AFRL-RQ-WP-TR-2021-0111

PRIMARY PROCESSING PARAMETERS AND THEIR INFLUENCE ON POROSITY AND FATIGUE LIFE OF ADDITIVELY MANUFACTURED ALLOY 718

Luke Sheridan
Air Force Research Laboratory
Aerospace Systems Directorate

MARCH 2020
Final Report

AIR FORCE RESEARCH LABORATORY
AEROSPACE SYSTEMS DIRECTORATE
WRIGHT-PATTERSON AIR FORCE BASE, OH 45433-7542
AIR FORCE MATERIEL COMMAND
UNITED STATES AIR FORCE

REPORT DOCUMENTATION PAGE

PLEASE DO NOT RETURN YOUR FORM TO THE ABOVE ORGANIZATION.

1. REPORT DATE	2. REPORT TYPE	3. DATES COVERED	
		START DATE	END DATE
30032020	Final	17102012	19102020

4. TITLE AND SUBTITLE

PRIMARY PROCESSING PARAMETERS AND THEIR INFLUENCE ON POROSITY AND FATIGUE LIFE OF ADDITIVELY MANUFACTURED ALLOY 718

5a. CONTRACT NUMBER	5b. GRANT NUMBER	5c. PROGRAM ELEMENT NUMBER
In-house	NA	62203F
5d. PROJECT NUMBER	**5e. TASK NUMBER**	**5f. WORK UNIT NUMBER**
3066	NA	Q11M

6. AUTHOR(S)

Sheridan, Luke

7. PERFORMING ORGANIZATION NAME(S) AND ADDRESS(ES)

Air Force Research Laboratory
Aerospace Systems Directorate
Wright-Patterson Air Force Base, OH 45433-7542
Air Force Materiel Command

8. PERFORMING ORGANIZATION REPORT NUMBER

AFRL-RQ-WP-TR-2021-0111

9. SPONSORING/MONITORING AGENCY NAME(S) AND ADDRESS(ES)	10. SPONSOR/MONITOR'S ACRONYM(S)	11. SPONSOR/MONITOR'S REPORT NUMBER(S)
Air Force Research Laboratory Aerospace Systems Directorate Wright-Patterson Air Force Base, OH 45433-7542 Air Force Materiel Command	AFRL/RQTI	AFRL-RQ-WP-TR-2021-0111

12. DISTRIBUTION/AVAILABILITY STATEMENT

DISTRIBUTION STATEMENT A. Approved for public release. Distribution is unlimited.

13. SUPPLEMENTARY NOTES

PA Clearance Number: (88ABW-2020-0622)

14. ABSTRACT

This effort explores the influence of four key process parameters and scan strategies on the formation and characteristics of porosity distributions in additive manufacturing (AM) material. Then, based on the porosity distributions observed via non-destructive inspection techniques, a crack-growth based life prediction method was developed to accurately predict fatigue lives of AM components. Additionally, fatigue limit models were modified based on experimental data to explore the interactions of defect size and applied stress with respect to both finite and "infinite" fatigue life which enables defect tolerant design for components manufactured via AM. Finally, a novel compliance-based method for crack initiation detection was developed and used to assess some of the assumptions made in prior investigations. The connections made through the work presented herein link AM processing to potential design requirement which will facilitate faster, safer design efforts for implementation of AM components into structurally critical applications.

15. SUBJECT TERMS

additive, manufacturing, life prediction, fracture mechanics, non-destructive inspection, damage tolerant design

16. SECURITY CLASSIFICATION OF:			17. LIMITATION OF ABSTRACT	18. NUMBER OF PAGES
a. REPORT	b. ABSTRACT	C. THIS PAGE		
Unclassified	Unclassified	Unclassified	SAR	141

19a. NAME OF RESPONSIBLE PERSON	19b. PHONE NUMBER *(Include area code)*
Jeffrey M Brown	(937) 255-7223

PREVIOUS EDITION IS OBSOLETE.

STANDARD FORM 298 (REV. 5/2020)
Prescribed by ANSI Std. Z39.18

PRIMARY PROCESSING PARAMETERS AND THEIR INFLUENCE ON POROSITY AND FATIGUE LIFE OF ADDITIVELY MANUFACTURED ALLOY 718

A dissertation submitted in partial fulfillment
of the requirements for the degree of
Doctor of Philosophy

by

LUKE C. SHERIDAN
B.S.M.E., Wright State University, 2015
M.S.M.E., Wright State University, 2016

2020
Wright State University

Wright State University
GRADUATE SCHOOL

March 30, 2020

I HEREBY RECOMMEND THAT THE DISSERTATION PREPARED UNDER MY SUPERVISION BY Luke C. Sheridan ENTITLED Primary Processing Parameters and Their Influence on Porosity and Fatigue Life of Additively Manufactured Alloy 718 BE ACCEPTED IN PARTIAL FULFILLMENT OF THE REQUIREMENTS FOR THE DEGREE OF Doctor of Philosophy.

Joy E. Gockel, Ph.D.
Dissertation Director

Philippe Sucosky, Ph.D.
Director, Engineering Ph.D. Program

Barry Milligan, Ph.D.
Interim Dean of the Graduate School

Committee on
Final Examination

Joy E. Gockel, Ph.D.

Nathan W. Klingbeil, Ph.D.

Ahsan Mian, Ph.D.

Onome Scott-Emuakpor, Ph.D.

Anthony Rollett, Ph.D.

ABSTRACT

Sheridan, Luke, C. . Ph.D., Engineering Ph.D. Program, Wright State University, 2020. *Primary Processing Parameters and Their Influence on Porosity and Fatigue Life of Additively Manufactured Alloy 718.*

In many structural applications void-like defects cause significant performance debits which call for component redesign or post-processing to account for or remove the defects. For laser powder bed fusion (LPBF) processes, it has been shown that many of these features and their size and shape characteristics are controllable through LPBF process parameter manipulation. For design efforts, however, it is necessary to understand the direct influences of processing on the formation of porosity and the role that individual pores and porosity distributions have on the properties and performance of AM components. Additionally, design criteria must be established to facilitate implementation of AM components into structurally critical applications. To this end, the investigations that have been performed here relate the AM material processing of alloy 718 to the pore structure, crack growth properties and fatigue performance. This dissertation first explores the influence of four key process parameters and scan strategies on the formation and characteristics of porosity distributions in AM material. Then, based on the porosity distributions observed via non-destructive inspection techniques, a crack-growth based life prediction method was developed to accurately predict fatigue lives of AM components. Additionally, fatigue limit models were modified based on experimental data to explore the interactions of defect size and applied stress with respect to both finite and "infinite" fatigue life which enables defect tolerant design for components manufactured via AM. Finally, a novel compliance-based method for crack initiation detection was developed and used to assess some of the assumptions made in the prior investigations. The connections made through the work presented herein link AM processing to potential design requirements which will facilitate faster, safer design efforts for implementation of AM components into structurally critical applications.

Contents

List of Figures

List of Tables

Acknowledgment

I would like to take this opportunity to extend my thanks to many of the people who have helped me in performing this accomplishment. First and foremost, I would like to thank the Lord for giving me the ability to think through complex problems and the curiosity to probe the details I have observed. I hope that in everything I will continue to use the talents he has given me to serve him in my career, my home, and in the world at large. Secondly, I would like to thank my wife who has been a great encouragement to me and who has supported me throughout our life together. Thank you for being patient and understanding while I went to class or stayed late at work and for being my adventure buddy as we travel the country and world together. I love you. Third, I would like to thank my children for the joy that they bring to my life. Although you have not been long living here on Earth, I want to thank you for always welcoming me home with hugs and kisses and for reminding me why I come home every day. I hope that my hard work will be an example to you of what can be achieved if you put your mind to it, and I pray that you will also remember how much I love you. You and your mom will always be my top earthly priority. Thank you, Mom and Dad, for the love you have shown me and the discipline you have instilled. You have taught me to love God first, others second, and myself last, and I pray that I will follow the example you have given me. I hope that I will be able to continue your legacy.

Thank you also to those who have helped me begin my professional career. Thank you to Terry Gillaugh, Dr. Danny Gillaugh, Dr. Greg Minkiewicz, Dr. Tommy George, and the entire crew at the Turbine Engine Fatigue Facility. You have all played an important part in getting me where I am today. Thank you for your willingness to answer my questions, comment on off-the-wall ideas, and proof-read my papers. Finally, thank you to my advisor Dr. Joy Gockel and my entire committee for their willingness to serve in this capacity. I appreciate the time that you have spent teaching me, mentoring me, and talking through my research with me. I look forward to continuing to work with each of you in the future.

As I reflect on the number of people who have helped me on my academic journey, I am very humbled that they have all given there time and effort to help me achieve this great accomplishment. I was recently considering how, two generations ago, my father's parents finished high school and went on to live full and successful lives which impacted their local communities. I only hope that I, having surpassed them from this educational standpoint, will be able to at least match the impact that they and others have had not only in my life but also in the world around them.

"And whatever you do, whether in word or deed, do it all in the name of the Lord Jesus, giving thanks to God the Father through him." Colossians 3:17, NIV

Dedicated to my family who has supported and encouraged me so much in this endeavor.

Introduction

Additive manufacturing (AM) has proven to be a versatile technology with promise for both current and future manufacturing endeavors. The versatility of AM processes allows for re-evaluation of current practices to produce cutting edge, weight-reducing designs while reducing manufacturing cost and material waste. Although the benefits of AM make it attractive to the defense and aerospace industries for maintenance, sustainment, and innovation both in deployed and domestic environments [3], there are many complex facets that need to be addressed before AM may be considered a viable manufacturing process for fracture-critical components. In order for the technology to reach its full potential and utility, extensive process development and thorough post-process analysis must be performed to develop sufficient qualification guidelines and techniques for AM components.

The processing-structure-property-performance (PSPP) relationship for materials is recognized as an important framework that guides material characterization and qualification. The push for rapid implementation of AM components draws interest from diverse research fields, and the branches that define the PSPP framework offer numerous opportunities for multi-disciplinary investigations. Due to the novelty of AM technology and its relatively recent emergence as a viable manufacturing technology, scientific knowledge is generally transferred from more mature technologies or better understood processes and applied to AM. One drawback from this approach is that research efforts may focus on one portion of the PSPP framework without accounting for the interactions between all four branches. For example, an investigation minimizing grain size may reduce beam power

and increase beam speed to reduce the cooling rate of the melted material. Consequently, the modified parameters reduce the melt pool size to the point where significant porosity develops which is detrimental to the fatigue life of the component. In another example, a designer may want a component to be built in a specific orientation to fit more components on the build platform, but anisotropy in the built material may require a different orientation due to the applied loading. For successful implementation of AM components in a wide number of applications, it is imperative that the designer understand the interactions of each PSPP branch with the others. If any of the four branches is insufficiently accounted for, the potential for a component's failure is significantly higher.

The purpose of this dissertation is to investigate the effects of processing on the development of porosity in AM nickel-base superalloy 718 and the fatigue performance of academic components. It will be demonstrated in the next few chapters that AM processing plays a significant role in pore population formation and that porosity characteristics determine the fatigue performance of the component. The large number of processing variables that define AM processes, however, makes quantifying the PSPP relationship very complex. It has been shown that certain primary process parameters (PPPs), such as Power, Speed, Hatch Spacing, and Layer Thickness, dominate internal defect development [4–7]. It has also been observed that certain pore population characteristics, such as average pore size, maximum pore size, and pore shape, can influence material performance [8, 9]. It is necessary, therefore, to quantify the influences of PPPs on porosity production for application to performance prediction.

The organization of this dissertation is designed to provide an in-depth description and analysis of each branch of the PSPP framework and to uncover insight into the interactions between the four branches. The literature review in the next chapter will step through each PSPP branch and discuss its significance and related work from the literature. Chapters 3-6 will detail methods, results, and discussion of four different investigations, and Chapters 7 and 8 will highlight conclusions and recommended future work. This dissertation

approaches porosity in AM components in light of the PSPP framework and traces the influence of AM processing to fatigue performance of porous AM materials. The insight gained from the work included herein will help inform process optimization efforts which will facilitate implementation of additive components in structural applications.

Background and Literature Review

2.1 The "PSPP" Relationship

The PSPP framework has been used extensively in the field of AM to explain trickle down influences of processing to the final part performance. Recognizing the importance of processing on every characteristic of a material is critical when designing for AM applications. For structural applications, defects have had wide recognition as the primary failure mechanisms for AM materials. While understanding the role that defects play on performance criteria such as creep and fatigue, it is equally important to recognize the role processing plays in defect formation which facilitates efforts to eradicate macroscopic defects entirely from AM materials. While its name gives some indication as to the scope of the PSPP framework, it is important to understand the meaning and the depth of each term.

2.2 Processing

Processing refers to the procedure of fabricating a component including production of raw material, synthesis of the raw material into the component shape, and post-manufacturing treatments of the material. Some common steps in AM processing include fabricating the stock material (powder, wire, etc.), building the component with specified process parameters (power, speed, hatch spacing, layer thickness, etc.), heat treating the material to achieve

the desired microstructure, and hot isostatic pressing (HIP) to heal defects in the components. For a given material, the processing that the material experiences has a profound influence on every characteristic of the material and the fabricated component from microstructural attributes (phase formation, grain orientation, grain size, and defect content) to elastic and plastic mechanical properties (modulus, ductility, toughness) to application-based performance (fatigue, creep, strength). Understanding the influence of material processing on the structure, properties, and performance of a component is imperative for application-specific design.

2.2.1 AM Processing

One strength of AM processing is that diverse AM processes are available to meet complex application requirements. Additionally, process tailoring to accomplish end user needs is easily accomplished due to the flexibility of the technology. The expiration of the initial AM patents has encouraged numerous companies to invest their resources in creating new machines, and the sheer number of processes that have been developed facilitates competition and creativity to set Company A apart from Company B. Any attempt to encapsulate the entirety of AM processing methods and approaches in this literature review would be very difficult and time consuming, so an overview of key mechanisms for AM and a summary of several well-known metal AM processes will be discussed here.

AM Process Characteristics

In general, AM processing requires a source material, a delivery system, and a heat source. There are several different types of source material which can be leveraged depending on the application. One common material form that is leveraged for high volume deposition rates is metal wire that is delivered to the component via a wire feed system. Component tolerances may be a cause for concern with this feed material because the material is de-

posited in such large quantities, but if the application allows for post-process machining, this feed material is appropriate for high deposition rate processes. Powder is another common feedstock used in AM applications. Powder is typically spherical and ranges between diameters of 10-200 μm. The powder size allows for complex features to be built, but generally leaves the component surface rough which can cause mechanical performance debits.

The delivery system required for a given machine depends on the feedstock form and the application of the component. For metal materials, there are two common delivery methods. The first is directed deposition of the material which involves using a nozzle to direct the material under the heat source and depositing the molten material onto a base component. This method is used for both wires and powders. For wires, a wire-feed system delivers the material underneath the heat source, and the molten material is deposited onto the component. For powder, the heat source melts a small region of the base material, and the metal powder is injected into the melted region commonly referred to as the melt pool. One creative advantage for directed powder processes is the capability to build multi-material components. Several different nozzles can be leveraged to deliver different materials to the build which allows for graded/multi-alloy applications. Often, directed deposition delivery systems leverage CNC type systems to direct the feedstock material which makes this delivery system amenable to component repairs, an application that is very difficult with other delivery systems.

The second delivery system, powder bed fusion, is exclusively for powders. This delivery process is commonly used for aerospace components due to the tight tolerances facilitated by fine powder feedstock. Currently, powder bed systems are limited to relatively small components due to machine size limitations. The system consists of a build platform and a powder hopper that supplies the powder to the build platform. A recoater blade spreads a thin layer of powder across the build platform. In beam-based AM, a heat source (laser or electron beam) scans the powder and melts the component cross-section. Once the

cross-section has been melted, the build platform recedes a specified layer thickness depth, the powder hopper platform rises, and the recoater blade spreads another layer of powder across the build platform.

Just like feedstock and delivery systems, the heat source that is applied can depend on the application for which the component will be used. Beam based-AM processes leverage either electron beams or laser beams to melt the stock material. Laser beams typically range from 50 W to 1kW and are used for fine features. Typically, mirrors are used to direct the beam from one or multiple sources to the component. Electron beams generally exhibit much higher powers (up to 100 kW) and leverage electromagnetic lenses to guide and move the beam. For electron beam powder bed fusion processes, an initial pre-sintering step is required using a defocused electron beam. This is because the momentum of the electrons is sufficient to displace the powder particles in the bed which removes the feedstock from the melt region and prevents building up the part. This pre-sintering step also acts to maintain an elevated preheat temperature throughout the entire component which reduces the residual stress in the part and results in significantly larger grain structure. On the other hand, pre-sintering the powder also causes the entire build volume to be semi-solid, and removing the semi-sintered powder from the fully fused component leaves the component surface very rough.

AM Process Physics

Despite differences in feedstock, delivery system, and heat source, beam-based AM processes exhibit similar physics once the beam is applied to the material. The beam delivers energy to the base material and the feedstock at a given rate which is designated the power (Q) of the beam, and at the same time, the beam travels across the build region at a given speed (S).

For a beam of given power traveling along a straight path at a constant speed, the thermal field in the base material can be approximated using Rosenthal's heat transfer solution

[10]. The solid bounded by the solidus temperature isosurface from this solution gives the approximate shape of the "melt pool". The melt pool shape and size is directly related to the power and speed of the beam as is discussed in [11–15]. These authors showed for a variety of processes and materials that as the power increases, the width and depth of the melt pool increases. They also showed that as velocity increases, the width and depth of melt pool decreases. Therefore, optimization of these two parameters is necessary to retain constant melt pool dimensions. Bertoli *et al.* further showed that beam power actually has a stronger influence on melt pool depth during melting than scan speed [16]. As the melt pool traverses the base material, it leaves a deposited path in the material which is approximately ellipsoidal. Cases in which the ellipsoid assumption breaks down are when the power is sufficiently high or the beam speed is sufficiently low to cause keyhole mode melting. In these cases, the large amounts of energy per unit volume of material evaporates certain materials within the melt pool, and pressure gradients within the melt pool cause the depth to increase. This keyhole mode melting gets its name from the characteristic "keyhole" shape of the melt pool and is generally identified by a depth to width ratio significantly greater than one half.

While the single line laser path is one of the most basic beam maneuvers observed in beam-based AM processing, machines typically combine multiple back and forth passes into a scan to fuse a solid part. After each single line, the beam translates a certain hatch spacing (H) and begins another single line pass. The combination of these hatch patterns make up the scan strategy and the strategy can be modified to achieve certain material property and performance goals.

Three such scan strategies are the continuous meander (CM), striped meander (SM), and island meander (IM) scan strategies which are exhibited in Figure 2.1[17]. Modifying the scan strategy changes the thermal processing history which is crucial for phase formation, grain growth, and orientation control in materials. It has been shown that certain scan strategies encourage defect formation at laser path intersections [18] which can have

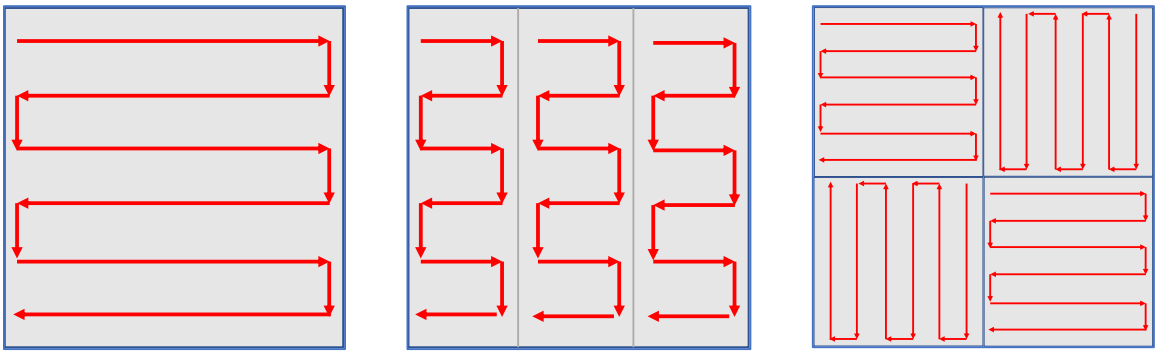

Figure 2.1: Three scan strategies commonly used in AM processes: Continuous Meander (CM), Striped Meander (SM), and Island Meander (IM)

a detrimental effect on the performance of a component.

Since the laser power and speed change the size of the melt pool and hatch spacing describes how far apart the centers of the melt pools are separated, it is intuitive that increases in hatch spacing will eventually result in complete separation of adjacent melt pools such that there is no overlap. In such lack of fusion (LOF) cases, a significant amount of porosity is expected. Analogously, if the layer thickness (L) is sufficiently large that the current layer's melt pools do not reach the base material, LOF should also be expected. Similar relationships between processing and material structure have been noted in the literature as will be discussed below. Therefore, optimization of the process parameters is imperative to assure proper processing of the material.

2.2.2 Post-Processing

There are several post-processing procedures that are performed for additive materials to increase performance and properties for AM components. Heat treatment methods are used to remove residual stress and acquire desirable microstructure. Multiple standards are available that describe appropriate heat treatments for AM alloy 718, but it is important to maintain consistent procedures to appropriately compare test to test variation. In light

of this, heat treatments prescribed in ASTM 3055 [19] will be used in this work. This standard calls for a stress relief of the component at 1950 °F (1065 °C) for approximately 90 minutes. This stress relief takes place while the components are still on the plate. Once the components are removed from the plate, a solution annealing step is performed on the components at 1750° F (954° C) for approximately 30 minutes. An aging treatment is performed at 1325° F (718° C) for 8 hours, and then the temperature is reduced to 1150° F (621° C) for another 8 hours. The material is then furnace cooled to room temperature.

Porosity, as mentioned previously, is a common defect in additive materials. One method for removing porosity from an AM component is HIP which involves heating the material and applying significant amounts of hydrostatic pressure to the component. The combination of heat and pressure will "heal" many of the internal pores. Because the focus of this investigation is the effect of porosity on fatigue in AM components, HIP was not performed on any of the components described herein.

Finally, AM processes generally produce rough surfaces. A combination of periodic formations caused by intersections of melt layers and non-regular formations of powder adhered to the surface of the build introduce numerous possible crack initiation locations on the surface of AM components. Machining is commonly performed for AM components that undergo cyclic loads to minimize the probability of failure due to a surface notch. Machining will be performed on the experiments described herein to isolate the effects of porosity on fatigue life and minimize the probability of a surface notch-induced failure.

2.3 Material Structure

The structure represents the baseline attribute of a material from which it derives its properties and performance. Significant amounts of work have shown that AM microstructures are strongly dependent on AM process parameters. Microstructure manufactured via beam-based AM methods generally exhibits elongated morphology and grows in the direction of

the thermal gradient (generally in the build direction) [13]. Larger grains are traditionally found in components manufactured with low cooling rates produced by combinations of low speeds and high powers [15, 20]. Additionally, thermal gradients induced during the build process facilitate grain growth in preferred orientations [21, 22]. Material structure includes not only grain characteristics but also defects and voids that are contained within the component. Pre-existing raw material defects and AM process-induced defects are common in AM materials, and they typically appear in three main forms: surface roughness, surface porosity, and internal porosity. Each of these defect types cause sub-standard mechanical performance in the component, but it has also been shown that they can be modified and/or removed via post- and in-situ processing of the components [8, 23].

Previous work at Wright State and Carnegie Mellon Universities has traced process parameter factors to several structure and property effects in additive materials across a wide range of process space. The process parameters of interest include beam power, beam speed, material feed rate, substrate preheat, and component geometry while outcomes include melt pool geometry measurements (length, width, depth, cross-sectional area) [13, 15], microstructure morphology (feature width, feature aspect ratio) [13, 15, 24], and component performance (fracture toughness, ultimate strength, fatigue life) [15, 25]. These works focused on several regions of process space (shown in Figure 2.2).

2.3.1 Defects

As was discussed in 2.2.1, AM processing plays a key role in multiple types of component defects. LOF defects occur when insufficient melting characterizes the material, and keyhole mode melting occurs when over-melting is prevalent. Gas-porosity, another defect type occurs when air bubbles exist in the supply material[5]. When the stock material melts, the gas bubble is unable to escape into the atmosphere before the material re-solidifies, and the defect is left in the final part. Significant amounts of work have been performed to

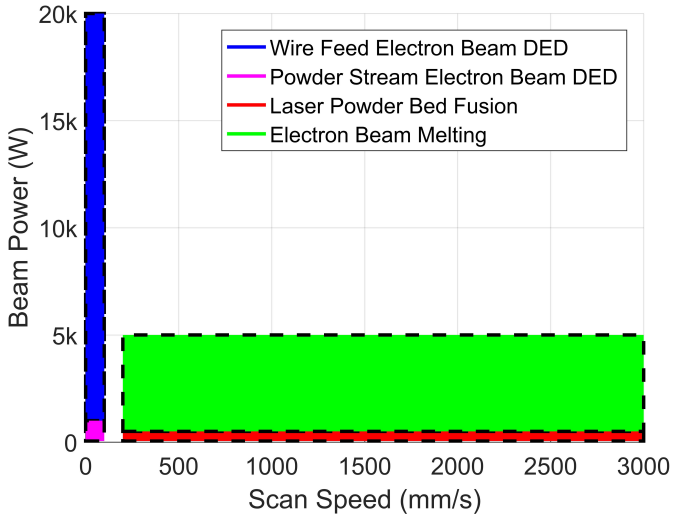

Figure 2.2: Power-speed process map of common AM process regions (adapted from [14])

model the process-material interactions to help predict the defect structure in the material. It is important to recognize the process characteristics that drive defect formation and to quantify the defect attributes that will drive component performance.

Defect Formation and Process Modeling

Several models have been developed in the literature to describe and predict LOF and key-hole defects due to AM processing. The relationship between PPPs and component density is driven by multiple factors including melt pool shape [26, 27] and thermal properties of the material [16, 28], and the models have been developed to help predict defects in AM materials. Tang *et al.* leveraged the Rosenthal point source model to overlap multiple melt pool geometries [10, 27]. They leveraged the elliptical shape of the melt track and hypothesized that LOF porosity, defects produced through insufficient overlap of melt pools in either the lateral or vertical direction, would occur when

$$\left(\frac{H}{W}\right)^2 + \left(\frac{L}{d}\right)^2 \leq 1 \tag{2.1}$$

where H is the Hatch Spacing, W is the melt pool width, L is the layer thickness, and d is the melt pool depth. This model effectively predicted the density of AM components due to LOF defects. Tang's model did not take phase change properties into account, so its applicability to keyhole type porosity prediction was limited. King *et al.*, however, showed that normalized enthalpy, could accurately predict conditions for keyhole mode melting. They derived a criterion for a material melted under a moving Gaussian heat source such that

$$\frac{\Delta H}{h_s} = \frac{\alpha Q}{h_s \sqrt{\pi D_m S \sigma^3}} \geq \frac{\pi T_b}{T_m} \tag{2.2}$$

where α is the power absorptivity factor, Q is the beam power S is the beam speed, σ is the beam spot diameter, D_m is the material diffusivity at the melting temperature (T_m), h_s is the material enthalpy at melting, and T_b is the boiling temperature of the material. King showed that melting conditions satisfying this criteria exhibited keyhole behavior and that a clear transition point is made at the threshold from conduction dominated melting (with elliptical melt pools) to keyhole dominated melting.

Another popular model to predict or explain component density is that of energy density. Multiple variations of energy density have been defined that describe different energy delivery aspects of the AM process, but Thijs *et al.* [29] defined volumetric energy density (VED) as

$$E_v = \frac{Q}{S * H * L} \tag{2.3}$$

Gong *et al.* attempted to show that this quantity could indicate process regions that minimize defects [6, 30]. Spierings *et al.* also showed that VED could be functionally related to component density [31]. Bertoli *et al.* confirmed that decreasing energy density degraded single melt pool tracks and that increasing energy density beyond a certain threshold would similarly induce irregular single melt pool tracks. According to Bertoli, however, VED has limitations in predicting keyhole mode melting because it does not take into account the physical behavior of the material [16]. Furthermore, Tang showed that controlling VED

need not necessarily improve part density: Maintaining a constant VED (while changing PPPs) may result in varying porosity [27]. This was further illustrated by Sheridan *et al.* [32] and will be presented in detail in Chapter 3.

Due to this ambiguity, it is important to recognize the role that each PPP plays in the formation of the melt pool and, therefore, in the creation of defects as was discussed in 2.2.1. Kasperovich *et al.* explored multiple process parameters including beam power, speed, hatch spacing, and focal distance, and they showed that beam power and speed have the most significant effect on component porosity [7]. Darvish *et al.* also showed that increasing beam power improved melt pool stability and track overlap consistency [33] which reduces stochastic (random) porosity.

During keyhole mode melting, material vaporization creates a pressure gradient that elongates the melt pool depth. Rapid cooling encapsulates vapor bubbles which increase component porosity. Keyhole mode melting typically occurs at elevated VED, but as mentioned above, VED is unreliable for predicting a keyhole threshold. It has been shown, however, that increasing beam spot size to the scale of the melt pool width can help avoid keyholing phenomena [34].

Several authors have explored process spaces and have shown the dependence of defect density on PPPs and VED [5, 26, 35]. Generally these papers focus on small regions of process space with multiple PPPs held constant. PPP interactions are rarely discussed. Furthermore, a majority of the authors conducting this research pay particular attention to average component density and ignore defect size distributions and defect shape. These characteristics have been shown to play a significant role in component performance [8, 9, 36, 37]. The work described herein explores a wide region of process space, assesses interactions of PPPs, provides insight into pore formation, and characterizes experimental trends in component density, pore size and pore shape.

Defect Characteristics in Additive Components

Defects in AM material come in many forms, sizes, and shapes. They are commonly created as a result of improper material processing or because of slight variations or inconsistencies of process parameters at a specific moment or location in the build. It has been shown that defects in materials are common failure mechanisms and can dominate other features that may eventually cause failure in the component. In structural applications, it is necessary to have a general knowledge of the defect content to properly design a component. Many authors have elected to use average defect quantification metrics such as overall component density or cross-sectional pore area fraction to quantify defect content [38–40]; however, for predicting structural performance it is necessary to look at other, more specific quantities and to characterize each pore as a member of a population. It is only through knowing the actual defect signature and being able to model it that relevant and accurate models of AM component performance can be developed. Three metrics that are commonly used to characterize individual pores (size, location, and shape) are discussed below.

It is well known that performance criteria such as fatigue are driven by the weakest link. A component is limited in its performance by the defects that are contained within it and by how those defects interact with the applied stress state. If several similarly shaped pores were formed within a component, it would be intuitive that the largest pore would be the weakest link. Local stresses would increase in the vicinity of the pore due to stress concentration phenomena and material damage would occur and propagate from this location. Therefore, quantifying the sizes of pores within a component is important for determining locations of high probability component failure. One method for characterizing pore size is to use the projected cross-sectional area of a pore as proposed by Murakami [41]. Three-dimensional characterization of pores is expensive and infeasible in many applications, but two dimensional characterization is easily performed. Additionally, stress is transmitted through a finite cross-section of a component; therefore, it is intuitive that a pore with a

larger cross-section would concentrate stress more than a pore with a much smaller cross-section.

Another pore characteristic of note is the location of a pore in relation to other pores and the component surface. Stress in the vicinity of multiple stress concentrating features will be amplified significantly. Therefore, it is important to recognize when defects collect in similar locations. It has been shown that collections of small pores within a certain radius of each other tend to act as a single, large pore. Because of this, lines of pores produced through keyhole mode or even LOF melting may act significantly different from similar pores that are more randomly distributed. Similarly, a crack emanating from a surface pore is approximated to have a thirty percent increase in stress intensity compared to an internal pore [41–44]. This means that a surface crack will grow significantly faster than a similar internal crack which reduces the fatigue life of that component. A majority of the components built during this investigation were significantly dense so that the pores were "evenly" distributed. Because of this, pore location with respect to other pores was not examined in-depth.

Finally, pore shape may also be an important characteristic for fatigue life and performance. Just as pore size and location can change stress concentration and crack growth rate properties, pore orientation and shape can have a dramatic impact on the local stress state in the material. Often, crack orientation has a strong dependence on build direction. This is specifically true for LOF porosity where long, unfused tracks tend to align parallel with layers of individual scan tracks. Keyhole mode porosity is typically spherical, and does not exhibit irregular shapes inherently, but a collection of closely-spaced pores produced by keyhole mode melting may exhibit behavior similar to a thin, elongated crack. When a long, flat crack is oriented perpendicular to the applied load, the stress intensity at the crack tip will be much greater than the stress intensity of the same crack oriented parallel to the loading direction.

Additionally, pore shape can play a key role in crack formation. Pores with high aspect

ratios will typically initiate cracks much faster than low aspect ratio, spherical pores of the same size. This is because the radius of curvature of the pore is much smaller which induces a larger stress concentration. As a result, it is important to recognize orientation and shape effects when designing a component for a specific application. Build orientation and loading orientation must be considered in order to successfully implement the component, and inspection of internal features is necessary to verify that pore shape and orientation meet specified criteria to prevent premature failure. Failure to take pore shape and orientation into account could result in significant life debits and insufficient component performance.

2.3.2 Material and Grain Structure

Alloy 718 [45] is a precipitation strengthened nickel-based superalloy commonly used in aerospace structural applications because of its strength at high temperatures. Alloy 718 is generally a good candidate for turbine engine hot section components. The superalloy contains high percentages of chromium and iron as seen in Table 2.1.

Table 2.1: Alloy 718 Composition

	Al	B	Cr	Cu	Fe	Mn	Mo	Ni+Co	Nb+Ta	P	Ti	C	S
Nominal	0.5	<0.006	19.00	<0.3	18.00	<0.35	3.05	Bal.	5.15	<0.015	0.9	<0.08	0.015

Alloy 718, a face centered cubic structured material, exhibits many different phases which all contribute to its properties and performance, but it's main strengthening mechanisms are the γ' (NiAL) and γ'' (Ni_3Nb) phases. Both of these phases are coherent with the γ matrix. AM alloy 718 microstructure has been characterized extensively in the literature [21, 22, 46–52], and attempts have also been made to control microstructure in AM components through the use of novel scan strategies and controlling process parameters [53].

Alloy 718 is a precipitation strengthened alloy which relies on specific heat treatment regimens to nucleate and grow strengthening phases. Traditionally, a heat treatment regi-

men for precipitation alloys consists of a solution treatment to bring all secondary phases into solution and a precipitation phase to control the size and percentage of each phase in the final structure. For additive materials, a preliminary heat treatment is performed before the material is removed from the baseplate to relieve residual stresses that are produced due to the contraction of cooling layers and the expansion of deposited layers throughout the growth of the component. Currently, several efforts are working to optimize heat treatment procedures for additive materials [54, 55]. Several documents have also been put forward to standardize heat treatment procedures for AM alloy 718 [19, 56]. For the experiments described in this work, a consistent heat treatment procedure was performed to reduce any variation due to processing. These procedures are specified in section 2.2.2.

2.4 Properties and Performance of Additive Components

The properties of a material describe a material's behavior. Structural properties that are of primary interest include elasticity, toughness, strength, ductility, and crack growth behaviors. These properties are specific to the material and are heavily influenced by the structure of the material. For AM materials, they are often non-isotropic and must be thoroughly quantified to properly inform any design efforts. Many AM materials have proven comparable with wrought materials in terms of elastic properties and material strength, and they have occasionally exceeded properties of traditionally manufactured materials [2, 57, 58]. Properties such as strength, toughness, ductility and crack growth may vary significantly depending on the orientation of the applied load with respect to the build direction. These phenomena occur due to the directionality of grain growth and defect orientation. Parallel, elongated grains will certainly behave differently in one direction compared to another direction, so understanding the material structure is imperative for interpretation of material property component to component variation.

The performance of a component is determined by the properties of a material. More

specifically, the performance quantifies how well a component is able to accomplish its role in a specific application. While properties focus mainly on a material's capabilities, the performance emphasizes the component's ability to do its job satisfactorily. The design-intended performance of a component is always the end goal, but it is impossible to adequately predict the performance of the component without an extensive understanding of the processing, structure, and properties that characterize the component. Therefore, a multi-disciplinary approach must be taken to trace the effects of AM process parameters throughout the entire PSPP chain for adequate, accurate, and successful implementation of AM components in aerospace applications.

2.4.1 Tensile Properties of Alloy 718

It has already been stated that material structure will certainly influence the properties of a material. Therefore, it is expected that different heat treatment procedures will produce significantly different tensile properties. Expected tensile properties for various post-process profiles are described in Table 2.2 [57].

Table 2.2: Alloy 718 tensile properties for various heat treatment states

	As-Built	Stress Relieved	HIP'ed	Solution Annealed	Precipitation Aged
Ultimate Strength	127 ksi	133 ksi	185 ksi	119 ksi	198 ksi
0.02% Yield Strength	112 ksi	75 ksi	135 ksi	46 ksi	153 ksi
Young's Modulus	26e3 ksi	28e3 ksi	29e3 ksi	26e3 ksi	28e3 ksi
Elongation	30%	42%	24%	29%	20%

Likewise, material orientation has been shown to significantly impact tensile properties of AM 718. Under a consistent solutionized and aged heat treatment, tensile properties can tend to vary as shown in Table 2.3 [58]

As is observed from both Tables 2.2 and 2.3, additive material elastic properties compare favorably with wrought material. It can also be observed from the literature that the sensitivity to AM processing parameters is not noticeable in certain circumstances.

Table 2.3: Alloy 718 tensile properties for three build orientations[1, 2]

	Extruded Rod	90° (Horizontal)	45°	0° (Vertical)
Ultimate Strength	180 ksi	194 ksi	196 ksi	186 ksi
0.02% Yield Strength	150 ksi	146 ksi	152 ksi	137 ksi
Young's Modulus	29e3 ksi	29e3 ksi	29e3 ksi	29e3 ksi
Elongation	12%	16%	17%	15%

2.4.2 General Fatigue Performance

It is well known that a material discontinuity such as a notch or hole will elevate the stress in the local region surrounding the discontinuity. The stress concentration (K_t) for an elliptical notch is of the form

$$K_t = \sigma_\infty \left(1 + 2\frac{a}{b}\right) \tag{2.4}$$

where σ_∞ is the applied stress, a is the notch length, and b is the notch width [59]. Under the assumptions of LEFM, as $b \to 0$ as in a crack, the elastic stress field around the crack asymptotically approaches infinity at the crack tip. Irwin [60] approximated the stress field (σ_{yy}) surrounding a crack tip in a large plate as

$$\sigma_{yy} = \sigma_\infty \frac{\sqrt{\pi a}}{\sqrt{2\pi r}} \cos\frac{\theta}{2}\left(1 + \sin\frac{\theta}{2}\sin\frac{3\theta}{2}\right) \tag{2.5}$$

and for $\theta = 0$,

$$\sigma_{yy} = \frac{\sigma_\infty \sqrt{\pi a}}{\sqrt{2\pi r}} \tag{2.6}$$

The numerator of Eq. 2.6, coined the stress intensity factor (SIF), K, defines the rate at which the asymptotic stress approaches infinity at the crack tip. This factor is commonly used to describe the stress state around a crack and has major implications on the fatigue and fracture behavior of a material. Not all cracks occur in large plates, however, so there is a correction necessary to accurately represent the stress fields of cracks under various

conditions. Therefore, common SIF representations are of the form

$$K_I = Y\sigma_\infty\sqrt{\pi a} \tag{2.7}$$

where Y is a shape correction term, and the I subscript represents an in-plane mode of stress. For fatigue applications, the stress is cyclic; therefore the cyclic SIF is defined as [59]

$$\Delta K_I = Y\Delta\sigma_\infty\sqrt{\pi a} \tag{2.8}$$

Murakami suggested that many surface features and material defects such as surface roughness and pores are sufficiently small to be modeled as small cracks [41] such that a defect could be approximated as an ellipse which circumscribes the defect's projected area. The equivalent crack length for SIF calculations was assumed to be the square root of the cross-sectional area ($\sqrt{A}$) of the ellipse. He showed that the SIF of an interior pore could be represented by

$$\Delta K_{I,i} = 0.5\Delta\sigma\sqrt{\pi\sqrt{A_i}} \tag{2.9}$$

and a surface pore by

$$\Delta K_{I,j} = 0.65\Delta\sigma\sqrt{\pi\sqrt{A_j}} \tag{2.10}$$

where A_i and A_j are the projected area of any bulk and surface pore respectively. According to Murakami a pore is a surface pore if $\sqrt{A}/e_0 > 0.8$ where e_0 is the distance of the pore's centroid to the free edge of the component. [41].

Fatigue life is distinguished by three distinct phases: Crack initiation, crack growth, and catastrophic failure. For high cycle fatigue (HCF), crack initiation dominates the fatigue life, and crack growth is relatively short. For low cycle fatigue (LCF), the converse is true. In both case, material structure determines the behavior of the material under a cyclic load. During each load-unload sequence, damage is introduced in the material through

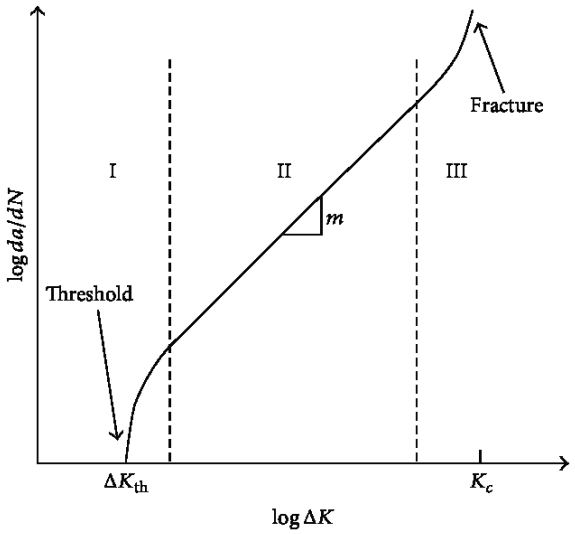

Figure 2.3: Crack growth curve diagram showing the three phases of crack growth: threshold, stable, unstable (fracture) [61].

the movement of dislocations. Dislocation movement in alloy 718 is often inhibited by structural features like intergranualar particles (carbides), intragranular particles (γ',γ''), or grain boundaries, and the dislocations begin to pile up at these locations. Once these dislocation "clusters" reach a saturated level, they frequently initiate microstructurally small cracks which propagate through a grain (if internally initiated) or around a grain (if initiated at a grain boundary) until it reaches another grain boundary. The crack must then change directions based on the next grain's crystal orientation. The crack continues to grow in this manner until it has reached a critical size, at which point it becomes a normal stress-induced (Mode I) growth that propagates quickly through grains and can be seen as continuum level crack growth. Long crack growth is characterized by three distinct phases: near threshold crack growth, stable crack growth, and unstable crack growth. These phases are illustrated in Figure 2.3.

The plot shows how the crack growth rate ($\frac{da}{dN}$) changes as the SIF increases. Phase I, the near-threshold crack growth regime, represents the period in which the crack is growing very slowly due to low loading conditions or extremely small crack length. Phase II repre-

sents stable crack growth and typically follows a power law trend. Phase II is the longest observable crack growth stage. Phase III represents unstable crack growth leading to fracture. This phase is typically the shortest of the three phases, and can usually be neglected for HCF applications.

There are several different methods for modeling the phases of crack growth. The simplest method ignores the very small growth rates in Phase I and the unstable crack growth in Phase III and accounts for only phase II crack growth. This particular crack growth model is represented by a power equation known as the Paris law (Eq. 2.11) where ΔK_I is the cyclic SIF in mode I and C and n are material specific crack growth constants [62].

$$\frac{da}{dN} = C(\Delta K_I)^n \tag{2.11}$$

Another commonly used model for crack growth measurement is the NASGRO equation [63] (shown in Eq. 2.12) which accounts for threshold growth (ΔK_{th}), crack closure (f) due to residual stress and fracture surface roughness, stress ratio (R), and unstable growth at the critical SIF (K_c).

$$\frac{da}{dN} = C\left[\left(\frac{1-f}{1-R}\right)\Delta K\right]^n \frac{[1-\frac{\Delta K_{th}}{\Delta K}]^p}{[1-\frac{K_{max}}{K_c}]^q} \tag{2.12}$$

In this equation, C, n, p, and q are material constants that are obtained from experimental data and K_{max} is the maximum SIF in the load cycle.

While the NASGRO equation provides significantly more fidelity in representing small crack growth and final fracture, the Paris law's simplicity is attractive for quick and efficient implementation for fatigue life prediction. Additionally, depending on initial pore size and stress levels, the failure pore's initial SIF commonly lies above the threshold within the Paris region. For the academic fatigue specimens used in the following investigations, the crack length will never reach the critical length which causes failure. Instead the failure

will occur when the normal stress in the remaining ligament exceeds the ultimate stress of the material.

Crack growth rate models are commonly used for growth life prediction. The Paris law is a popular model for this life prediction because a closed-form equation for crack growth life may be derived from it. Since ΔK_I is a function of crack length (a), like terms in Eq. 2.11 may be isolated, and each side of the equation may be integrated. This gives a general equation for fatigue life prediction based on initial crack length (a_1) and final crack length (a_2).

$$N_f = \frac{1}{C(\Delta\sigma Y\sqrt{\pi})^n} * \frac{a_2^{-n/2+1} - a_1^{-n/2+1}}{-n/2+1} \tag{2.13}$$

where C and n are crack growth constants and Y is the stress intensity shape factor. Konecna et al. [64] showed that the crack growth rate of LPBF alloy 718 having undergone HIP procedures may be represented using the parameters $(C, n) = (4.54 * 10^{-11}, 2.3)$, so

$$N_{f,bulk} = \frac{a_1^{-0.15} - a_c^{-0.15}}{(0.15)(4.54 * 10^{-11})(0.5\Delta\sigma\sqrt{\pi})^{2.3}} \tag{2.14}$$

and

$$N_{f,surf} = \frac{a_1^{-0.15} - a_c^{-0.15}}{(0.15)(4.54 * 10^{-11})(0.65\Delta\sigma\sqrt{\pi})^{2.3}} \tag{2.15}$$

where a_c is the critical crack size at which the component will fail. In this dissertation, the critical crack size is defined as the crack length required to exceed the normal strength of the material under a given load. For application of the crack-growth based life prediction method presented above to larger components, the critical crack size may be defined as the minimum crack size that will surpass either the bearing strength or the critical fracture toughness of the material.

2.4.3 Fatigue Performance of Alloy 718

Similarly to the tensile properties observed in section 2.4.1, fatigue properties and performance will vary with heat treatment procedure and build orientation. For structural aerospace applications, however, alloy 718 is rarely used in an annealed state because the aging procedure is what gives the material its strength. A brief literature review of fatigue performance for both additive and wrought alloy 718 was performed and is summarized in Figure 2.4 [2, 65–67].

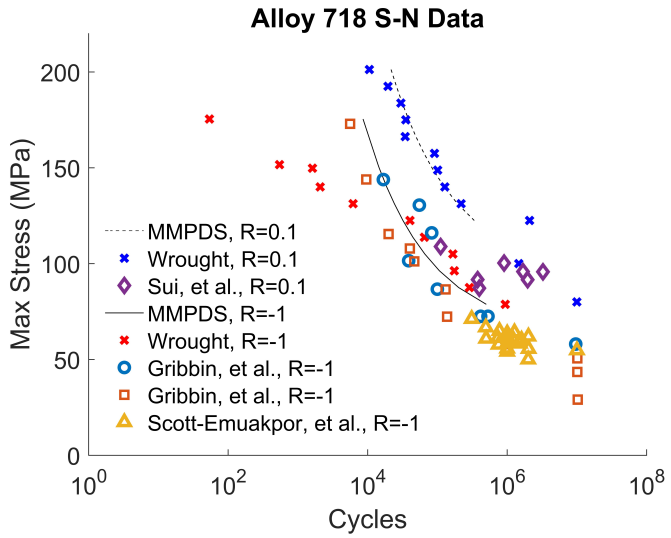

Figure 2.4: S-N curves obtained for both wrought and AM alloy 718 from in-house experiments (x) and the literature.

It can be seen that wrought material generally out-performs AM material. This is commonly attributed to elevated levels of porosity and defects in additive material that are not present in wrought material. There is a relatively large amount of scatter in the additive material which, again, is related to the random failure pores.

2.4.4 Fatigue Limits and Flawed Materials

When internal defects are considered to determine the probability of causing component failure based on the assumptions given previously, only a subset of the observed flaws

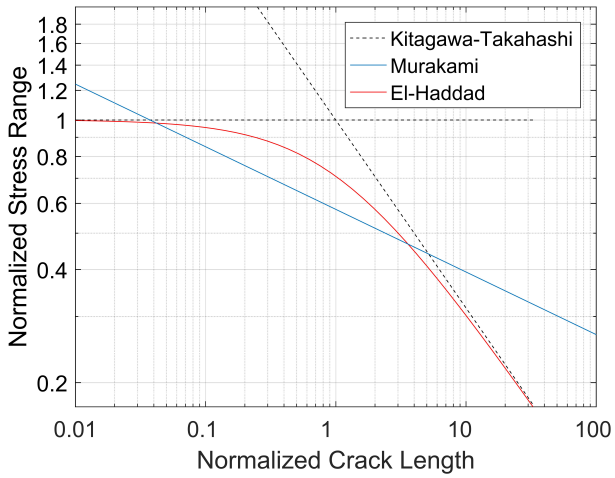

Figure 2.5: Normalized plots for endurance stress models as proposed by Kitagawa and Takahashi, Murakami, and El-Haddad. The y-axis has been normalized by the endurance stress of the material without a defect, and the x-axis has been normalized by the critical crack length (l_0)

.

need be considered in determining the fatigue life of the component. It is well understood that large flaws will more likely initiate failure inducing cracks, and they will propagate much quicker than smaller flaws. Similarly, small pores will experience significantly longer initiation lives, and the cracks will propagate at much slower rates compared to larger defects. For this reason, there exists some critical flaw size for a given stress level which will not cause failure in the component. A defect is considered to be below the critical size when its stress intensity defined by Eqs. 2.15 or 2.14 is below the threshold stress intensity value as determined by the material's crack growth behavior. One criteria for defining this threshold is that the stress intensity value produces a crack growth rate ($\frac{da}{dN}$) of less than 10^{-10} meters per cycle. Any flaw larger than the critical flaw size has the potential to cause a failure, but any flaw smaller than the critical flaw size will not initiate a failure inducing crack.

There have been several models introduced in the literature for estimating critical defects and fatigue limits for AM components. Three of these models are visualized for alloy 718 in Figure 2.5 and discussed below. The first model was developed by Kitagawa and

Takahashi [68]. They recognized that crack propagation was dominated by two physical mechanisms depending on the crack lengths and the applied stress. They found that cracks of a certain size did not propagate to failure at the endurance limit of the material. The horizontal dotted line pictured in Figure 2.5 represents this condition. They showed, however, that there was some critical crack length that would propagate even at the endurance limit causing failure. For cracks longer than this critical length, non-propagation required that the stress intensity of the crack be less than the threshold stress-intensity of the material. This condition is described by the dotted diagonal line in Figure 2.5. The equation of this line is obtained by solving Eq. 2.10 for $\Delta\sigma$ and specifying ΔK as the threshold SIF range for the material.

El-Haddad *et al.* [69] derived a mathematical model to predict the endurance limit phenomenon described by Kitagawa and Takahashi. El-Haddad's model included the same physics, but they included a region of crack length during which the non-propagation mechanism transitioned from endurance limit to linear elastic fracture mechanics assumptions. They proposed that the stress intensity of a specific crack of length $l + l_0$ had a stress intensity of approximately

$$\Delta K = Y\Delta\sigma\sqrt{\pi(l + l_0)}. \tag{2.16}$$

where l_0 is the critical crack length below which a crack will not propagate under the endurance stress, l is some length beyond the critical crack length, and ΔK and $\Delta\sigma$ are the cyclic SIF and the cyclic stress respectively. The threshold SIF may then be stated as

$$\Delta K_{th} = Y\Delta\sigma_e\sqrt{\pi(l_0)} \tag{2.17}$$

where $\Delta\sigma_e$ is the endurance stress range of the base material. Therefore,

$$l_0 = \left(\frac{\Delta K_{th}}{Y\Delta\sigma_e}\right)^2 \frac{1}{\pi}. \tag{2.18}$$

From 2.16, for a crack of length $l + l_0$, the threshold stress below which the crack will not propagate ($\Delta\sigma_w$) can be represented by the following equation:

$$\Delta\sigma_w = \frac{\Delta K_{th}}{Y\sqrt{\pi(l + l_0)}} \tag{2.19}$$

which when combined with Eq. 2.17 becomes the more common form:

$$\Delta\sigma_w = \Delta\sigma_e\sqrt{\frac{l_0}{l + l_0}} \tag{2.20}$$

Murakami *et al.* [42–44] developed a model that exhibited simplified behavior. They demonstrated that the fatigue limit (σ_w, MPa) of a material with a defect could be predicted using the Vickers hardness (H_v) of the material and the equivalent diameter ($\sqrt{A}$, μm) of the defect using the below relationships:

$$\sigma_{w,bulk} = 1.56\frac{H_v + 120}{\sqrt{A_i}^{1/6}}\left[\frac{1 - R}{2}\right]^{\alpha} \tag{2.21}$$

$$\sigma_{w,surf} = 1.43\frac{H_v + 120}{\sqrt{A_j}^{1/6}}\left[\frac{1 - R}{2}\right]^{\alpha} \tag{2.22}$$

where

$$\alpha = 0.226 + H_v \cdot 10^{-4}. \tag{2.23}$$

Several other models similar to the three mentioned above have been developed for defect tolerant design (highlighted in [43]) , but they are not discussed here.

Beretta, Romano, and others have applied the early work performed by Kitagawa and Takahashi, El-Haddad, and Murakami to AM material performance characterization. Beretta *et al.*[70–72] modified the El-Haddad model (Eq. 2.20) by replacing the El-Haddad parameter (l_0) with a modified parameter ($\sqrt{A_0}$) and crack length (l) with the Murakami

equivalent defect diameter ($\sqrt{A}$) such that for porous materials,

$$\Delta\sigma_w = \Delta\sigma_e \sqrt{\frac{\sqrt{A_0}}{\sqrt{A} + \sqrt{A_0}}} \tag{2.24}$$

where $\sqrt{A_0}$ is of the same form as Eq. 2.18. They showed that defect-tolerant design concepts could easily be applied to additive materials with surface roughness and internal porosity and that the wide scatter of fatigue life properties was reduced if the defect size was taken into account. The fatigue strength data that they collected followed the El-Haddad model and supported the application of extreme value statistics to prediction of fatigue strength of additive alloys. Romano *et al.* [73–75] proposed the method of introducing artificial defects to define a lower S-N curve bound. They also developed a model based on extreme value statistics for fatigue life estimation in high cycle fatigue (HCF) regions of fatigue life which described the experimental scatter in the fatigue life data. This model included special consideration of surface volume defects to further reduce error in life prediction.

2.5 Contributions

The literature review presented in this chapter shows that a significant amount of work has been performed previously to understand the processing, structure, properties, and performance disciplines separately. The work performed in this document stems from a recognition that the implementation of additive materials in structural aerospace applications requires a thorough understanding of all four of the aforementioned PSPP disciplines and their interactions with each other. The purpose of this dissertation will be to approach porosity in AM components in light of the PSPP framework and trace the influence of AM processing to fatigue performance of porous additive materials. The insight gained from the proposed investigations will help inform process optimization efforts which will facil-

itate implementation of additive components in aerospace applications. More specifically, the contributions of this work are to:

1. Examine PPP trends across laser powder bed fusion (LBPF) process space
2. Interrogate literature porosity prediction models using experimental data
3. Develop a pore-based fatigue life prediction method
4. Identify beam PPP influence on fatigue life
5. Quantify fatigue life debit induced by a pore of a given size compared to fatigue life of wrought alloy
6. Adapt fatigue limit prediction methodologies to predict finite life using pore and stress data.
7. Identify critical pore size for achieving a infinite/finite life for a given stress state
8. Develop a compliance-based characterization method for rapid characterization of fatigue performance of AM materials

PPP Influence on Component Density and Pore Size Characteristics

3.1 Introduction

Additive material consistently exhibits pores and internal defects that have been shown to come from several different sources including raw material, insufficient melting, and over-melting. As discussed in Chapter 2, several authors have discussed various mechanisms for pore development in additive material with respect to AM process parameters, but very few have taken the opportunity to explore wide regions of process space to determine the influence of several process parameters and their interactions on the production of porosity in AM materials. Before one can fully understand and predict fatigue behavior of additive components, it is important to understand how pore populations are formed and to determine how and why population characteristics change throughout AM process space.

3.2 Materials and Methods

In this initial investigation, two AM builds were performed to characterize the effects of four PPPs, beam power, scan speed, hatch spacing and layer thickness, on porosity defects in LPBF nickel-based superalloy 718 components. Over fifty 12.25 mm (0.5 in) diameter

by 12.25 mm tall cylinders were manufactured during each build using an EOS M290 system (see Figure 3.1). Each component contained a notch to help register the orientation of the cylinder on the plate. The first build was conducted at the nominal beam power and a constant 20 μm layer thickness ("low" setting). The build was designed as a modified factorial experiment with the multi-level factors of scan speed and hatch spacing. The scan speed limits for the experiment were set to +/- 20% of the nominal value for scan speed, and the hatch spacing limits were set to +/- 50% of the nominal value for hatch spacing. The structure of the design is shown in Figure 3.2.

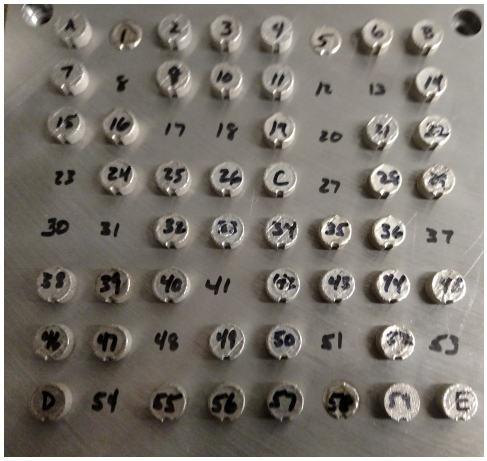

Figure 3.1: Experimental build layout for Low layer thickness

The low layer thickness build was structured so that the majority of the PPP treatments

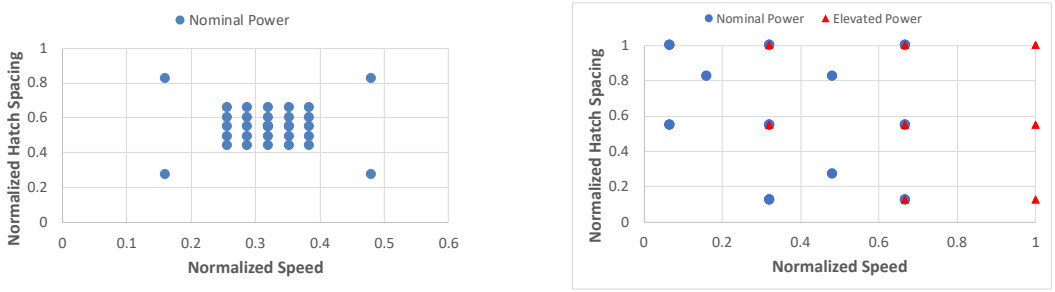

(a) (b)

Figure 3.2: a) Design of experiment structure for low layer thickness at nominal power. b) Design of experiment structure for high layer thickness. Blue circles indicate nominal power and blue triangles indicate elevated power.

were compactly centered around the nominal hatch spacing and speed with four outlying PPP treatments surrounding them. Multiple replicates of each treatment were included in the experiment design. High VED PPP treatments experienced overmelting, and these components caused the machine to jam when the hard recoater blade impacted them. The failure occured within the first few layers of the build, so the remainder of these particular components were removed from the experiment, and the build was restarted.

A second build was performed with a layer thickness of 40 μm ("High" setting). During the high layer thickness build, two power settings (nominal and high) were investigated, and the ranges of hatch spacing and speed were extended to more extreme settings. To prevent the build from crashing as it did in the previous experiment, high VED settings were removed from consideration. For both experiments, there was some design overlap to ensure continuity in models that were developed.

Once the specimens were electron discharge machined (EDM'd) off the plate, they were mounted and polished to a mirror finish. Each specimen was imaged using a Phenom XL tabletop scanning electron microscope at a magnification of 500x. The entire cross-section was imaged, and ImageJ [76] was used to convert the grayscale images to binary images. Each pore's equivalent diameter ($\sqrt{Area}$) and circularity ($4\pi\left(\frac{Area}{Perimeter^2}\right)$) were measured. Additionally, each layer's pore density was approximated as the difference of the total pore area fraction from unity. This process was performed for at least four cross-sections of each specimen, so that defects throughout the depth of the component could be analyzed. For each measured quantity, the data from each layer was combined, so that a distribution from each component could be observed.

3.2.1 Regression Methodology

Once the data was collected from each specimen, the mean of each component distribution was calculated. These calculated quantities were matched with their PPP settings, and a regression analysis was performed to develop second-order linear models for layer density,

pore diameter and pore circularity. The model was constructed in the form of Equation 3.1 such that the β terms are the effect coefficients, ϵ is the error term, and Q^*, S^*, H^*, and L^* are normalized power, speed, hatch spacing and layer thickness respectively. Quadratic and linear interaction terms were included for hatch spacing and speed, but only linear terms and interactions were included for beam power and layer thickness.

$$\begin{aligned} f(Q*, S*, H*, L*) = \beta_1 + \beta_2 Q^* + \beta_3 S^* + \beta_4 H^* + \beta_5 L^* + \beta_6 Q^* S^* + \beta_7 Q^* H^* + \beta_8 S^* H^* \\ + \beta_9 L^* Q^* + \beta_{10} L^* V^* + \beta_{11} L^* H^* + \beta_{12} S^{*2} + \beta_{13} H^{*2} + \epsilon \end{aligned} \tag{3.1}$$

Three models were constructed (density, diameter, circularity) from the average metric data using the least-squares approach described below. Each component (i) was considered to be a separate training point (x_i) in order to give insight into the component to component variability. First, a system of equations representing each data point was constructed from Eq. 3.1 including every experimental observation such that:

$$\begin{bmatrix} 1 & Q_1^* & S_1^* & H_1^* & L_1^* & Q_1^*S_1^* & Q_1^*H_1^* & S_1^*H_1^* & L_1^*Q_1^* & L_1^*V_1^* & L_1^*H_1^* & S_1^{*2} & H_1^{*2} \\ 1 & Q_2^* & S_2^* & H_2^* & L_2^* & Q_2^*S_2^* & Q_2^*H_2^* & S_2^*H_2^* & L_2^*Q_2^* & L_2^*V_2^* & L_2^*H_2^* & S_2^{*2} & H_2^{*2} \\ \vdots & \vdots & \vdots & \vdots & \vdots & \vdots & \vdots & \vdots & \vdots & \vdots & \vdots & \vdots & \\ 1 & Q_N^* & S_N^* & H_N^* & L_N^* & Q_2^*S_N^* & Q_N^*H_N^* & S_N^*H_N^* & L_N^*Q_N^* & L_N^*V_N^* & L_N^*H_N^* & S_N^{*2} & H_N^{*2} \end{bmatrix} \begin{bmatrix} \beta_1 \\ \beta_2 \\ \vdots \\ \beta_N \end{bmatrix} + \begin{bmatrix} \epsilon_1 \\ \epsilon_2 \\ \vdots \\ \epsilon_N \end{bmatrix} = \begin{bmatrix} y_1 \\ y_2 \\ \vdots \\ y_N \end{bmatrix} \tag{3.2}$$

where y_i is the i^{th} observation and

$$\begin{bmatrix} \epsilon_1 \\ \epsilon_2 \\ \vdots \\ \epsilon_N \end{bmatrix} = \begin{bmatrix} y_1 \\ y_2 \\ \vdots \\ y_N \end{bmatrix} - \begin{bmatrix} \hat{y_1} \\ \hat{y_2} \\ \vdots \\ \hat{y_N} \end{bmatrix} \tag{3.3}$$

where $\hat{y}_i$ is the regression predicted value.

The system of equations is solved for the β terms that best fit the model to the experimental data. To ensure the accuracy of the model and to determine whether the calculated β terms are appropriate for the measured data set, analysis of variance (ANOVA) is per-

formed on each response model to approximate error variance and to determine its source.

3.2.2 ANOVA Methodology

ANOVA is a tool that compares the variance in two treatments and determines the probability that the two treatments belong to the same data set. It is also used to analyze error estimates from regression models and predict whether the model accurately reflects the data. In order to determine the goodness of fit, the sum of squares for the response degrees of freedom (DOF), error DOFs and total DOFs are calculated respectively as follows:

$$SSR = \sum_{i=1}^{N} (\hat{y}_i - \bar{y})^2, \tag{3.4}$$

$$SSE = \sum_{i=1}^{N} (y_i - \hat{y}_i)^2 = \sum_{i=1}^{N} \epsilon_i^2, \tag{3.5}$$

and

$$SST = SSR + SSE \tag{3.6}$$

where $\bar{y}$ is the average of the regression responses for the experimental treatments. SSR represents the difference between the groups, SSE characterizes the variation within each group, and SST describes the total variation. For an example case, suppose N data points were obtained during an experiment, and a regression model with v unknowns were used to describe the response. One DOF would be used to find the average response ($\bar{y}$), therefore the number of DOFs required to find SSR would be $v-1$, and the number of DOFs required to calculate the total variation (SST) would be N-1. Therefore, the remaining DOFs ($N-v$) would be used to calculate SSE.

In the real experiment, sixty-nine observations were made, and Eq. 3.1 ($v = 13$ unknowns) was used to describe the response. Therefore, the DOFs to calculate SSR, SSE, and SST were distributed as observed in Table 3.1. Once the sum of squares quantities

were calculated, the Mean Sum of Squares for each DOF was calculated by dividing the respective sum of squares by the number of DOFs used to calculate it.

Table 3.1: DOF summary for the porosity experiment

SS	DOF		MS
SSR	$v-1$	12	$\frac{SSR}{12}$
SSE	$N-v$	56	$\frac{SSE}{56}$
SST	$N-1$	68	$\frac{SST}{68}$

After the sums of squares were calculated, an F-statistic (F^*) was calculated for each model based on the ratio of the Mean Sum of Squares from the regression and the error respectively ($F^* = \frac{MSR}{MSE}$), and the corresponding p-value (p) was calculated from the cumulative distribution function (CDF) of the F-distribution such that

$$p = 1 - F_{v-1,N-v} \tag{3.7}$$

where F represents the F-distribution CDF. The p-value represents the probability that the experimental data can best be described using the mean value of all the data or the probability that the treatment to treatment variation is the same. If this p-value is below 0.05, there is sufficient evidence from the experimental data that the regression model represents the data more appropriately than the mean of the experimental data. If the P-value is larger than 0.05, there is not enough evidence to support this hypothesis.

The error sum of squares (SSE) may be examined more closely, and the source of the variation may be determined to be from either pure (random) error or from lack of fit error which is a result of an insufficient modeling technique. The sum of squares for pure error (SS_{PE}) and the sum of squares for lack of fit error (SS_{LF}) terms sum together to equal the SSE. In order to determine if the model is appropriate for the collected data, SS_{PE} may be

calculated as

$$SS_{PE} = \sum_{i=1}^{N} \sum_{j=1}^{M} (y_{i,j} - \hat{y}_{,j})^2 \tag{3.8}$$

where $y_{i,j}$ represents the i_{th} replicate in the j_{th} PPP treatment and

$$SS_{LF} = SSE - SS_{PE}. \tag{3.9}$$

The number of DOFs required for SS_{PE} is given by

$$DF_{PE} = \sum_{j=1}^{M} (n_j - 1) \tag{3.10}$$

where n_j is the number of data points obtained for each treatment. The number of DOFs required for SS_{LF} is the difference between DF_{PE} and the total number of SSE DOFs. The mean sum of squares for pure error (MS_{PE}) and lack of fit (MS_{LF}) can be calculated by dividing SS_{PE} and SS_{LF} by their respective number of DOFs, and a corresponding F-statistic can be calculated as the ratio of MS_{LF} to MS_{PE}. The corresponding p-value can be calculated from the cumulative distribution function (CDF) of the F-distribution such that

$$p = 1 - F_{DF_{LF}, DF_{PE}}. \tag{3.11}$$

The p-value represents the probability that model error variation is not due to lack of fit error or the probability that the model error variation is due to pure random error. If the p-value is below 0.05, there is sufficient evidence to suggest that the lack of fit error is significant, and the model used in the regression is inappropriate for the experimental dataset. If the P-value is larger than 0.05, the error in the model probably occurs randomly and not due to a lack of fit. Another value that is often used for reference is the R^2 value which represents the proportion of the variation which is explained by model. The maximum

variation that a specific model will explain is given by:

$$R^2 = 1 - \frac{SS_{PE}}{SST}. \tag{3.12}$$

A majority of the rest of the variation can be described by random error. The combination of total regression ANOVA, lack of fit analysis, and R^2 calculations can give a good indication as to whether the proposed model sufficiently represents the experimental data. These analyses were highlighted for each of the three models developed in this chapter.

3.3 Results and Discussion

In order to fully understand each PPP's role in producing porosity characteristics and its interaction with other PPPs, data from the two AM builds were analyzed via ANOVA and regression analysis. This model was examined extensively, and the data was collapsed into mechanism-based models that shed light on physical phenomena and their role in porosity formation.

3.3.1 Pore Distribution Quantification

It will be important for subsequent studies to identify the key characteristics of the pore size distributions, so some brief observations will be made here. Once the pore size data was compiled for each specimen, histograms were prepared of the pore sizes, and appropriate probability distribution functions were fit to the data. It was observed that a large majority of the observed pores exhibited very small diameters and that number of pores decreased significantly as size increased as observed in Figure 3.3. Therefore, a lognormal distribution was selected to represent each porosity distribution. A probability plot was examined for each distribution to verify that the distribution did indeed reflect a lognormal

distribution. The choice of distribution type was confirmed based on these observations.

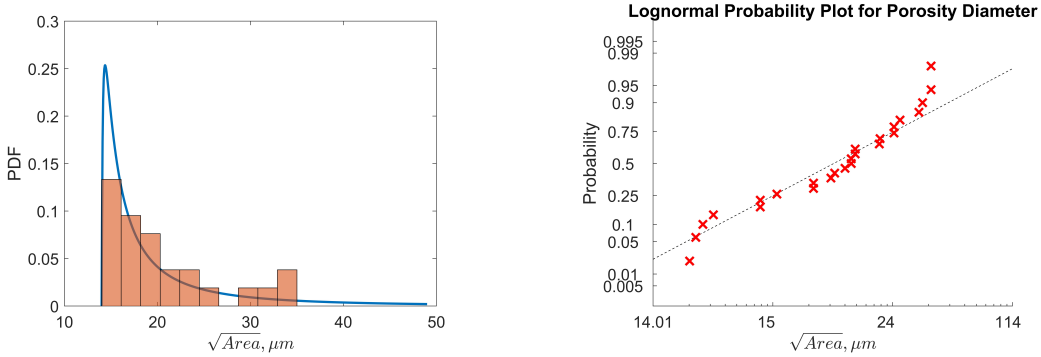

(a) (b)

Figure 3.3: (a) Typical lognormal distribution observed for diameter and (b) its lognormal probability plot showing the diameter distribution follows a lognormal trend

Figure 3.3a shows qualitatively that the pore diameter histogram lines up with an offset lognormal distribution where the offset accounts for the thresholding performed to remove very small pores. Additional verification of the lognormality of the distribution is observed in Figure 3.3b. An ideal lognormal distribution will follow the dotted line. The majority of the experimental data does indeed follow this line with slight deviations in the tails of the distribution. The tail deviations indicate that the minimum and maximum pore sizes are clearly defined in this dataset which is contrast to the actual distribution. The lower tail drops off at approximately 14 μm which is the threshold value used in the experiment. The upper tail approaches approximately 34 μm which as the histogram shows is approximately the same as the maximum pore diameter. For a larger dataset, these tails should be examined more closely and conclusions should be drawn about the extreme values of pore size in AM porosity distributions.

3.3.2 Qualitative Pore Observations

Initial observations of pore occurrences show definitive regions of process space in which pores are more likely to appear in the components, but some regions exhibit elongated,

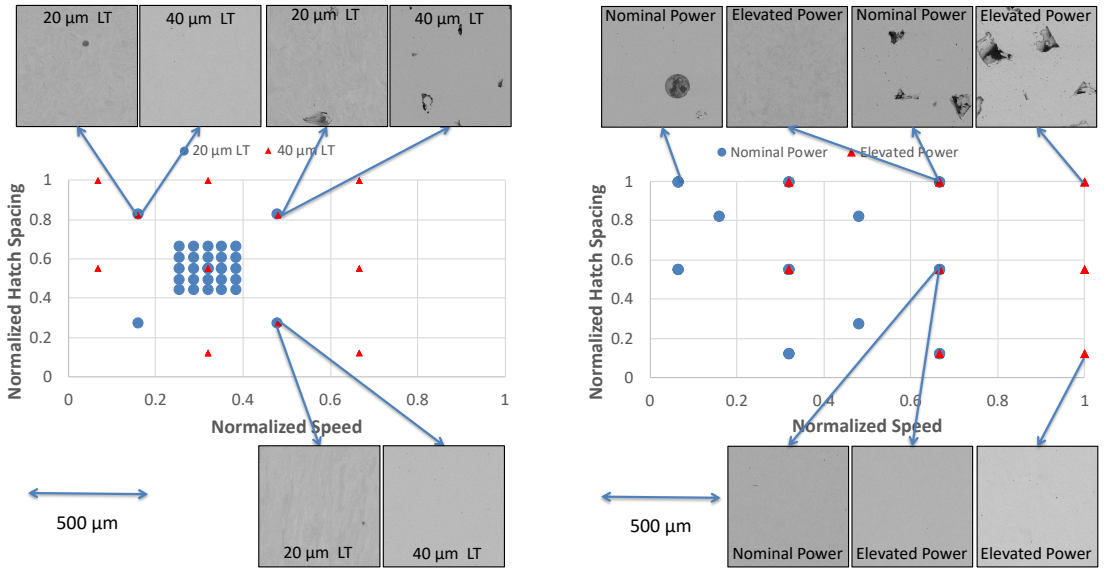

(a) (b)

Figure 3.4: Micrographs showing the porosity formation in a) the layer thickness comparison and b) the beam power comparison.

polygonal pores while others exhibit large circular pores. Between both experiments, there was a single region in the center of the process space in which there was little to no porosity observed. The porosity in the central region is very small and likely caused by entrapped gas from the powder manufacturing process or small LOF regions where possible large powder particles and/or random fluctuations of PPPs occurred during the component manufacturing process. Example micrographs for both experiments are shown in Figure 3.4.

Figure 3.4a shows that lower VED regions exhibit more porosity than mid-range and low VED regions, but qualitative comparisons between small and large layer thicknesses and low and high powers show drastic changes in porosity content. Figure 3.4a exhibits minimal porosity at the large hatch spacing/low speed and high speed/small hatch spacing settings, but much larger porosity at the high speed/large hatch spacing condition. Furthermore, increasing the layer thickness seems to increase the porosity observed in the high speed/large hatch spacing setting. It can also be seen that the porosity at large hatch spacing settings transition from large polygonal pores to small spherical pores. In that low

speed region, though, porosity is diminished by increasing the layer thickness and effectively decreasing the VED.

Similarly, Figure 3.4b indicates a transition from large spherical keyhole porosity to very small porosity to large polygonal LOF. Elevated power seems to show fewer, smaller pores than nominal power specimens. At smaller hatch spacing settings, porosity gets much smaller and is barely noticeable from a macroscopic view.

3.3.3 Porosity and Density Regression

A metric that has been used historically to define the quality of a build and describe the porosity content within the components is component percentage density. Several methods have been developed to measure this quantity, but the metallographic cross-section method described herein allows for high precision measurements at multiple cross-sections. It is flexible and inexpensive which makes it a good option, but it also limits the number of measurements that may be taken due to the time-intensive nature of polishing, cleaning, and imaging a large number of specimens. For this investigation, four cross-sections for each specimen were obtained which totals between eight and twenty random cross-sections for components manufactured via the same PPPs. This number of measurements per specimen was considered sufficient to capture an average density value for each specimen. Eqs. 3.13, 3.14, and 3.15 give the equations obtained using least squares regression for mean density, mean diameter, and mean circularity.

$$\begin{aligned} f_{Density} = {} & 1.0852 - 0.4962Q^* - 0.2413S^* - 0.1931H^* + 0.6197L^* \\ & + 1.302Q^*S^* + 0.9471Q^*H^* - 0.6227S^*H^* - 0.8547L^*Q^* \\ & + 0.0361L^*V^* + 0.0236L^*H^* - 0.4674S^{*2} - 0.2492H^{*2} \end{aligned} \tag{3.13}$$

$$f_{Diameter} = -56.9983 + 229.9595Q^* + 122.5746S^* - 1.5402H^* - 124.2101L^* - 428.0683Q^*S^* - 239.0156Q^*H^* + 152.8604S^*H^* + 178.1882L^*Q^* - 42.9649L^*V^* + 25.0858L^*H^* + 160.4902S^{*2} + 81.9233H^{*2} \quad (3.14)$$

$$f_{Circularity} = 1.0774 - 0.7111Q^* - 1.1043S^* - 0.5625H^* + 0.7173L^* + 1.8206Q^*S^* + 1.0462Q^*H^* + -0.739S^*H^* - 0.9885L^*Q^*0.7455L^*V^* + 0.3407L^*H^* - 0.7155S^{*2} - 0.2454H^{*2} \quad (3.15)$$

Total regression ANOVA and lack of fit analyses were performed for each model, and the results are summarized in Tables 3.2, 3.3, and 3.4. Tables 3.2 and 3.3 show that for

Table 3.2: ANOVA summary table for Mean Density

	SS	**DOF**	**MS**	**F**	**p-value**	**R^2**
Regression	7.48e-2	12	6.23e-3	16.9807	**1.62e-14**	**0.8073**
Error	2.05e-2	56	3.67e-4	-	-	-
Pure Error	*1.84e-2*	*37*	*4.96e-4*	-	-	-
Lack of Fit Error	*2.18e-3*	*19*	*1.15e-4*	*0.2316*	***0.999***	-
Total	9.53e-2	68	-	-	-	-

Table 3.3: ANOVA summary table for Mean Pore Diameter

	SS	**DOF**	**MS**	**F**	**p-value**	**R^2**
Regression	7620	12	635	15.42	**1.189e-13**	**0.8515**
Error	2306	56	41.18	-	-	-
Pure Error	*1474*	*37*	*39.83*	-	-	-
Lack of Fit Error	*832.56*	*19*	*43.82*	*1.10*	***0.389***	-
Total	9926.1	68	-	-	-	-

both the density and diameter, the mean sum of squares of the regression (MSR) is much larger than the mean sum of squares of the error (MSE) which indicates that at least one β term in the model (other than the intercept term) is statistically greater than zero and that

Table 3.4: ANOVA summary table for Mean Pore Circularity

	SS	DOF	MS	F	p-value	R^2
Regression	0.5903	12	4.92e-2	9.8882	**5.50e-10**	**0.8987**
Error	0.2786	56	4.97e-3	-	-	-
Pure Error	*0.0880*	*37*	*2.378e-3*	-	-	-
Lack of Fit Error	*0.1906*	*19*	*1.003*	*4.217*	***8.933e-5***	-
Total	0.8689	68	-	-	-	-

the model is non-trivial (i.e. it represents the data better than an average of all the data). The certainty of this conclusion is demonstrated by a p-value very close to zero. Any p-value less than 0.05 indicates that the model is non-trivial. Further evaluation of the error sum of squares for mean density shows that the pure (random) error for each DOF (MS_{PE}) is approximately four times larger than the lack of fit error (MS_{LF}). This results in a p-value (0.999) which indicates that there is less than a 1% chance that the error variation is due to a lack of fit. For the mean pore diameter, MS_{PE} is almost equal to MS_{LF} which results in a p-value of 0.389. This means that there is a 38.9% chance that the error term variation is not due to model lack of fit (i.e. There is a 61.1% chance that the error term variation is due to pure random error.) While these numbers are not convincing from an intuitive standpoint, the statistical interpretation is that there is not enough evidence to support the hypothesis that the error observed between the mean diameter model defined by Eq. 3.14 and the experimental data is due to lack of fusion. Therefore, it must be assumed that the error is due to pure, random error. For both models, the R^2 calculation indicates that the proportion of the response variation that the model will describe is greater than 80 %, and the rest of the variation may be described by random error in the response.

Similarly, Table 3.4 shows that the probability that all of the β values in Eq. 3.15 are effectively zero is very low. Indeed, the p-value indicates that there is evidence to support the hypothesis that treatment to treatment variation is accounted for in the model. Further examination of the error, however shows that the MS_{LF} is much larger than MS_{PE}. In fact, the p-value indicates that there is almost no chance that the error observed between

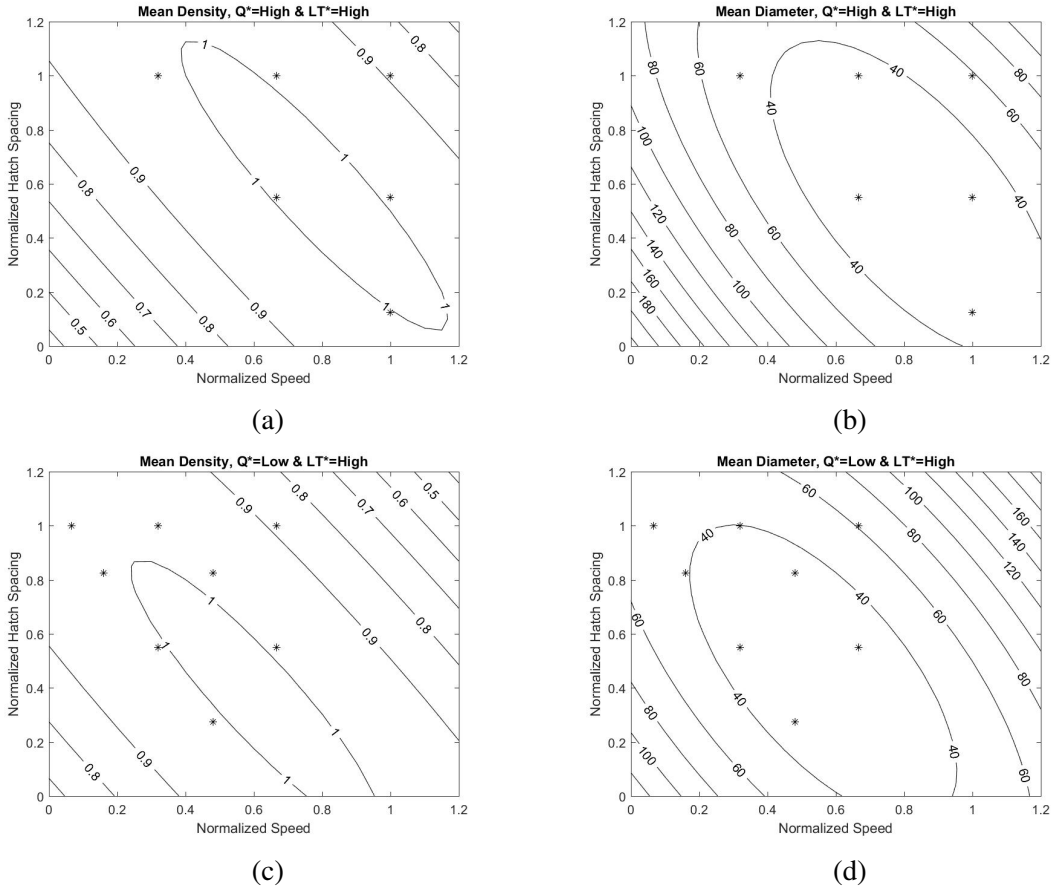

Figure 3.5: Regression trends for mean layer density (a & c) and mean pore diameter (b & d) for thick layers and high and low powers.

the experimental data and the model is due to lack of fit. Therefore, the model specified in Eq. 3.15 is not appropriate to represent this data, and another model should be developed to accurately represent pore circularity across process space.

The model form that was proposed in Eq. 3.13 leveraged the highest level terms allowed by the number of treatments performed. Adding higher order terms would result in overfitting the data and would increase the risk of mispredicting responses in regions where experimental data does not exist. For this reason, until more data is available, pore circularity will not be examined any further, and the following discussion will focus solely on mean density and mean pore diameter.

Figure 3.5 shows the trends for both layer density and pore diameter as hatch spacing,

speed, and beam power vary. Initial inspection shows that layer density does not seem to depend on layer thickness according to the model. This is counter-intuitive because an increase in layer thickness has been connected with increased porosity [27] because the amount of material that must be melted to fuse the current layer to the previous layer is much greater. If the melt pool region does not fully penetrate the powder into previous layers, LOF porosity will occur. In contrast, if the powder layer is too thin, it is possible that over-melting will occur and keyhole porosity will develop.

One possibility for why the model does not predict a change in layer density for different layer thicknesses is that the measured data for one of the layer thickness settings does not extend as far as the data from the other thickness setting. The low layer thickness build was designed with a very narrow spread of hatch spacing and scan speed settings compared to the high layer thickness build. Both experiments were centered around the nominal settings, and the component densities measured within a small radius of the experiment center were very close to 100% dense as can be seen in Figures 3.5a and 3.5c. A significant decrease in density did not occur until the settings reached their extreme values (High Speed-Large Hatch Spacing, Low Speed-Small Hatch Spacing). If the first experiment had contained a much wider range of beam settings, the layer thickness may have played a much more prevalent role in this component density model.

In general, however, Figures 3.5a and 3.5c (obtained from Eq. 3.1) show expected behavior. Component density stays relatively constant at about 100% dense from the top-left to bottom right. This is intuitive because an increase in speed will reduce the melt pool width. In order for the density to remain constant, the hatch spacing must also decrease to maintain a similar melt pool overlap. Additionally, interaction effects can easily be seen between the scan speed and hatch spacing settings. For low speeds, increasing hatch spacing increases density while at high speeds, increasing hatch spacing decreases component density. Similarly, for large hatch spacings, increasing speed decreases the density of the component, and for small hatch spacings, increasing speed increases the component density

up to a certain point, beyond which the density begins to decrease again as speed continues to increase. This last interaction clearly shows the transition from LOF porosity to fully dense material to keyhole porosity.

Pore diameter shows a similar trend to layer density where the optimum region traverses the plot from the top left to the bottom right. This trend is also intuitive because an increase in speed will reduce the melt pool width, and a decrease in hatch spacing is necessary to maintain the overlap required for a fully dense component. Contrary to the behavior observed in the layer density model, pore diameter *is* dependent on layer thickness. More specifically, the average pore diameter increases as layer thickness increases from the low to high settings. Figures 3.5b and 3.5d show the trend of pore diameter at a constant layer thickness (high setting). The surface is increased slightly for the nominal layer thickness, but for the sake of visualization, a single surface for each power has been displayed. The linear dependence of pore diameter on layer thickness and power is assumed based on the number of DOFs available, but a more in-depth study may indicate that the dependence is actually non-linear.

Examination of Figures 3.5b and 3.5d shows clear transitions from mid-sized keyhole induced porosity to large LOF pores, and both figures show a non-zero minimum point which indicates that the as-built material never reaches 100% density. This may be due to gas porosity that is captured in the material even at optimal PPP settings. This can occur as a result of gas entrapped in the powder stock [77]. Gas porosity must be accounted for in the design of structural components because defects have been shown to drive failure. It has been seen, however, that small pore sizes do not necessarily cause a life detriment in AM components because microstructural defects can dominate crack initiation [8, 9]. In addition, there is evidence that a critical flaw size exists for a certain stress state such that any pore below that critical threshold is not likely to cause catastrophic failure. El-Haddad showed that some critical crack length (l_0) exists below which crack non-propagation will be dominated by the material fatigue limit behavior and above which crack non-propagation

will be dominated by the SIF threshold of the material. Romano modified El-Haddad's critical crack length to include small crack effects of porosity [69, 74]. Therefore, incorporating gas porosity into a design framework is possible to increase the reliability of AM components.

3.3.4 Melt Pool Shape Model

As mentioned in 2.3.1, Tang et al. proposed a density model that can predict LOF density changes based on assumed melt pool dimensions. These dimensions were obtained from the Rosenthal point source heat transfer solution. It is well known that the Rosenthal solution, while useful for steady state assumptions, is limited in its application to transient problems. It assumes pure conduction and neglects powder, phase change, and internal convection effects on the melt pool geometry. Some of these deficiencies can be accounted for through the use of a "fitting" variable (α) in which the variable is modified so that the model melt pool dimension matches the experimental dimension. For this study, the initial fitting value $\alpha = 0.57$ was used based on previous work [14, 15].

If the melt pool is assumed to be a quasi-elliptical shape as proposed by Tang, monitoring the overlap of melt pools in both the vertical and horizontal directions as described by Eq. 2.1 gives a usable criterion to determine what PPPs will produce LOF porosity. To verify this assumption, Eq. 3.13 was combined with the Rosenthal solution. The low power and high layer thickness setting was the only data subset which produced noticeable, systematic LOF throughout the build. Therefore, only this setting was interrogated for this model. The melt pool depth and width for the high power setting and a range of speeds were calculated numerically from the Rosenthal solution, and the values for mean density were calculated from Eq. 3.13 using the same power and speed values, a range of hatch spacing values and a single layer thickness value. The metrics $\frac{H}{W}$ and $\frac{L}{D}$ were calculated and the values from Eq. 3.13 were plotted as a function of these two metrics as shown in Figure 3.6. In this investigation, the value of D was determined to be the distance from the

top of the melt pool to the bottom of the melt pool and assumes that the powder layer is included in the melted material. This differs from Tang's approach in which the depth of the melt pool was comprised of the melted substrate depth and the added material depth.

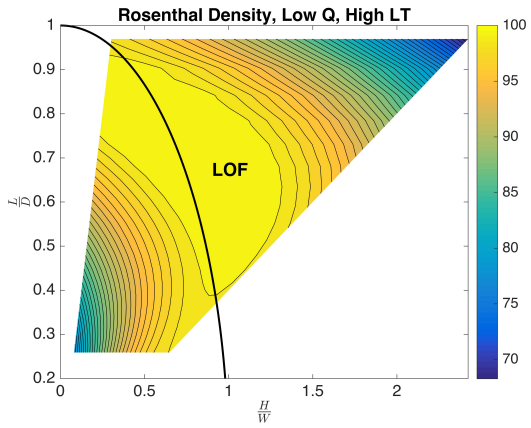

Figure 3.6: Mean density as a function of hatch spacing to width and layer thickness to depth as calculated by the Rosenthal solution assuming a low power setting, a high layer thickness setting, and varying speeds and hatch spacing settings (fitting variable $\alpha = 0.57$)

A black contour representing Eq. 2.1 was overlaid on the plot such that all data between that curve and the upper right corner of the plot signifies the LOF zone. Tang's criteria appears to predict the threshold for LOF porosity reasonably well.

One weakness of this method is that the predictor is a simple approximation. The Rosenthal solution does not take melt pool to melt pool interactions, surface tension, or powder effects into account, so it is difficult to obtain an accurate representation of melt pool shape and pore density for a wide region of process space. An improvement that could be made in future work is to observe the actual melt pool size and perform a fitting operation to the Rosenthal model to more accurately represent the melt pool size across process space. In spite of this, Tang's criteria does provide a first-order approximation which provides some insight into LOF production in AM material.

One observation that is easily made in the melt pool shape context, however, is that LOF porosity relies on $\frac{H}{W}$ and $\frac{L}{d}$ which interact with each other. Therefore, LOF can occur in three different modes, and the LOF mode observed depends on the interaction of these

two terms. The LOF modes are identified below:

1. A melt pool that does not reach a sufficient depth to melt the entire powder layer ($\frac{L}{D} \rightarrow 0$)

2. A melt pool that does not have sufficient lateral overlap due to the hatch spacing being too large ($\frac{H}{W} \rightarrow 0$)

3. A combination of the previous two modes

Each of these LOF types obtained from non-optimal PPPs introduce distinct material structure that are detrimental to properties and mechanical performance of a component. Insufficient melt pool depth produces planar LOF which poses significant mechanical property and performance detriments to components in both tensile and shear loading conditions. Additionally, planar pores can be very difficult to detect using NDE because they are typically very thin. Excessive hatch spacing distance can cause linear, polygonal LOF perpendicular to the build direction which can easily initiate and propagate cracks in fatigue. A significant amount of LOF occurs due to stochastic or unintentional PPP variation during the build process. Disturbances in the powder layer change layer thickness; machine hygiene and atmospheric conditions vary the powder absorptivity which changes melt pool dimensions; and component size and build order change the amount of thermal energy stored in the previous layers. Each of these observations induce LOF porosity through a combination of $\frac{H}{W}$ and $\frac{L}{d}$ variations.

3.3.5 VED Model

The VED model has been used extensively to describe the amount of energy being put into the system. It has been observed that modifying the VED of a process effectively changes the output quantity of interest including microstructure size, component density, and material properties and performance. Typically, comparisons are made by holding all but one

variable constant and making VED a function of only one variable. It can be seen from Figure 3.7 that as a function of multiple variables, the density values do not converge to a single curve. This indicates that generalizing the structure-properties-performance relationship based on this metric does not *necessarily* give insightful information (e.g. Constant VED induced via several combinations of process parameters does not provide the same mean component density.)

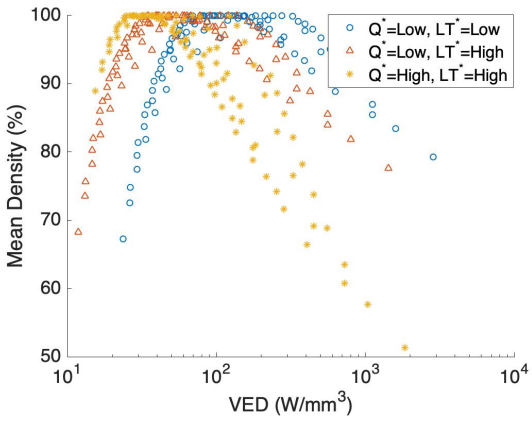

Figure 3.7: Mean density with respect to VED as obtained from Eq. 3.13

Figure 3.7 shows, however, that reducing the VED equation to a function of two variables (Speed and Hatch Spacing) reduces the scatter band significantly. Taken as a whole, the data presented in Figure 3.7 gives no observable trend, but separating the data with respect to the power and layer thickness settings (as visualized by the different colors) shows a much more meaningful trend. Each data series in 3.7 shows less variation in density at lower VEDs compared to the higher VED measurements. This could indicate that a functionally reduced VED metric could be reasonably applied to predicting material structure, properties and performance in low-VED processing applications. This observation supports prior work. Keyhole mode melting is not easily modeled or observed using this framework because it does not account for the material behavior which is integral to the keyhole threshold.

3.3.6 Normalized Enthalpy Model

King's thermodynamics-based normalized enthalpy model, (Eq. 2.2) on the other hand, has been shown to accurately predict the formation of keyhole mode melting for single bead geometries. An attempt has been made here to apply this model to bulk components and determine its utility in predicting porosity for geometries other than single beads. The material properties for alloy 718 were collected from multiple sources [45, 78] and are tabulated in Table 3.5.

Table 3.5: Material properties for calculating normalized enthalpy

Material Density (ρ)	Specific Heat (c)	Thermal Conductivity (k)	Melting Temperature (T_m)	Boiling Temperature (T_b)	Spot Size (σ)
9316.33 $\frac{kg}{m^3}$	673.56 $\frac{J}{kg-K}$	28.56 $\frac{W}{m-K}$	1533 K	2500 K	70 μm

The material density, specific heat, and thermal conductivity were obtained for the solidus temperature, and the boiling temperature of the alloy was approximated to be the boiling temperature of nickel at atmospheric pressure. This element was chosen because it is the main elemental component of the material and has the lowest boiling temperature of the four major elements in the alloy. The absorption factor (α) was approximated to be 0.57 as in the Rosenthal conduction model.

The normalized enthalpy model is similar to the VED model in that it combines the effects of multiple process parameters into a single quantity to frame the results in light of a thermally related metric. It is significantly different, however, because the VED metric does not take thermodynamic or material properties into account. By incorporating these terms into the model, the stability of the melt pool can be examined more closely. In the case of the experiment described above, the density can be investigated with respect to the normalized enthalpy and the hatch spacing as shown in Figure 3.8.

It is observed that increasing enthalpy at large hatch spacings decreases the density of the component slightly, but this decrease is magnified at lower hatch spacing settings. This occurs before the threshold described in Eq. 2.2, but can potentially be attributed to keyhole

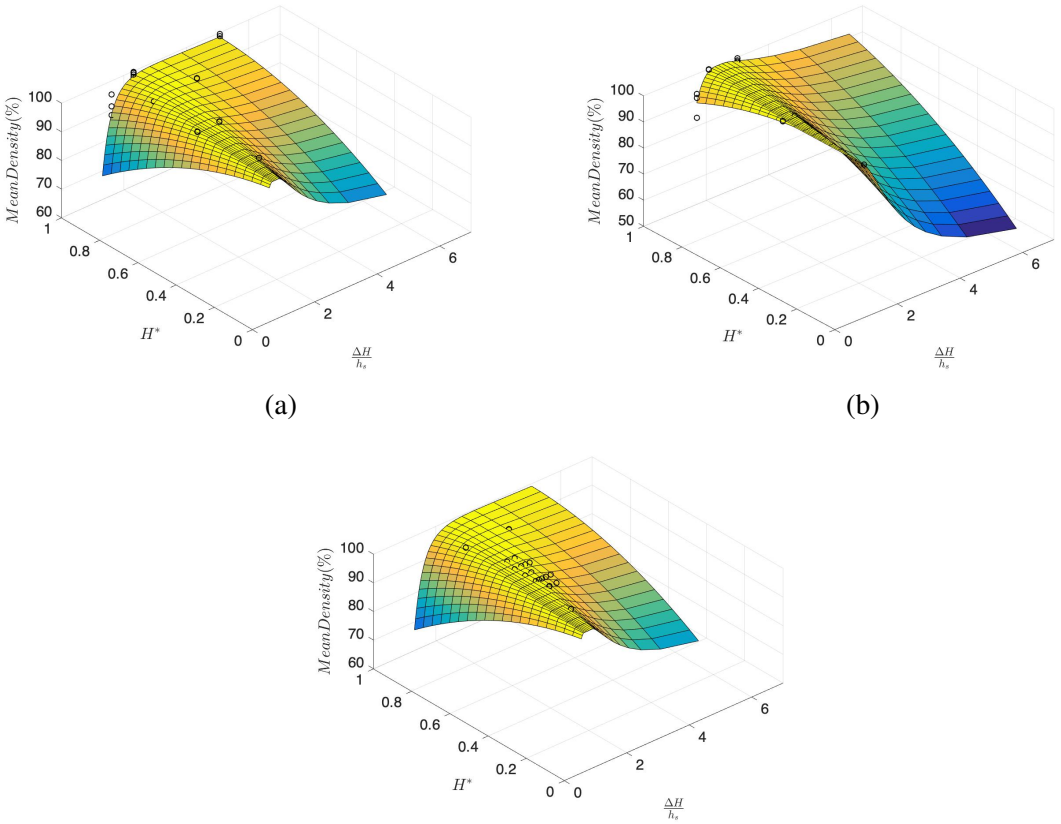

Figure 3.8: Mean Density surfaces plotted with respect to normalized enthalpy and normalized hatch spacing. a) Low Power, High Hatch Spacing; b) High Power, High Hatch Spacing; c) Low Power, Low Hatch Spacing

mode melting. It is seen that the threshold for the alleged keyhole melting decreases with a decrease in hatch spacing. This is intuitive from the model's assumption that the melt geometry is a single bead (i.e. an infinitely large hatch spacing). As the hatch spacing gets smaller, this assumption breaks down, and a lower enthalpy is required to cause overmelting and keyhole mode melting. The black circles represent the experimental data. Currently, there is little data to verify that the decrease in density predicted above is due to keyhole melting, but the trend is intuitive. Therefore, the criteria for keyhole melting described above must be modified such that the threshold value becomes a function of hatch spacing.

Power and layer thickness effects are clearly observed as well. Increasing power as seen in Figures 3.8a and 3.8b increases the amount of keyhole porosity observed at the same values of layer thickness and speed, and increasing layer thickness as seen in Figures 3.8a and 3.8c does not significantly effect the response surface in this region of process space.

3.4 Conclusion

In this investigation, explicit relationships between several PPPs and material structure have been established for LPBF alloy 718. These relationships, while specific to the experimental data collected here, establish trends that can be applied to other materials and processes. It has been shown that component density can be an appropriate metric for determining the approximate average pore size within a component, but data correlating the two quantities must be obtained in advance. It was shown that both density and pore diameter trends exhibit an optimal region and two non-optimal regions. These non-optimal regions correspond to LOF porosity and keyhole mode porosity. Pore circularity, however, showed no significant trend with process parameters for the models applied, so further work must be performed to determine how pore shape changes throughout process space.

Three models cited in the literature have been explored over the wide region of process

space used in the experiment to determine their utility in predicting porosity in bulk components. It was found that the melt pool shape and the absorbed VED quantities are amenable to LOF prediction applications, but due to the assumptions used in the respective models, they should be used with caution as first-order approximations of the true behavior. Alternatively, the third model, normalized enthalpy, is applicable to predicting keyhole mode porosity in bulk components as well as single bead geometries, but a modified threshold must be appropriated such that the hatch spacing PPP is taken into account.

Three models have therefore been verified for use in predicting porosity throughout AM process space, but a single model in and of itself is limited in its usefulness. It is only through meshing multiple models together that the entire process space can be more adequately characterized and porosity size characteristics from both LOF and keyhole mode melting can be predicted.

Life Prediction of Additive Components Based on Pore Size Distributions

4.1 Introduction

Many studies have shown that material properties of AM materials differ significantly from wrought materials [79], and AM components may exhibit notable scatter due to the large number of variables that influence the PSPP outcomes [80]. It is well known that the processing of an AM material from raw powder to final heat treatment dictates the material performance in a given application [36, 81]. The thermal history of an AM component has bearing on a wide range of material characteristics including microstructure [21, 22, 82], residual stress [83], and porosity [84, 85].

Porosity is known to dictate fatigue performance in many traditional materials. In casting, micro-porosity and shrinkage porosity were shown to act as stress concentrators which lead to crack initiation and failure [86, 87], and quantification of porosity distributions was shown to provide sufficient information to predict component life using statistical methods [88, 89]. Similarities in porosity observed in both casting and AM materials indicate that historical methods may be used to characterize the porosity content in AM components.

Beam power, raster speed, hatch spacing, and layer thickness have been varied to explore the mechanism for developing porosity in AM. It has been shown that different types

of porosity are developed by manipulating these PPPs, and that controlling the quantity, size, and morphology of porosity populations can be achieved [84]. This chapter utilizes four PPPs (power, speed, hatch spacing, and layer thickness) and multiple scan strategies that are known to influence porosity content, and explores the PPP space to further develop the understanding of the PSPP framework in relation to fatigue life of AM components. The parameters are varied to obtain various porosity distributions and the porosity is subsequently related to the fatigue life.

4.2 Materials and Methods

This chapter brings together data from two different experiments that will provide further insight into the PSPP model for AM materials from different material and processing pedigrees. In the first experiment, three scanning strategies (SS) were used, and in the second experiment, three PPP settings were used to explore the effect of processing changes on the formation of porosity. In both of these experiments, the internal porosity was measured using computed tomography (CT), and predictions were made based on these observations and the application of crack growth theory. The CT measurements were obtained using a North Star Imaging X-View X-50 machine. A summary of the experimental design is provided in Table 4.1 where A, B, and C denote the three SS and PPP settings for their respective experiment.

Table 4.1: Overview of Experiment

Machine	Concept Laser M2 Cusing			EOS M290		
Setting Name	SS-A	SS-B	SS-C	PPP-A	PPP-B	PPP-C
Power	370 W			285 W		
Velocity	700 mm/s			1000 mm/s	1150 mm/s	1400 mm/s
Hatch Spacing	0.13 mm			0.120 mm	0.110 mm	0.055 mm
Layer Thickness	0.050 mm			0.020 mm		
Scan Strategy	Continuous	CL Stripped	Island	EOS Striped		

4.2.1 Experiment 1: Scan Strategies

The components produced for the scan strategy study were manufactured using a Concept Laser^{TM} (CL) M2 Cusing LPBF machine. Alloy 718 powder was used to construct five rectangular bars on a 316L stainless steel plate. Three different scan strategies were used including CM, SM, and IM. In CM, the beam scans across the entire part in a continuous raster while in SM, a strip of width 5 mm creates multiple raster patterns across the width of the part. In IM, 25 mm^2 squares are melted at random across the entire component cross-section. For each powder layer, CM and IM undergo a 1 mm layer shift and a 90 degree layer rotation. CL's layer exposure technique also incorporates a skin and core strategy where the skin and core regions are exposed differently. The skin is exposed every layer under one PPP setting, and the core is exposed every other layer under a different PPP setting. The core material controls the fatigue performance of the component because the skin material is machined off, but it must be noted that the 50 μm shown in Table 4.1 is actually two 25 μm layers of powder that have been deposited on top of each other and subsequently exposed.

For this experiment, the core beam settings, power, speed, hatch spacing, and laser spot size, were held constant for each component as shown in Table 4.1. The components were stress relieved on the plate according to ASTM F3055 [19], EDM'd from the plate, and solution annealed and aged according to AMS 2774 [56]. Each component was machined into a round fatigue bar within the ASTM E466 standard [90], low stress ground to final dimensions (see Figure 4.1), and electro-polished to a mirror finish. The machining removed the entire skin region in the gage section and left the core material for testing. The gage section of each specimen underwent CT measurements with a 14 μm/voxel resolution, and the ImageJ (v. 1.5H) software package [76] was used to process these images and to measure the observed pores.

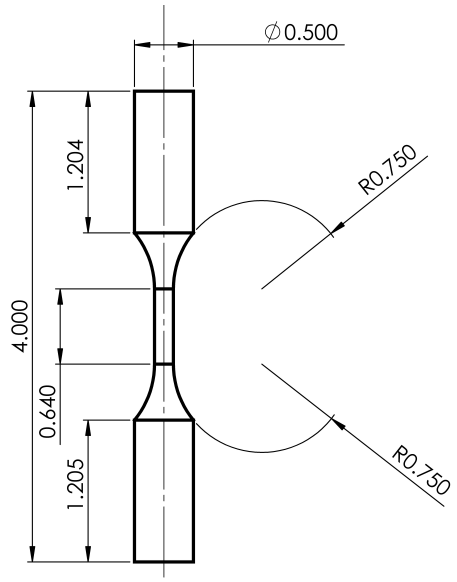

Figure 4.1: Fatigue specimen geometry based on ASTM E466 round, constant gauge section diameter specimen design

4.2.2 Experiment 2: Primary Processing Parameters

The second experiment was performed using an EOS M290 LPBF machine. Alloy 718 powder was used to construct eight rectangular bars on a 316L stainless steel plate. This experiment was to demonstrate the relationship between PPPs (power, speed, and hatch spacing), porosity content, and resulting fatigue life of AM components. Three different PPP combinations (see Table 4.1) were specified. For this experiment the stripes scan strategy was used for all bars and the beam settings were modified. The porosity in the gage section was measured using CT, and the images were analyzed via ImageJ using the same procedure as Experiment 1.

4.2.3 Raw Material and Processing

Two different powder pedigrees were used for the two experiments. The powder used in the scan strategy study had been reused approximately 10 times at the time of the build while the powder used in the PPP study had been lightly reused (<5 times). The powder morphology for both batches was observed in a NanoScience Phenom XL scanning electron

microscope. Irregularly shaped powder particles with multiple satellites were observed in both powder batches (Figure 4.2). Diligent sieving procedures and enclosed powder hoppers ensured that large powder particles were removed and the contamination level was kept low for both batches.

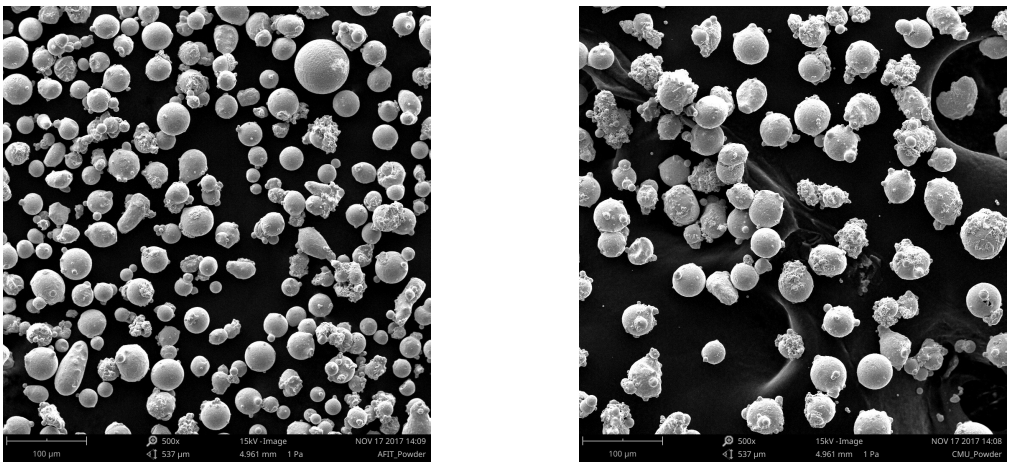

(a) (b)

Figure 4.2: Powder samples obtained from a) the SS Experiment and b) PPP Experiment.

Post process chemistry analyses were performed for five samples from both experiments, and the chemical composition for each of those specimens was determined using wet chemical analysis (Table 4.2). A representative specimen for PPP-A was not available for chemical testing at the time of the procedure, so this measurement was omitted from consideration. The chemistry of the components for each experiment were found to be within the specifications for alloy 718. Due to the consistency of the chemical composition for each of the tested components, it is assumed that the PPP-A's chemistry is consistent with the other components.

Table 4.2: Chemical Analysis of Manufactured Components

	Al	B	Cr	Cu	Fe	Mn	Mo	Ni+Co	Nb+Ta	P	Ti	C	S
Nominal	0.5	<0.006	19.00	<0.3	18.00	<0.35	3.05	Bal.	5.15	<0.015	0.9	<0.08	0.015
SS-A	0.51	<0.002	19.68	0.060	18.55	0.055	3.19	Bal.	5.09	3.1e-3	1.09	0.037	2.30e-3
SS-B	0.55	<0.002	19.35	0.062	18.36	0.013	3.21	Bal.	5.06	3.1e-3	1.07	0.036	2.60e-3
SS-C	0.54	<0.002	19.58	0.061	18.34	0.056	3.24	Bal.	5.04	3.3e-3	1.06	0.036	2.45e-3
PPP-B	0.51	<0.002	18.83	0.069	18.34	0.059	3.25	Bal.	5.06	3.3e-3	1.15	0.039	3.01e-3
PPP-C	0.52	<0.002	18.24	0.064	18.20	0.020	3.24	Bal.	5.08	3.2e-3	1.14	0.037	3.11e-3

4.2.4 Fatigue Testing

After quantifying the porosity in each specimen, load controlled, axial, room temperature fatigue tests were performed with a 100 kN MTS servo-hydraulic load frame. The maximum stress was set to 900 MPa (130 ksi) with a load ratio $R = 0.1$. Each specimen was fatigued at a linear frequency of 20 Hz until catastrophic failure occurred.

4.3 Results and Discussion

4.3.1 Experiment 1

Using image slices from the CT measurements, the porosity data were collected. For each pore, the cross-sectional area was measured, and the effective diameter was calculated. For all the slices the collective pore diameter distribution was constructed. Diameters under 14 μm were removed from consideration to account for image processing artifacts and to discard any pores smaller than the threshold crack length obtained from Konecna. Furthermore, it is assumed that fatigue failure is driven by "worst-case" phenomena, so the largest pores are expected to have the most significant effect.

Examination of the pore measurements show that the porosity content drastically changes with different scan strategies. This is illustrated in Figure 4.3 which shows the cumulative distribution function (CDF) of the pore size for each component. This function shows the percent likelihood that a certain pore size will occur within a given specimen. The red lines represent SS-A, the blue lines represent SS-B, and the green line represents

SS-C. The same scan strategies group together with SS-A exhibiting the smallest average porosity and SS-B exhibiting the largest average porosity. Qualitative observations show that in general, the pore morphologies for all of the components were large and spherical which indicates that over-melting of the material may have occurred because of non-optimal PPPs. The component porosity content indicates that the components manufactured via the SS-A strategy will perform better than components manufactured via the other two scan strategies because of the smaller maximum pore size. In addition, the average CT slice density was calculated for each component. Components manufactured with the same scan strategy exhibited similar slice density distributions, and although the average density for each component was above 99.9%, significant differences among the scan strategies were observed such that SS-A exhibited the highest average density, and SS-B exhibited the lowest average density. In comparison, the average density and the pore size distributions correlate with each other which is intuitive. The fatigue life prediction was

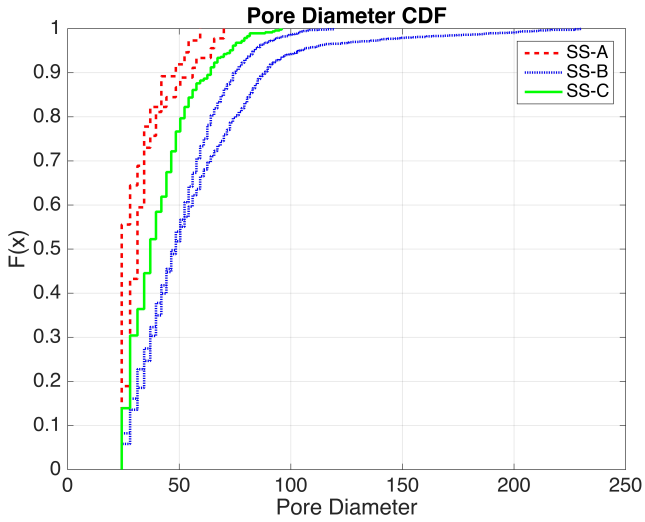

Figure 4.3: Cumulative Distribution Function of pore diameter for the SS components

made based on the maximum stress intensity calculated for each component. The pore diameter producing this stress intensity value was applied to Eq. (2.14) or Eq. (2.15) depending on its distance from the surface. When comparing the predicted life to the actual

life from fatigue testing, it was observed that estimating the fatigue life based on the largest stress intensity gave predictions that consistently lie within a 2x scatter band when compared to the actual component life. More specifically, it is seen from Figure 4.4 that SS-A performed the best while SS-B and SS-C performed at levels similar to each other. This behavior indicates that the life prediction method based on the porosity diameter distributions measured from the gage section of each component provides an accurate prediction of fatigue life that can be leveraged to qualify components and identify design criteria for AM components.

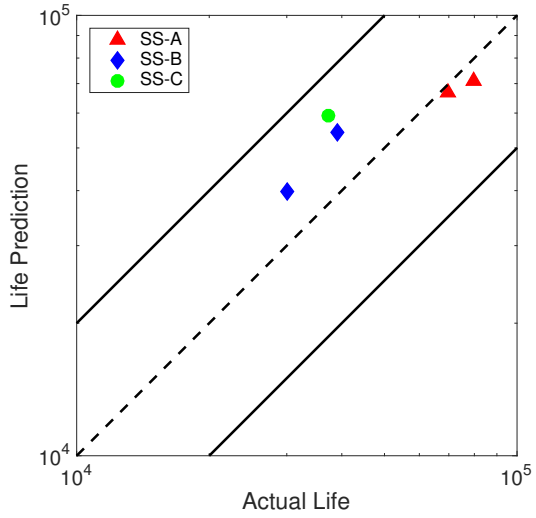

Figure 4.4: Life prediction comparison to experimental life for SS components.

4.3.2 Experiment 2

A similar analysis, as described above, was performed for the PPP study components to test whether the life prediction method can be used for components with different processing pedigree. The cross-sectional area for every pore throughout the gage section was measured from CT slices, and the pores under 14 μm diameter were again removed. PPP-A and PPP-B, which were made using similar PPP settings, both exhibited significant porosity in the gage section of each component. PPP-C, which was made with a much higher beam speed

and a narrower hatch spacing, showed very little porosity. In general, the porosity content and pore cross sectional area in this experiment was much smaller in comparison to the SS components which is another indication that the parameter settings for the SS components were not optimized for porosity content observed in the various scan strategies.

Using the data obtained from the two-dimensional CT slices, approximate fatigue life predictions were calculated for each component, and the components were fatigued until catastrophic failure occurred. Actual fatigue lives and life predictions were then compared (Figure 4.6). It was observed that the life was severely underpredicted for each compo-

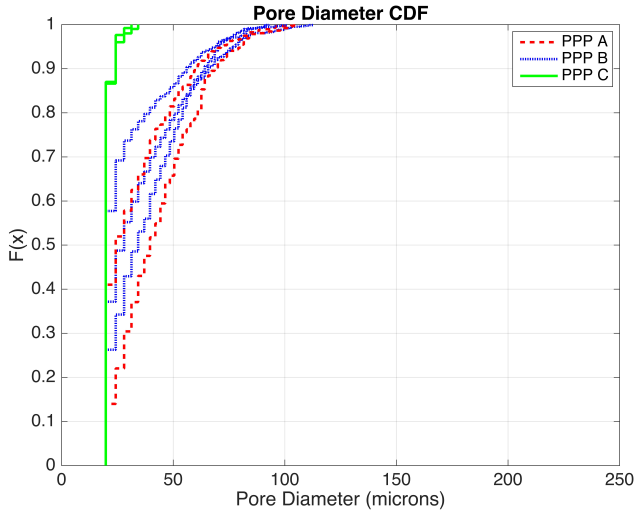

Figure 4.5: Cumulative Distribution Function of pore diameter for the PPP components

nent. This discrepancy indicates that the crack growth model developed by Konecna is not representative of the PPP experiment material. Therefore, AM processing pedigree plays a significant role in crack growth behavior. The components for both the scan strategy and PPP studies were post-processed in the same way, but their original build processing conditions were very different. The SS components were made with almost double the powder layer thickness of the PPP components. This was partially counteracted by increasing the beam power, speed, and hatch spacing for the SS components. Therefore, in order to understand the performance of an AM component it is imperative to also understand the influence

of PPPs and scan strategy on microstructure texture and phase development which dictate crack growth behavior. This must be pursued in future work.

Further observation indicated that the PPP component fatigue lives were similar to the lives of wrought components subjected to the same loading conditions [2]. Therefore, the crack growth model for a half inch die forged alloy 718 plate subjected to a stress ratio $R = 0.05$ was obtained such that the crack growth constants $(C, n) = (3.0 * 10^{-13}, 3.89)$. Implementing this new model significantly reduced the error in the life prediction, and pushed each of the predictions to within the 2x scatter band as shown in Figure 4.6.

It is also seen in Figure 4.6 that PPP-C components significantly outperformed PPP-A

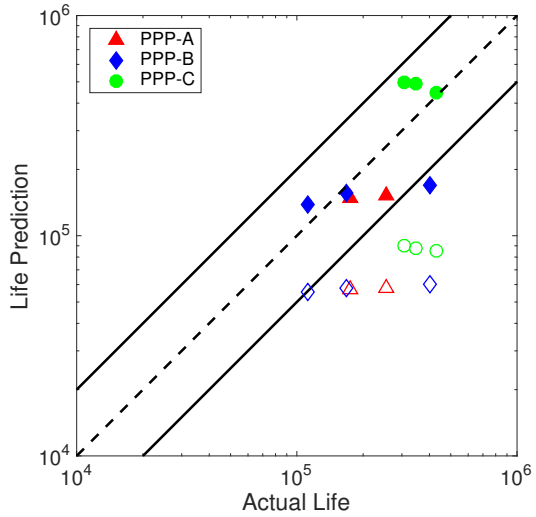

Figure 4.6: Life prediction comparison to actual life for PPP components assuming wrought (solid) and previously published AM (empty) crack growth behavior.

and PPP-B components as was hypothesized based on the component porosity size distributions. Additionally, PPP-A and PPP-B appear to perform similarly in regards to the fatigue life. This is consistent with the porosity data shown in Figure 4.5 where the CDFs of porosity diameter for PPP-A and PPP-B components are intermingled with each other. Life prediction using porosity data from AM components manufactured via different scan strategies and PPP settings is therefore feasible using two-dimensional data obtained from CT measurements, but pre-existing knowledge of the materials' crack growth behavior is

required to obtain accurate predictions.

4.3.3 Fractography

The investigation above supports the hypothesis that stress intensities induced by pores of various sizes heavily dictate the fatigue life of a component, and the maximum stress intensity calculated from non-destructive measurements is useful in predicting the fatigue life of additive components following a pre-determined crack growth behavior. To verify the results above, a post-mortem examination of each component's fracture surface was performed.

Initial observations indicated diverse failure mechanisms among the entire population of components including surface pores, pore lines, and brittle inclusions. Some components did not appear to fail as a result of any of these mechanisms. A summary of the failure mechanisms for each component is provided in Table 4.3, and images of representative crack initiation locations are shown in Figure 4.7.

For the five SS components, only two conclusive failure mechanisms were identified. One SS-B component exhibited a large spherical pore at the crack initiation location. Further examination of the entire fracture surface revealed multiple large pores in straight lines which may correspond to a strip intersection location. These anomalies were not observed in the other SS-B component; however a larger number of observations must be made to draw any conclusions as to why the pore lines were present in the component. The second conclusive failure mechanism was a small pore at the surface of SS-C. The elongated pore was very small compared to the pores mentioned before, but the life exhibited by SS-C was nearly the same as SS-B. This could indicate that the pore was partially obscured from view on the fracture surface or that local crack growth behavior was different from the crack growth model. Crack growth experiments will reveal location dependence of crack growth behavior and will shed light on the true crack growth behavior of these components.

Table 4.3: Summary of fractographic observations and measurements

PPP Setting	Fatigue Life	Failure Mechanism	Predicted Defect Size	Observed Defect Size	Post-Failure Life Prediction
SS-A	69,559	-	70.00	-	-
	79,904	Inclusion	59.39	41.24	44,119
SS-B	29,974	-	230.04	-	-
	39,079	Pore	119.62	53.52	40,340
SS-C	37,167	Pore	95.98	19.72	55,650
PPP-A	254,090	Pore	102.88	43.75	127,550
	175,724	Pore	105.7	39.82	139,700
PPP-B	167,154	Pore	100.96	36.63	151,420
	404,301	-	92.87	-	-
	111,791	Pore	112.87	33.49	165,070
PPP-C	346,635	Other	31.31	-	-
	308,118	Other	-	-	-
	430,679	Other	34.29	-	-

For the PPP parts, it was observed that the lowest performing components failed at easily observable pores, but the higher performing components were more ambiguous as to their failure mechanisms. Figure 4.7 shows six fractographs each exhibiting a different failure mechanism. One PPP-A component clearly showcases a pore at the initiation location, but

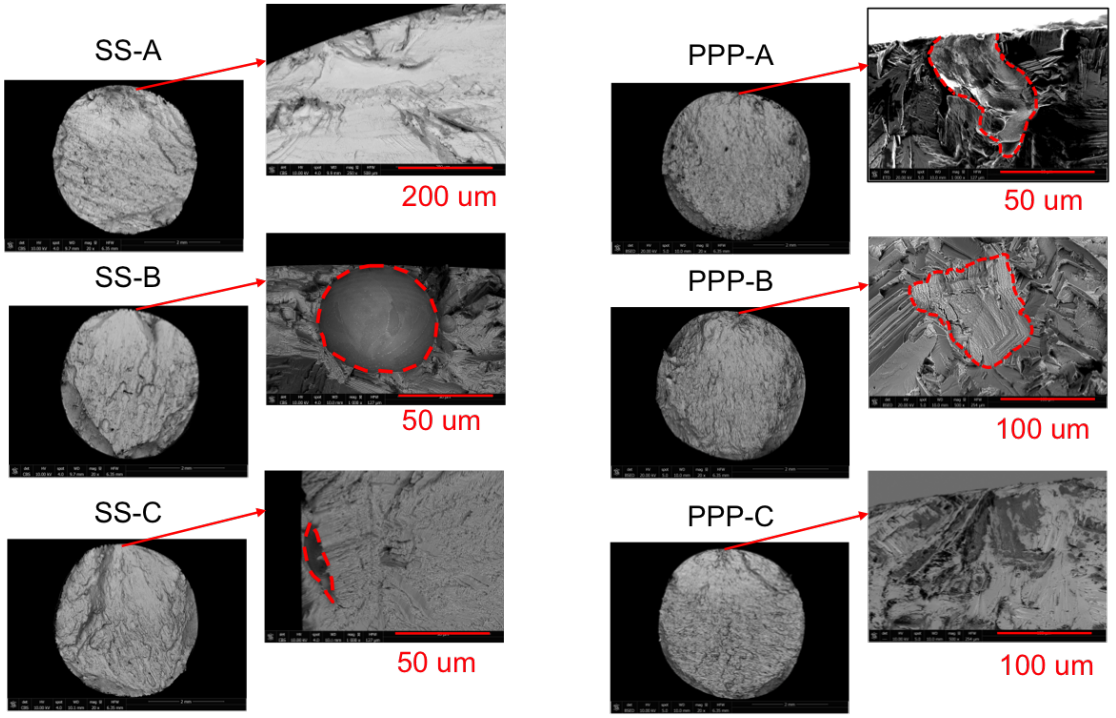

Figure 4.7: Fractographs obtained from the crack initiation locations for both experiments

the images shown for both PPP-B and PPP-C show ambiguous failure mechanisms which may be twinning-induced failures. Both experiments showed that the pores observed in the

fractographs were typically smaller than those observed in the CT measurements. When the crack growth life prediction approach described above was applied based on the observed fracture surface porosity, the life predictions were different from the CT-based predictions, but they were still within the 2x scatter band (see Figure 4.8). The difference between CT-based predictions and fractography-based predictions may have been caused by local crack growth behavior that caused deviations from the model for each scan strategy or PPP setting. This is supported by the observation that components within PPP-A and within PPP-B seemed to exhibit similar failure pore sizes and life predictions. Therefore, initial observations support the claim that components manufactured and processed under the same pedigree will perform at similar levels because they contain similar porosity content. Furthermore, components manufactured and processed under different pedigrees may not perform at the same level because an increase or decrease in porosity, not to mention other microstructural features, will differ, therefore varying the crack growth behavior of the components.

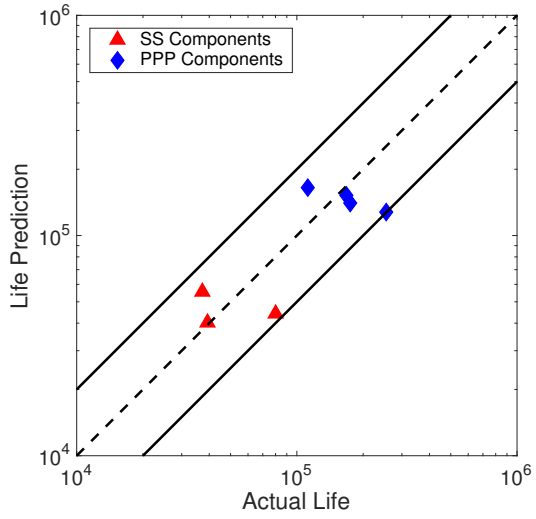

Figure 4.8: Fractograph-based life prediction comparisons to actual life for components which failed due to observable defects. Crack growth constants as described above were used for each experiment.

4.3.4 Response Surface Based Life Predictions

The mean pore diameter model developed in Chapter 3 may then be leveraged and applied to the fatigue life prediction framework demonstrated here. Life predictions for a broad region of process space may then be obtained and compared against experimental data. The specimen geometry used above is assumed to undergo a cyclic stress range of 810 MPa (118 ksi). The pore diameter data collected in Chapter 3 was revisited, and the average standard deviation for every measured pore distribution was calculated and assumed to represent the global pore diameter standard deviation (s_g) across the entire process space. This value was calculated to be 21.2232 μm.

Using the calculated average pore diameter for each component (Eq. 3.13) and the global standard deviation, a three-parameter lognormal distribution ($logn[\mu, \sigma_{std}, d_{thresh}]$) was approximated such that

$$\mu = \log\left(\frac{f_{Diameter}^2}{\sqrt{s_g^2 + f_{Diameter}^2}}\right) - d_{thresh} \tag{4.1}$$

and

$$\sigma_{std} = \sqrt{\log\left(\frac{s_g^2}{f_{Diameter}^2} + 1\right)} \tag{4.2}$$

where μ and σ_{std} are the mean and standard deviation of the corresponding normal distribution, and d_{thresh} is the threshold value representing the smallest pore considered in the investigation (14 μm). The lognormal CDF was used to define an approximate "worst-case" pore for each component such that its diameter is in the 90^{th} percentile of the entire pore population. This value was assumed to be relatively conservative, but it may be modified to tailor the conservativeness of the life prediction exercise if the user so desires. Eq. 3.13 was then applied over the range of process space, and the life was calculated via Eq. 2.15 using the defined failure pore, and the wrought crack growth properties. A subset fatigue life response surface for the low power, low layer thickness setting is portrayed in

Figure 4.9. The response surface indicates an increase in fatigue life for areas of high density, and small pore diameter, and a significant drop in fatigue life for areas of both high and low energy density corresponding to increased pore size and decreased density.

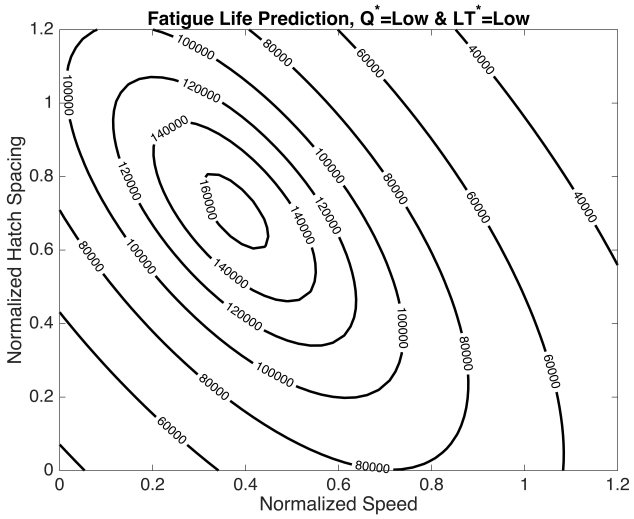

Figure 4.9: Fatigue prediction map based on the mean pore diameter model and a global standard deviation constant for low power and low layer thickness settings

To validate the utility of this response surface method for life prediction of additive components, predictions from the response surface were compared to the PPP components described above and are exhibited in Figure 4.10 with a 2x scatter band. Figure 4.10 shows that four of the components fall within the 2x scatter band which indicates an exceptional life prediction. Four of the specimens fall outside and to the right of the scatter band which indicates that the model under-predicted the life of the components. This result is still acceptable because the prediction is conservative and will not result in premature failure.

There are several mechanisms that may influence the accuracy and uncertainty of the life prediction response surface. Three of them are presented below:

1. Average pore diameter is a random variable which may change slightly among components manufactured using the same PPP settings. This variation is not accounted for in the above method.

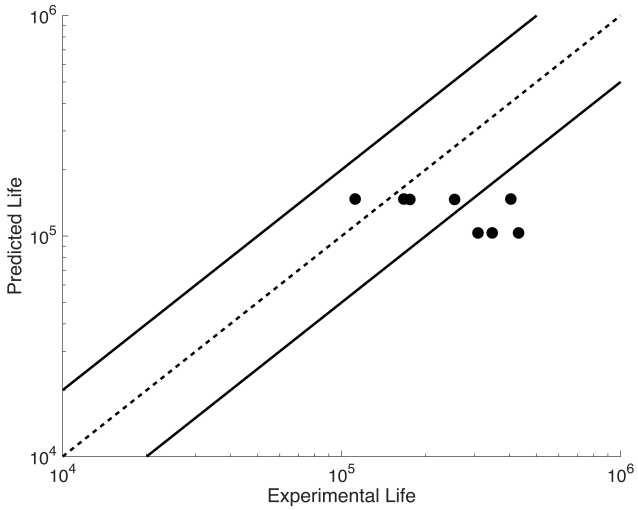

Figure 4.10: Comparison of calculated growth life predictions to experimental data for AM fatigue components

2. The standard deviation of pore diameter may change functionally or stochastically from specimen to specimen and among PPP settings. The global standard deviation is a simplification that may need to be revisited for appropriate statistical analysis.

3. The 90^{th} percentile pore diameter for each PPP combination was assumed to be the worst case scenario, but it is probable that the failure-inducing defect at a given PPP combination will be either larger or smaller than this standard pore diameter. This variation will change the result and introduces uncertainty in the prediction.

Further analysis and application of Monte Carlo-based methods may address these mechanisms, but the simplicity of the above method facilitates quick and sufficiently accurate life predictions for axial fatigue of additive components.

4.4 Conclusion

The PSPP relationship for AM IN718 has been explored by characterizing the development of porosity under different processing conditions and from two different machines. The porosity within each component was measured and analyzed, and the influence of the

porosity on the fatigue life of the components was measured which lead to several new insights.

First, as was mentioned in Chapter 3, scan strategies and PPPs are important factors that dictate the porosity content within AM components. Second, the porosity that is induced by varying scan strategy and PPPs dictates the fatigue life of the machined AM component. Third, non-destructive observation of component porosity can be leveraged to accurately predict fatigue life. It has also been shown that predictions based on CT measurements are similar to predictions based on fracture surface porosity measurements; however, accurate life prediction can only be obtained, if the crack growth data of each material system is known. Finally, the regression model for pore diameter developed in Chapter 3 was applied to the developed life prediction framework, and a new life prediction map for additive manufactured components was presented. This map was compared to experimental fatigue life data, and it was seen that predictions were accurate and conservative for AM components. Mechanisms influencing the accuracy and uncertainty of the life prediction model were also discussed.

This investigation is a "first of its kind" look at the comprehensive relationship between the processing, structure, properties, and performance of AM components with respect to porosity. The results presented here provide significant insight into the behavior of AM materials and represent a leap in understanding of AM processing and material performance that can be used in the design of future components. With this new understanding, AM processes can continue to be optimized for reduction of porosity and improved performance, and design constraints can be developed to account for the intrinsic detriment imposed by internal porosity.

Alloy 718 Fatigue Baseline

5.1 Introduction

In light of the fact that PPPs play a significant role in defect formation, it is important to illustrate how pores influence the fatigue failure of porous, AM components compared to "defect-free", wrought material. The insight provided by this investigation bridges the gap between the structure and the properties and performance of the material, and this baseline investigation will greatly inform future investigations of behavior of AM material in the presence of defects and will shed light on defect tolerant design methodology development.

5.2 Materials and Methodology

To perform a baseline fatigue test of AM alloy 718 compared with wrought material, two AM builds were performed on a Concept Laser™ M2 Cusing LPBF machine. Thirty-six 12.25 mm (0.5") cylinders were manufactured to height of 95.25 mm (3.75") for each build. The process parameters are summarized in Table 5.1. The components were stress-relieved

Table 5.1: Process parameters for vertical fatigue bar builds

	Power	**Speed**	**Hatch Spacing**	**Layer Thickness**
Vertical A	370 W	700 mm/s	130 μm	40 μm
Vertical B	370 W	700 mm/s	130 μm	80 μm

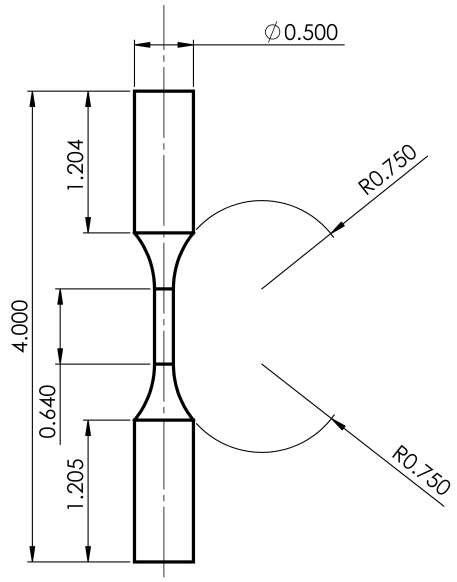

Figure 5.1: Fatigue Specimen Dimensions

on the base plate as described in [19] and heat treated off the plate as described in section 2.2.2. ASTM standard specimens [90] were manufactured from the AM cylinders to the dimensions shown in Figure 5.1. Wrought alloy 718 rods of the same diameter were aged in the same manner as the AM components (see section 2.2.2), and they were machined to the same ASTM standard dimensions.

Fatigue testing was performed on an MTS 312.12 servohydraulic loadframe with a 100 kN (22 kip) load cell. Loading was performed axially under load control with a load ratio R equal to 0.1. Each test was performed at a single stress level until failure or until runout at 10^7 cycles. In the event of a run out, the cyclic stress on the specimen was increased, and the fatigue test was continued at this stress until failure or run out. This "step-wise" procedure was continued until catastrophic failure of the component. The fatigue stress of a component having undergone a step test was calculated using the following equation [91]:

$$\sigma_f = \sigma_{i-1} + \Delta\sigma\left(\frac{N_i}{10^7}\right) \tag{5.1}$$

where σ_f is the fatigue strength at 10^7 cycles, σ_{i-1} is the next to last stress step, $\Delta\sigma$ is the

stress step size, and N_i is the number of cycles to failure on the last stress step.

Post-failure, the fracture surfaces of each specimen were removed with a high speed saw and cleaned with isopropyl alcohol. The failure pores were observed using the Phenom XL desktop scanning electron microscope and the projected area of each pore was measured. Unfortunately, several specimens from the Vertical A batch were improperly labeled, so failure pore measurements for these specimens were mixed up. Another set of tests from the same data set were performed, and the fracture surfaces were carefully labeled. Therefore, for S-N data every specimen is represented, but for pore measurement data, only the specimens for which the fracture surfaces were properly labeled are represented.

5.3 Results and Discussion

The collected S-N data is displayed in Figure 5.2 for Vertical A (blue triangles), Vertical B (red circles) and wrought (black squares) data sets. The blue, filled triangles represent data from Vertical A for which correct porosity data exists, and the blue, empty triangles represent data for which the porosity data was scrambled.

It can be observed that in the AM data there is significant scatter compared to the wrought material. First glance indicates that neither Vertical A nor B exhibits superior performance compared to the other, but both material systems exhibit a broad range of performance compared to the wrought. Several components exhibit life similar to the wrought material, but a majority of the AM components exhibit significant life debits which sometimes reach to up to a 99.9% difference in fatigue life between AM and wrought material in HCF. In fact, the upper limit of the AM S-N data closely follows the wrought, and the rest of the data falls below this curve. This observation indicates that the AM bulk material behaves in a similar manner to wrought AM material, but some material structural characteristic (i.e. defect) in the AM material initiates a crack sooner than in the wrought

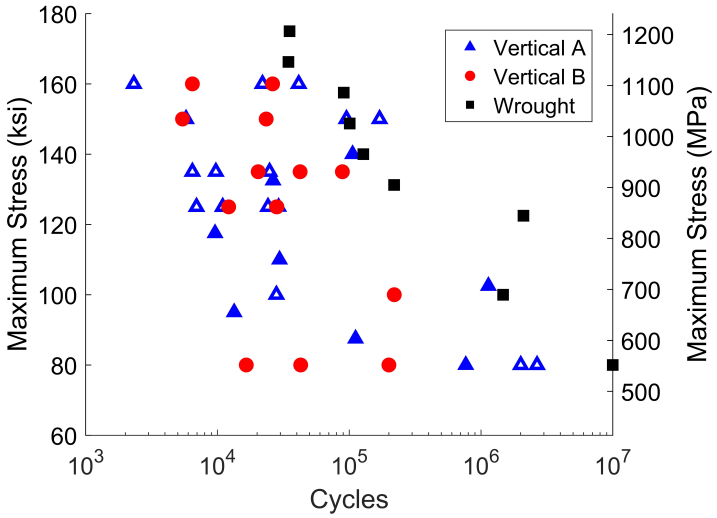

Figure 5.2: S-N data for Vertical A (blue triangles), Vertical B (red circles) and wrought (black squares) data sets

material. Therefore, it is necessary to observe the defect sizes on the fracture surfaces to determine how the defects interact with the applied stress to initiate and propagate a crack.

5.3.1 Fractography

Inital observations from fractography of the tested specimens show two obvious failure mechanisms: LOF and twinning defects. These types of defects and other observations are portrayed in Figure 5.3. LOF defects in these specimen lots are easily observable, and exhibit two characteristics of note. First, the defects causing failure were often very large sometimes on the order of five hundred microns in diameter (see Figure 5.3a and 5.3b). Second, the pores causing failure were most likely caused by the layer thickness being too large because the pores are very flat and laser track marks and unfused powder are observed within these pores (see Figure 5.3b). For HCF and LCF failures alike, one feature that was observed multiple times was multi-level fracture surfaces which were caused by defects located at multiple locations along the length of the specimen (see Figure 5.3a) . Cracks initiated at these defects, and the separate cracks coalesced during final failure resulting in

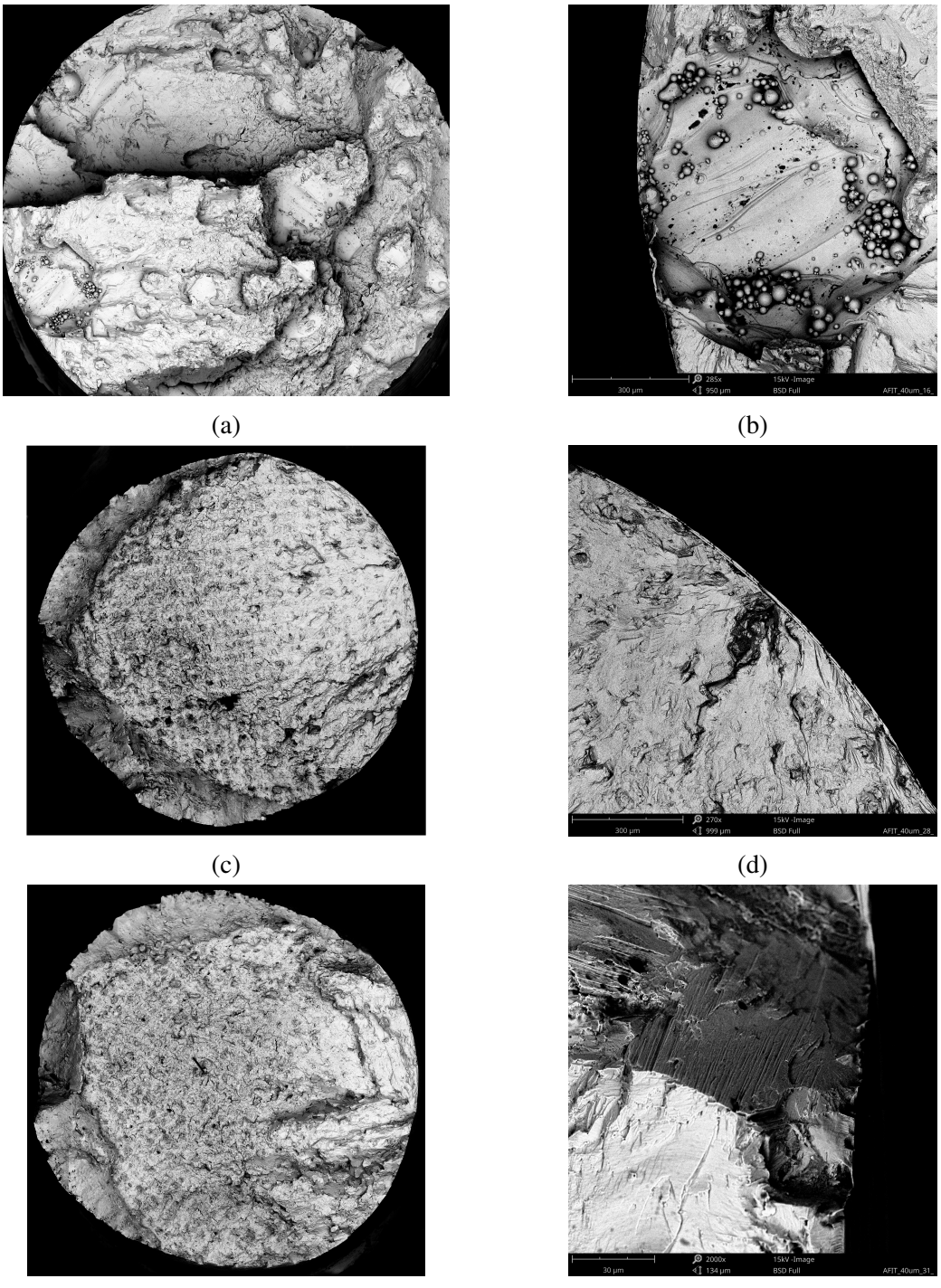

Figure 5.3: Representative fracture surfaces exhibiting features common to many of the Vertical specimens. Each total fracture surface (a,c,e) is matched with its corresponding failure location (b,d,f). For a,c,and e, the specimen diameter is 4.064 mm (0.16 inches).

stepped fracture surfaces.

Five of the specimens tested did not exhibit pores at the failure locations (see Figures 5.3c-5.3f for examples). This indicates that even in the presence of pores in a material, some microstructure-based defects (in this case twinning defects) can dominate the failure of a component. Therefore, appropriate microstructural analysis is most likely necessary to fully predict fatigue life of AM components. Another common occurence with components experiencing HCF was a lattice-like pattern along the fracture surface which seems to follow the scan strategy for the specimens (See Figures 5.3c and 5.3e). This pattern exists probably because the crack followed the microstructure within the melt pool tracks leaving behind the pattern observable via microscopy. Additionally, regions where the melt region did not overlap sufficiently may have resulted in patterns of porosity throughout the melted material. Further investigation must be performed to assess these observations.

5.3.2 Pore-Stress Interactions

Because almost every specimen failed due to one or multiple pores, it is necessary to analyze the influence of both pore size and applied stress on the fatigue life. One way to visualize this multi-dimensional problem is to modify Figure 5.2 so that the color of each data point indicates the size of the pore which caused the failure. This new visualization is shown in Figure 5.4. The first observation that can be made is that the specimens that performed most comparably to the wrought material exhibited extremely small porosity, and the specimens that performed poorly, exhibited relatively large porosity. Secondly, for a given data set at a single stress, scatter in the data is explained well in light of the failure pore size. For Vertical B, at a given stress state for a particular data set, the life of the part increases as the failure pore size decreases. This trend is easily seen due to the number of replicate experiments performed at each stress state. A similar trend is more difficult to observe in Vertical A because stress level replicates are not available. It can be assumed,

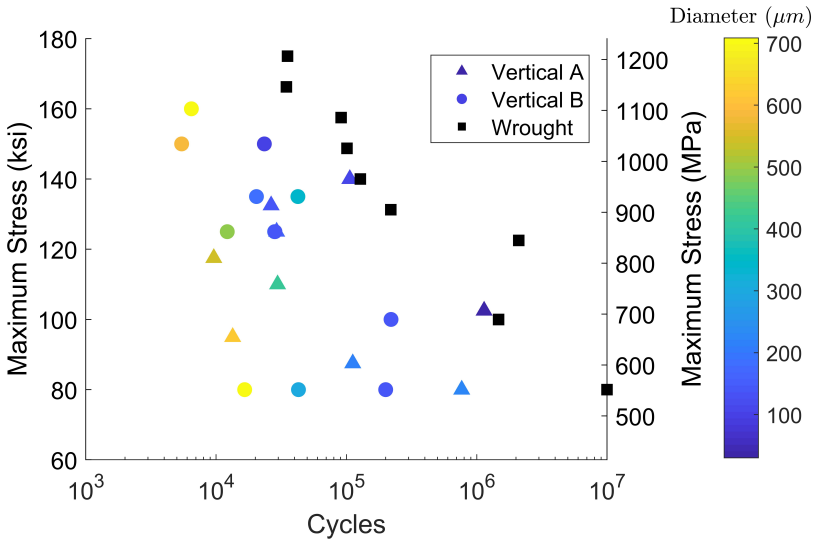

Figure 5.4: S-N data for Vertical A (triangles), Vertical B (circles) and wrought (black squares) data sets where the data color represents the pore size in microns

however, that a similar trend may apply to Vertical A.

Since pore size and stress level obviously relate to final fatigue failure, it is intuitive that combining pore size and stress level into a single term would effectively collapse the scatter in the S-N data to a single curve. A common term that describes the localized stress around a crack of a certain size is the SIF which for small pores is given by Eqs. 2.9 and 2.10 depending on where the pore is located in the specimen. Most failure pores for this range of stresses occur at the surface of the specimen, so Eq. 2.10 most likely represents a majority of the failure pores observed in this experiment. Therefore, the stress intensity of the failure pore for each specimen was calculated such that $\Delta\sigma = 0.9\sigma_{max}$, and the resulting dK-N plot was constructed (see Figure 5.5). The power function regression curve and 95% confidence prediction bounds were overlaid on the data. In general, the scatter in the data is completely reduced to a single curve in this form. This indicates that the stress intensity of the failure pore is highly indicative of the life of the part. There is one potential outlier that appears in the upper stress intensity region and falls slightly outside of the 95% prediction bounds, but it does not appear to be far enough from the rest of the data to warrant any concern.

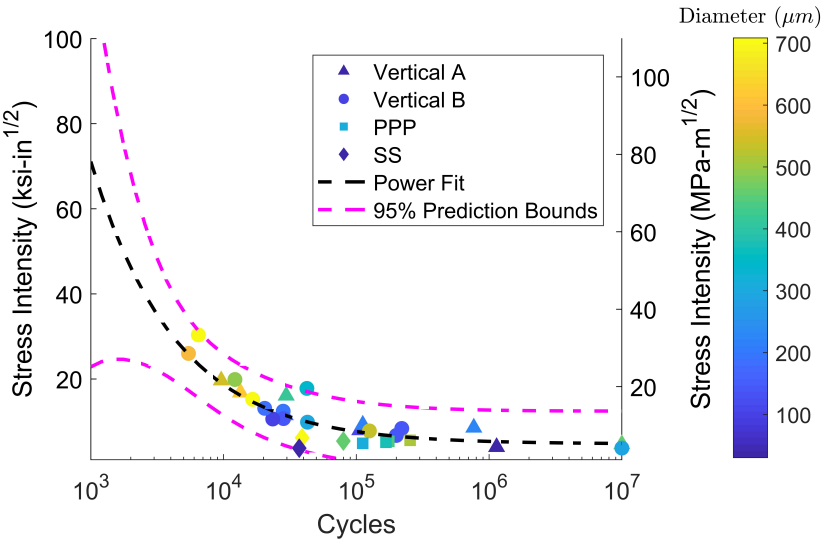

Figure 5.5: dK-N data for Vertical A (triangles) and Vertical B (circles) data sets where the data color represents the pore size in microns

Close examination of the data and regression curve shows that the dK-N data follows a two term power trend of the form $\Delta K = A(N)^b + C$ where A, b, and C are the regression constants and N is the life of the part. For this particular material and data-set, ΔK $(MPa - \sqrt{m})$ is given by

$$\Delta K = (7.910 * 10^3)N^{-0.6784} + 5.192 \tag{5.2}$$

In log-log space, the data trend begins with a very steep, negative slope, and as the number of cycles increases, the trend flattens to an almost horizontal line similar to the fatigue limit observed in many alloys. The horizontal asymptote that this curve approaches is given by the regression constant C and describes the cyclic stress intensity for which a component will exhibit infinite life. Another interpretation is that the C term represents the threshold SIF for the material, and every point along the curve represents the initial stress intensity due to a pore which will result in a specific fatigue life. These quantities may be referred to as effective threshold stress intensities for finite life ($\Delta K_{th,N_i}$) where the Ni subscript represents the number of cycles to failure for that particular ΔK value.

Because $\Delta K_{th,N_i}$ is a function of fatigue life, and fatigue life due to a pore approaches wrought properties as the size of the initiating pore decreases, a Kitagawa-based model can be developed to predict fatigue life based on pore diameter and applied stress. First, $\Delta K_{th,N_i}$ for a specified fatigue life is determined from Eq. 5.2, and the average fatigue stress for that life is determined from S-N data for wrought material. The wrought material data collected for Figure 2.4 is represented by the equation

$$\sigma_{max} = (5.392 * 10^3) N^{-0.1606} + 190.847 \tag{5.3}$$

for lives up to 10^7 cycles where σ_{max} is the maximum stress (MPa) in the cycle and N is the total number of cycles to failure.

These two parameters can be applied to Beretta's modified El-Haddad model such that

$$\Delta\sigma_{w,N_i} = (1-R)\sigma_{max}\sqrt{\frac{\sqrt{A_{0,N_i}}}{\sqrt{A}+\sqrt{A_{0,N_i}}}} \tag{5.4}$$

where $\sqrt{A_{0,N_i}}$ is

$$\sqrt{A_{0,N_i}} = \left(\frac{\Delta K_{th,N_i}}{(1-R)\sigma_{max,N_i}}\right)^2 \frac{1}{\pi} \tag{5.5}$$

and $\Delta K_{th,N_i}$ and σ_{max,N_i} refer to Eqs. 5.2 and 5.3 respectively evaluated at some fatigue life (N_i). Therefore, the new finite-life El-Haddad model becomes a function of cyclic stress, defect size, and cycles to failure. The resulting function is plotted in Figure 5.6 as a contour plot. This plot shows that increasing life requires a decrease in cyclic stress, but the decrease is sensitive to how large of a defect is in the component. For small defects, the spread is relatively even, but as the defect size gets larger, the sensitivity of stress range to fatigue life decreases with increasing fatigue life. Qualitative comparison of the experimental data to the new modified El-Haddad model shows extremely good correlation. While there is some overlap of fatigue lives in the experimental data with respect to $\sqrt{A}$

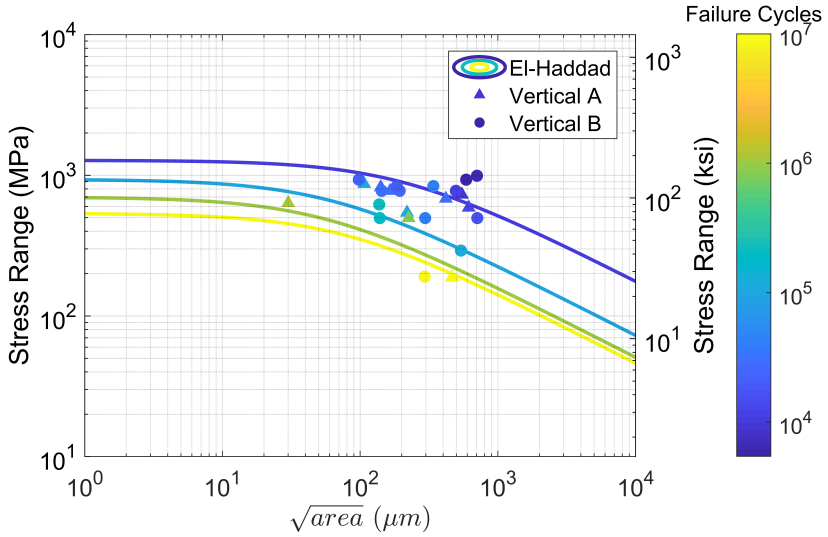

Figure 5.6: Modified Kitagawa-Takahashi diagram for finite life prediction and Vertical A and Vertical B data overlaid

Table 5.2: Critical pore size ($\sqrt{A_{0,N_i}}$) for several fatigue life decades

N_i	$\sqrt{A_{0,N_i}}$ (μm)
10^4	193.8
10^5	60.7
10^6	53.0
10^7	74.5

and cyclic stress range, it is clearly seen that the colors of the experimental data closely resemble the colors of the finite life El-Haddad model contours.

From this model, the critical pore size ($\sqrt{A_{0,N_i}}$) at some fatigue life (N_i) can also be obtained from Eq. 5.5. A tabulated list of some key critical pore sizes are compiled in Table 5.2.

It is odd that the critical pore diameter decreases until 10^7 cycles at which point it increases by about 50%. The reason this occurs can be found from closer examination of Eqs. 5.2 and 5.3. At 10^7 cycles, $\Delta K_{th,N_i}$ exhibits an almost horizontal slope indicating a stress-intensity limit. For the data obtained, $\Delta\sigma_{max}$ still has a steep, negative slope which indicates that the fatigue limit for this material at load ratio of $R = 0.1$ is at a lower stress. Therefore, while the second leg of the Kitagawa diagram corresponding to the stress

intensity factor converges to a single slope as number of cycles increases, the fatigue limit stress represented by the horizontal first leg of the Kitagawa diagram does not converge. Therefore, the critical length (the intersection of the first leg and the second leg of the diagram) will increase as the number of cycles increases beyond 10^7 cycles.

While this phenomenon is explained by the regression models, intuition is not satisfied. Alloy 718 will approach a fatigue limit as the number of cycles increases. This has been seen in the literature and is exhibited clearly in Figure 2.4 for the load ratio $R = -1$. It is probable that more data at lower stress levels will exhibit longer fatigue lives and reveal the location of the fatigue limit of the material. When this is revealed, Eq. 5.3 can be updated, and the critical value should continually decrease and converge to an "infinite-life" critical value.

5.3.3 Comparison to Prior Results

The conclusions from Chapter 4 indicated that while porosity plays a large role in determining the life of a component under stress, the crack growth behavior of the material determines how quickly the failure pore grows to a critical length. Therefore, specimens with significantly different crack growth behavior will exhibit significantly different fatigue lives. Based on the results from this chapter's investigation, though the additive material appeared to exhibit fatigue behavior equivalent to wrought material with a pre-existing flaw. Therefore, it is necessary to compare the performance of the components in Chapter 4 with the performance in this chapter.

Recreating Figure 5.2 with SS and PPP component performance overlaid on the plot (see Figure 5.7) shows that both SS and PPP fall within the range of fatigue lives observed in the current investigation. Figure 5.7 shows that the PPP components exhibit life similar to that of wrought material while the SS components exhibit significantly reduced life. The scatter exhibited by the horizontal specimens is much less than the scatter exhibited by

Figure 5.7: Combined S-N data from PPP, SS, and Vertical data sets.

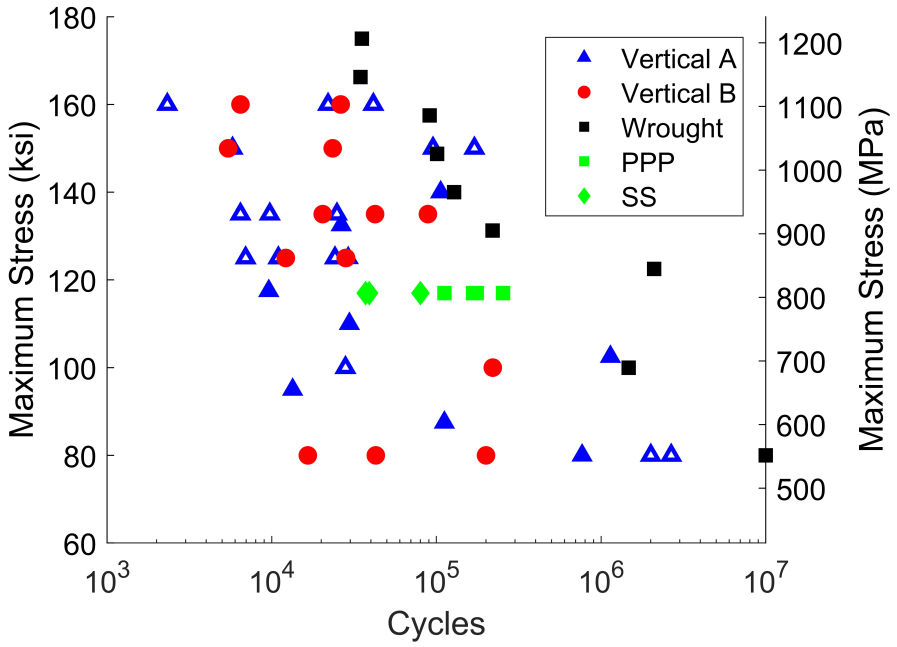

the vertical specimens. This indicates that the porosity distributions for the vertical specimens are much wider than for the horizontal specimens which increases the variability of the failure pore size. The difference between the lives of the SS components and the PPP components (factor of 10) is relatively small compared to the scatter among the vertical specimen lives (factor of 100). Since it was seen that the vertical specimens exhibit properties similar to wrought material with an equivalent failure defect, it is certain that some phenomenon not accounted for in the assumptions presented in Chapter 4 is causing a disparity in the fatigue lives. First, a comparison of initial stress intensities should be examined to determine whether one set of specimens is getting a ”head-start” over the other set.

Not every specimen exhibited a pore on the fractographic surface, so information from the fourth column of Table 4.3 was utilized to approximate the failure defect size. Based on those measurements, the initial SIF was calculated from Eq. 2.10 which is the worst case SIF for a surface pore. These values are tabulated in Table 5.3. By overlaying the data

Table 5.3: Summary of fractographic observations, measurements, and corresponding SIFs

PPP Setting	Fatigue Life	Predicted Defect Size	ΔK $(ksi\sqrt{in})$	ΔK $(MPa\sqrt{m})$
SS-A	69,559	70.00	7.08	7.78
	79,904	59.39	6.52	7.16
SS-B	29,974	230.04	12.83	14.10
	39,079	119.62	9.25	10.16
SS-C	37,167	95.98	8.29	9.11
PPP-A	254,090	102.88	8.58	9.43
	175,724	105.7	8.7	9.55
PPP-B	167,154	100.96	8.5	9.34
	404,301	92.87	8.15	8.96
	111,791	112.87	8.99	9.87
PPP-C	346,635	31.31	4.73	05.2
	308,118	-	-	-
	430,679	34.29	4.95	5.44

represented in Table 5.3 on Figure 5.5 (see Figure 5.8), it can be observed that the horizontal component data matches almost exactly with the vertical data. This evidence indicates that the horizontal components do indeed exhibit the same material behavior in the presence of defects to wrought material and the vertical specimens. A question that must be answered then becomes, why did the PPP specimens exhibit such different behavior from the SS specimens? A partial answer to this question is quite possibly a simple explanation which challenges a major assumption made in Chapter 4. The primary assumption is that crack growth in these porous specimens follows the Paris power law. Examination of Figure 5.8 shows that both PPP and SS SIF's lie near the horizontal portion of the curve which indicates that the initial SIF's are near the threshold SIF for the material. Therefore, small crack growth must be accounted for in the growth life prediction. A consequence of neglecting small crack effects is that the initial crack growth rate for a flawed component is significantly increased at smaller SIFs. Indeed, including small crack effects will significantly increase the number of cycles necessary to grow a crack from a near-threshold small crack to a failure sized crack. Additionally, larger pores, as observed in the SS study will initiate in or near the Paris regime and will reach failure lengths significantly quicker than

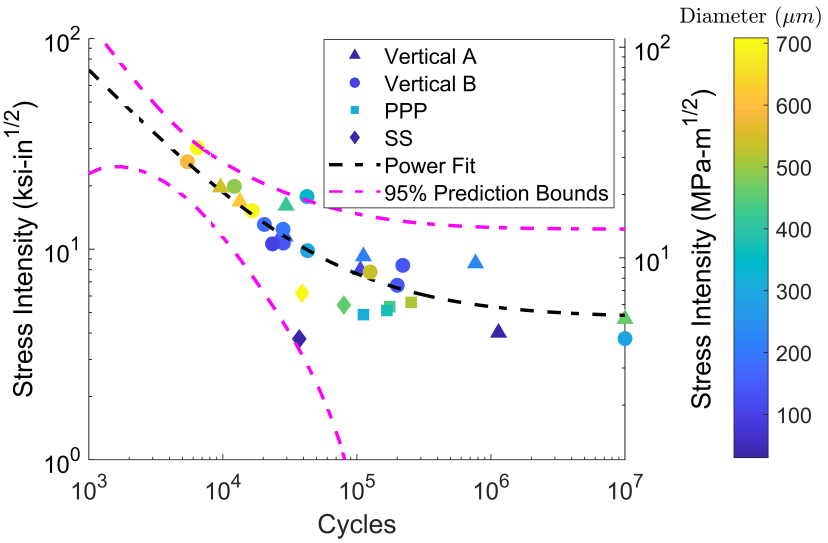

Figure 5.8: dK-N data for Vertical A (triangles), Vertical B (circles), SS (squares), and PPP (diamonds) data sets where the data color represents the pore size in microns. Note the Vertical A and B data sets represent pore data from the fracture surface, and SS and PPP data sets represent pores from CT inspection.

those starting in the near threshold region.

In addition to near-threshold effects on small crack growth, crack path tortuosity and roughness-induced crack closure effects must also be taken into account. Since dislocations and small cracks traverse through grains in preferential directions dependent on grain orientation, finer grained materials may experience significantly higher fatigue lives because the crack encounters significantly more grain boundaries requiring it to change directions more frequently than coarser grained materials. The frequency that a crack must change directions significantly impacts the roughness of the fracture surface. Several authors have found that fracture surface roughness increases with increasing grain size [92–97]. Roughness-induced crack closure effects occurs when the roughness of the fracture surface described above prevents the two crack faces from closing completely. Therefore, the material does not return to a "no-load" state, and an effective decrease in ΔK occurs which reduces the rate of crack growth. Therefore, three different mechanisms could explain the difference in number of cycles to failure between the three data sets: near threshold effects, crack path tortuosity, and roughness-induced closure effects. Grain size and surface roughness, can be

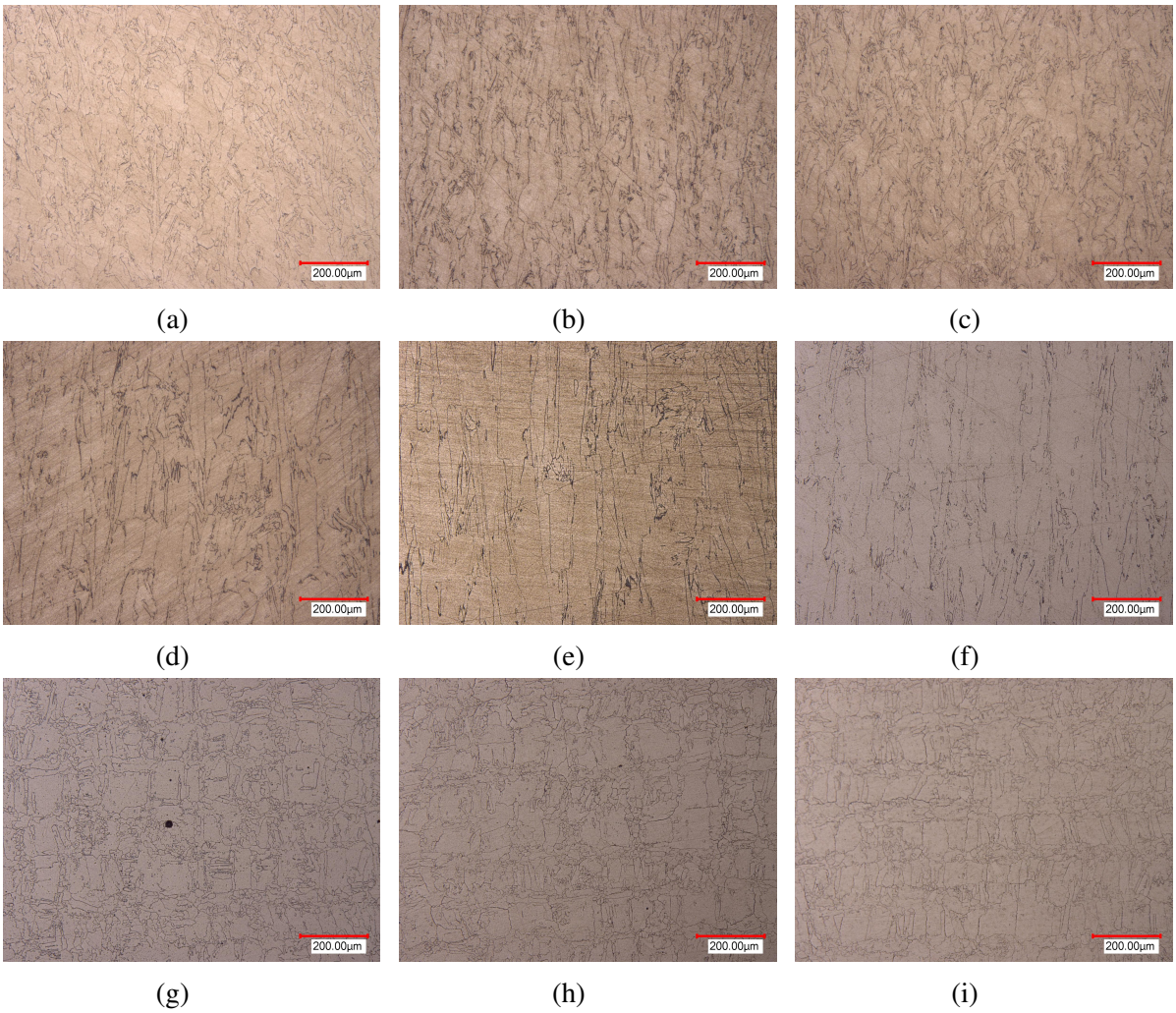

Figure 5.9: Representative microstructure from the a-c) PPP, d-f) SS, g-i) Vertical data sets. For images a-f, the build direction is vertical on the page, and the loading direction is out of the page. For images g-i, both the build direction and the loading direction are out of the page.

examined closer in the current investigation.

Images of the microstructure for each processing state were obtained from the tested material. A portion of the test section was removed from the specimen after failure, and it was mounted in graphite-based resin. Each specimen was polished to 1 μm and subsequently swabbed with Waterless Kalling's No. 2 etchant [98] for approximately 40 seconds to reveal the microstructure. Figure 5.9 shows that each data set exhibits different microstructure. The PPP specimens exhibit fine, columnar microstructure; the SS specimens

exhibit coarse, columnar microstructure; and the vertical specimens exhibit fine, equiaxed, and structured microstructure. The differences in microstructure can be explained by the processing. The PPP specimens experience much lower powers and higher speeds compared to the SS specimens. In general, lower energy density produces smaller grains. Additionally, power is directly related to the thermal gradient of the microstructure [15], and the thermal gradient controls the morphology of the microstructure [99] and the direction that the grains grow. The SS specimens exhibit significantly elongated grains compared to the PPP specimens which agrees with the elevated power experienced by the SS components. The fine, equiaxed microstructure observed in the vertical specimens occurs due to the direction of the grain growth. In the PPP and SS specimens, the build direction is vertical on the page while in the vertical specimens, the build direction is directly out of the page. The thickness of the grains for the vertical specimens is approximately the same size as the SS specimens due to similar processing, but the morphology in this plane is significantly different because of the difference in orientation of the specimens on the build plate. Therefore, a crack that grows in the plane of the page, as demonstrated in the fatigue tests, will experience significantly different crack growth behavior for each set of specimens. This behavior is determined by the size and morphology of the microstructure which as discussed above is directly related to the thermal processing of the material. Based on the microstructural observations and qualitative grain size analysis, it was expected that the SS specimens would exhibit the largest surface roughness followed by the PPP and vertical specimens. Table 5.4 shows, however, that SS fracture surfaces exhibited the smallest surface roughnesses and that PPP and vertical specimen fracture surfaces exhibited much larger surface roughness values. These observations directly contradict observations found in the literature which prevents satisfactory conclusions from being made with respect to the current experimental data. What can be concluded from these observations is that significantly different microstructure is exhibited among the three different data sets. It is well known that microstructure size and morphology dictates crack growth behavior due to the

Table 5.4: Average surface roughness measurements obtained from multiple representative fracture surfaces in each data set. S_a is the average areal surface roughness, and S_q is the average areal root mean square surface roughness [100].

	$\mathbf{S_a}$ (μm)	$\mathbf{S_q}$ (μm)
PPP	40.8	53.3
SS	31.5	40.8
Vertical	54.2	68.8

path a crack must follow to propagate throughout the material. Therefore, the best explanation available at this time for why the three data sets behave differently from each other is that the differences in microstructure size and morphology among the three data sets dictates very different crack growth behaviors. The large, elongated microstructure from the SS dataset allow the crack to propagate through the grains quickly with relatively few direction changes, and the small microstructure observed in both the PPP and the Vertical datasets create a more tortuous route for the crack to follow which increases the fatigue life significantly.

5.4 Conclusions

In previous chapters, pore size effects on fatigue life were considered, but the effects of applied stress and its interaction with the pore size was neglected. In this investigation, both pore size and applied stress effects were examined. S-N data was obtained from two different data sets, and several results were observed. First, it was seen that the scatter seen in the S-N data was due to interactions between the applied stress and the pore size. When these values were combined into a single stress-intensity term, the scatter was significantly reduced, and the trend was fit using regression analysis to a two term power equation. Next, based on the dK-N regression model and a regression model of wrought S-N data, the El-Haddad model was modified to produce a new finite life prediction model which is sensitive to both applied stress and defect size. This new model also indicates a

threshold defect size for a given stress value for which the AM material will experience a specified life. Therefore, non-destructive inspection of AM components can intelligently look for defects greater than a critical flaw size based on this threshold value, a capability that was previously not available. Third, the data analyzed in this investigation was comparable to prior work which indicates only slight variances in material properties between material. These variances may be explained by significant differences in microstructure size and shape between the three different data sets. It was seen that large-grained material experienced shorter lives than equivalent material with smaller grains.

Rapid Initiation and Growth Life Characterization Through Compliance Monitoring

6.1 Introduction

It has been seen in the previous chapters that the combination of flaw size and fatigue growth properties of AM material dictates the time in which a component under cyclic load will fail. Chapter 3 showed that changes in PPPs produce significantly different pore distributions. Therefore material processing plays an important role in failure defect formation, and probably the number of cycles a crack takes to initiate from a defect. Chapter 4 further illustrated that the different porosity distributions produced via various processing methods indeed influence the fatigue life of the part, and assuming first cycle initiation and Paris law crack growth, the fatigue life of a particular component can be predicted based on supposed initial flaw size and the crack growth properties of the material. Chapter 5 showed that, at least for the material tested, fatigue lives exhibited by additive material perform significantly worse than defect-free wrought material and that as defect size gets smaller, the fatigue life difference between additive material and wrought material becomes negligible.

From the investigations presented in the previous chapters, four questions arise. First, does crack initiation actually occur on the first cycle of fatigue, or does it occur later in the life of a component? Second, is initiation stress and flaw size dependent? Third, do components manufactured under the same processing conditions exhibit the same crack growth properties? Finally how much does processing influence the crack growth properties of a material?

All the questions above require some method to detect crack initiation to distinguish between the crack initiation life and crack growth life of a component. Once these segments of the total life are identified for each component, further analysis can reveal valuable information that will enhance life prediction methods. Several techniques are available for detecting crack initiation and monitoring crack growth including acetate replicas [101–103], CT imaging [104–106], and thermal imaging [107, 108]. One quantity that may be valuable to supplement these proven methods because of its ease of implementation is component compliance. Cai *et al.* and Toribio *et al.* have developed numerical methods to model how compliance changes relate to crack growth in round axial fatigue specimens [109–113]. They have showed that as a crack grows through a component, the stiffness (k) of the component (defined in Eq. 6.1) decreases to zero at final fracture.

$$k = \frac{\Delta F}{\Delta d} \tag{6.1}$$

The compliance (λ) of a component is defined as the inverse of the stiffness or

$$\lambda = \frac{\Delta d}{\Delta F} \tag{6.2}$$

where Δd is the change in displacement from peak to valley of the cyclic load cycle, and ΔF is the change in force in the load cycle. Since the stiffness approaches zero as the crack grows, the compliance approaches infinity as the crack grows. In the absence of a crack or

other damage to a component, the compliance remains constant. As cyclic damage occurs and a crack initiates, the compliance will slowly rise, and continue rising as the crack grows. Monitoring this compliance signal throughout a fatigue test provides a method to detect crack initiation. Once the signal begins to rise, a criterion can be established to identify crack initiation, and distinguish between the number of cycles to initiate a crack and the number of cycles to grow the crack.

6.2 Materials and Methods

In order to demonstrate that specimen compliance does indicate the damage state of the material and to compare the new test method with other accepted methods of crack detection, a set of redundancy tests were performed using both optical imaging and thermal imaging. Four axial fatigue tests were performed using one-eighth inch thick rolled stock flat aluminum specimens designed to fall within ASTM E466 standard specifications for constant radius hourglass fatigue specimens (dimensions shown in Figure 6.1a). A FLIR SC650 thermal camera monitored the thermal profile of the specimen throughout the test, and two Allied Vision Technologies Prosilica cameras were used to monitor both sides of the flat specimens for cracks as shown in Figure 6.1b. For the thermal measurements, it is necessary for the cyclic force to be continually applied during measurement, so the energy released during crack initiation and growth accumulates quicker than convective dissipation. For best results with the optical cameras, however, the component must be held still to obtain a high quality image of small crack features. Therefore, the following work flow was developed to accommodate the thermal, optical, and compliance initiation detection methods. At the beginning of each test, the axial load on the specimen was set to zero, and the axial displacement channel was zeroed. A pulse signal was sent to the thermal camera system to trigger data acquisition, and cyclic loading began at a loading frequency

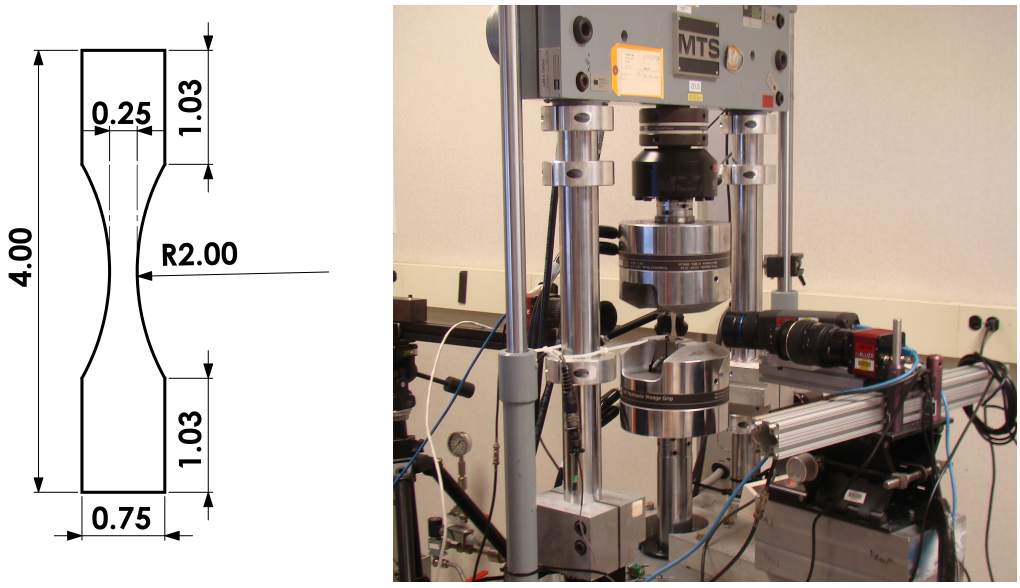

(a) (b)

Figure 6.1: a) Redundancy test specimen geometry based on ASTM E466 flat, hourglass specimen design, b) Redundancy test setup using an MTS 312.21 100 kN servohydraulic loadframe with monitoring using both thermal and optical cameras.

of about 40 Hz. Throughout the test, a peak/valley detector was configured to collect force, displacement, and cycle count data each time the detector detected a peak or valley in the sinusoidal force signal. The thermal camera took an image approximately every twenty cycles for two thousand five hundred cycles, and after the cycles were completed, the frequency was reduced to approximately 0.1 Hz for 1 cycle. At the maximum load of this low frequency cycle, the optical camera was triggered, and a single image was taken. The test frequency then returned to 40 Hz, and the thermal camera was triggered and began acquisition again. This cycle continued until final failure of the component occurred, at which point the data acquisition was stopped. Once the test was completed, the thermal profile at the location of the failure was compiled for each image step, and each optical image was examined to determine when initiation occurred during the test. Once the cycle of initiation was determined from the proven methods, the compliance signal was calculated from the load frame force and displacement sensor data.

Once the testing using the redundant crack detection methods were performed, the

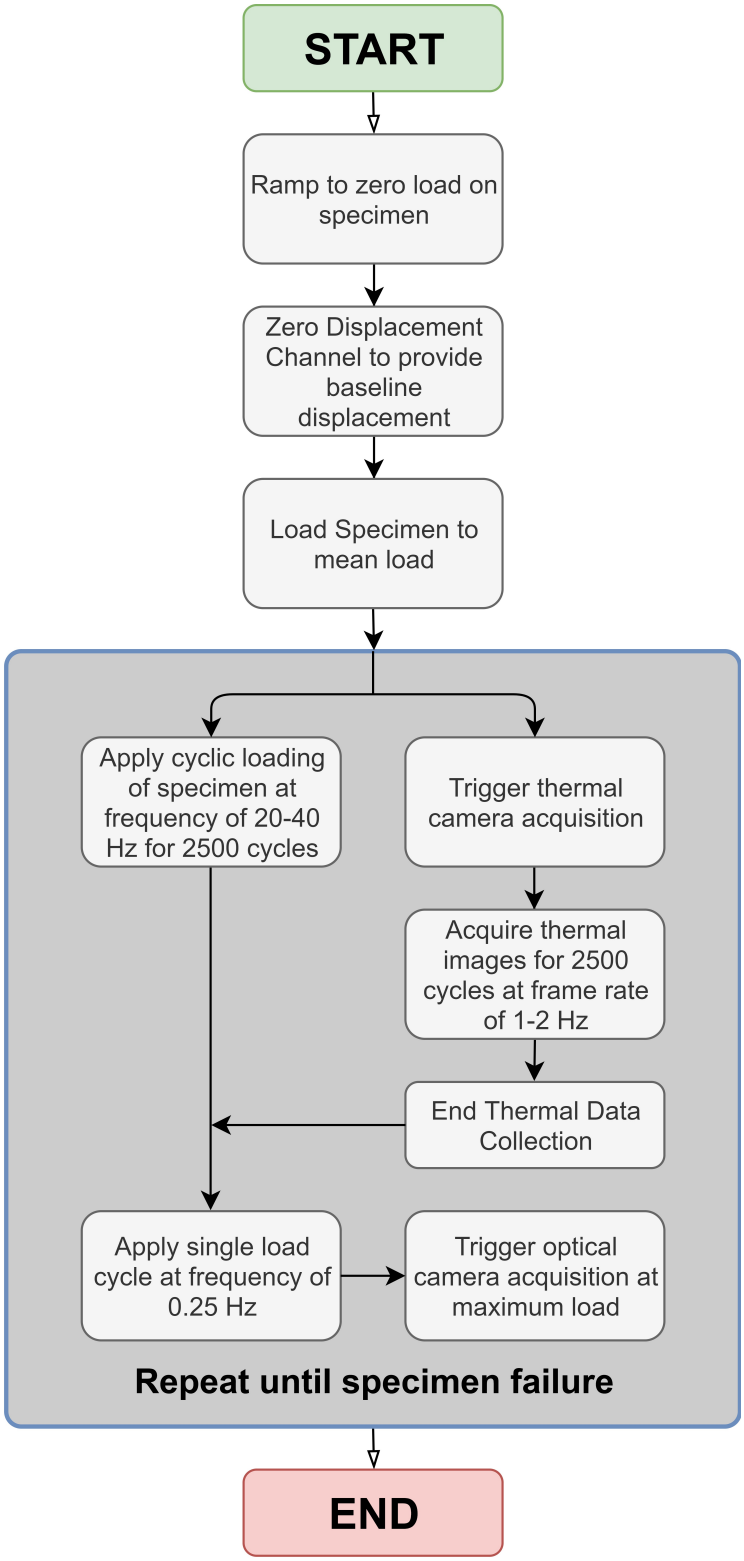

Figure 6.2: Flowchart explaining the data collection procedure for optical and thermal redundancy testing.

Table 6.1: Process parameters for vertical fatigue bar builds

	Power	**Speed**	**Hatch Spacing**	**Layer Thickness**
Vertical A	370 W	700 mm/s	130 μm	40 μm
Vertical B	370 W	700 mm/s	130 μm	80 μm

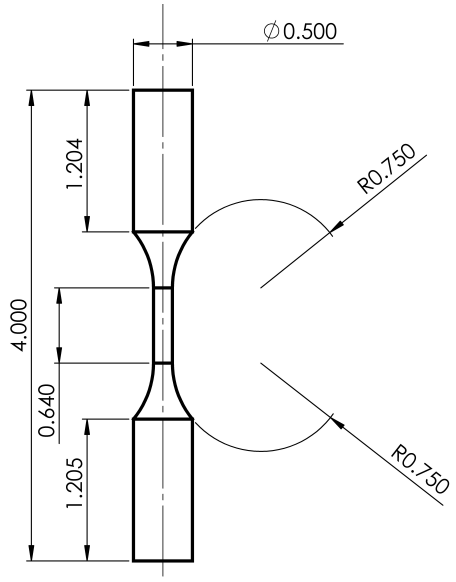

Figure 6.3: Fatigue Specimen Dimensions

fatigue data from the AM specimens described in Chapter 5 was analyzed in this investigation. The processing and specimen information for both the Vertical A and B specimens is recounted here for ease of access. The process parameters are summarized in Table 6.1. The components were stress-relieved on the base plate as described in [19] and heat treated off the plate as described in section 2.2.2. ASTM standard specimens [90] were manufactured from the AM cylinders to the dimensions shown in Figure 6.3.

For each specimen, the applied load, axial displacement, and cycle number was captured at the peak and the valley of each load cycle. From this data, the compliance was calculated using Eq. 6.2.

6.3 Results and Discussion

6.3.1 Compliance Method Development

The calculated compliance signal had a high signal to noise ratio which made observing slight changes in compliance difficult. To remove some of the noise in the system, a moving, weighted linear least squares calculation was performed across the compliance data stream using a first degree polynomial. This method of data smoothing was chosen because of artificial compliance spikes which occured at the end of every twenty-five hundred cycle group. These spikes were smoothed in the data using a first order linear least squares smoothing function which was weighted over a span of neighboring data points to reduce the influence of non-local data points. Further information about the smoothing process can be obtained from Matlab's documentation for filtering and smoothing data [114]. Figure 6.4 shows how the smoothing operation helped to reduce the amount of noise in the signal.

Once the compliance data was smoothed, a sample of the dataset was obtained from the stable portion of the signal at the beginning of the test, and the average baseline compliance value was calculated based on that sample. The percent change (p_{chg}) of the total signal was calculated from the baseline compliance value (λ_0) such that:

$$p_{chg} = \frac{\lambda_s - \lambda_0}{\lambda_s} \tag{6.3}$$

where λ_s is the smoothed compliance signal. Based on λ_s, a criterion was established, so that initiation detection was based off of a standard compliance deviation from baseline. For the redundancy test dataset, compliance-based crack initiation was defined as the approximate cycle at which the smoothed compliance signal initially deviated from the baseline compliance value. This method is not robust, and depends highly on the noise content in the data: Lower signal to noise ratio data obfuscates slight changes in signal mean. For

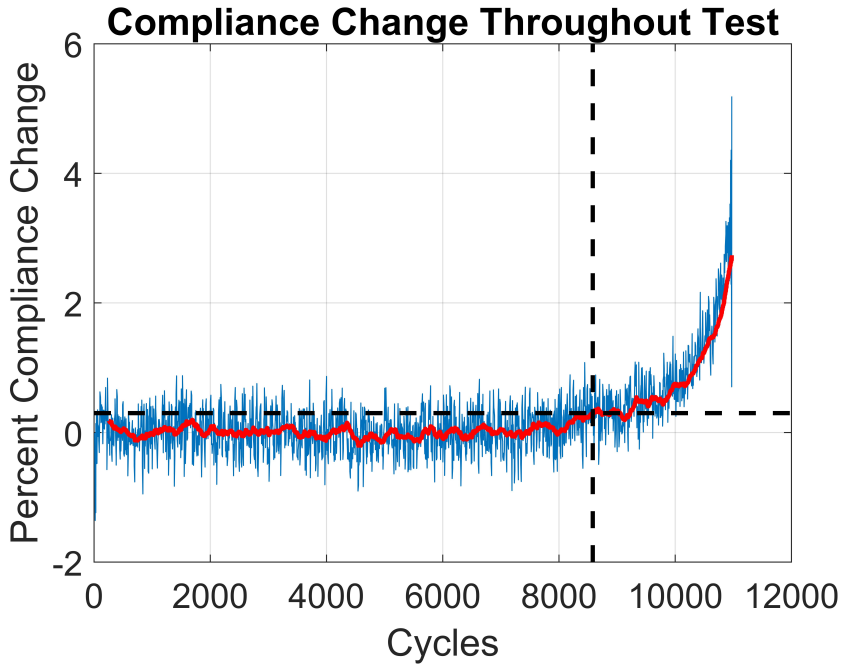

Figure 6.4: Compliance development throughout the duration of an axial fatigue test. Blue data is the raw data, red data is the filtered data, horizontal line indicates a 0.3% change in compliance compared to the baseline, and vertical line indicates the initiation cycle based on the 0.3% threshold.

the analysis of the AM specimen fatigue data, a different criterion was adopted to provide better repeatability between tests. A compliance percent change signal was calculated for each compliance data point from Eq. 6.3, and a threshold was set such that crack initiation was determined by a 0.3% change in compliance from the baseline value.

6.3.2 Redundant Verification of Compliance Test Method

For the tests equipped with redundant thermal and optical sensors, observed initiation from the thermal and optical systems were compared to the initiation phenomena observed in the compliance data. Thermally-observed initiation was based on a sudden temperature rise at the failure location. After the test, a vertical line of pixels that intersected the failure location of the specimen was designated, and time-based thermal data from that line of pixels was collected. It was observed that a "gradient" artifact existed in the thermal data extracted

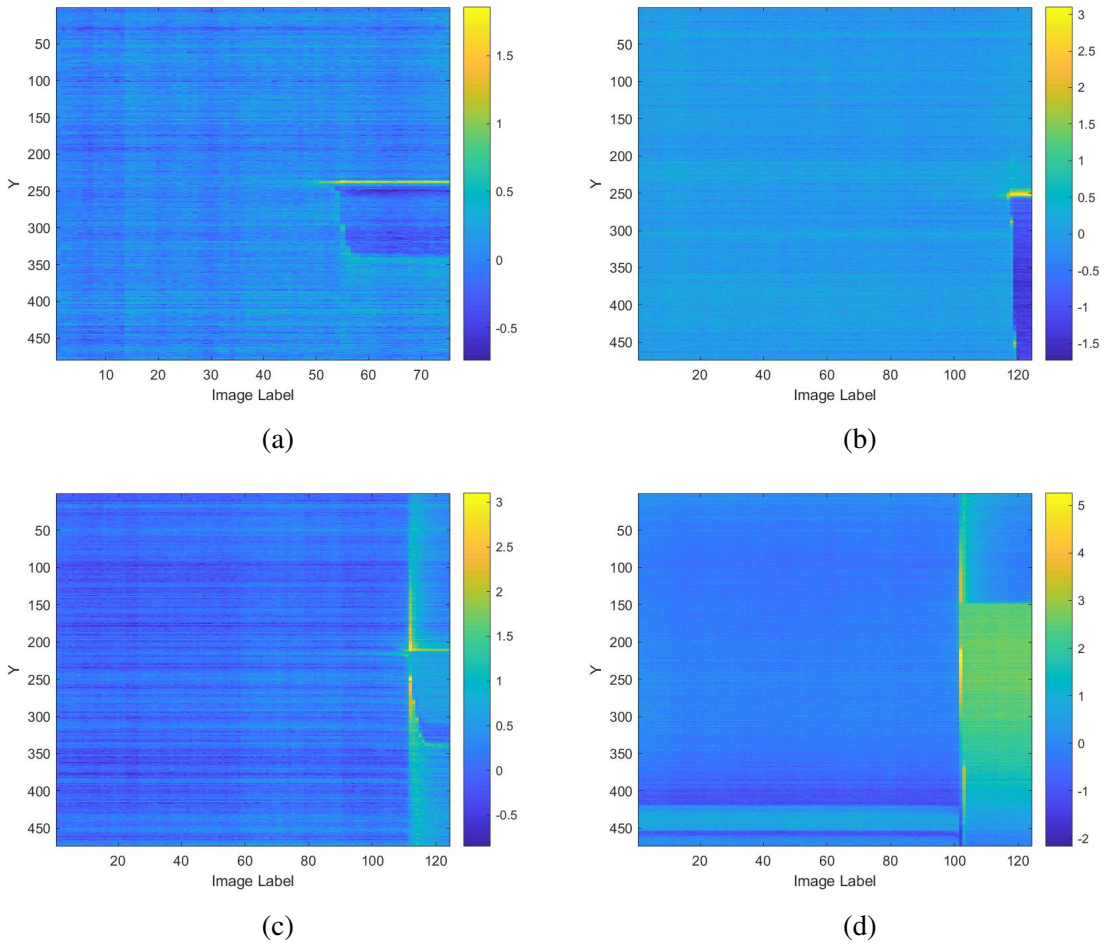

Figure 6.5: Thermal history of failure location for compliance redundancy testing of four specimens.

from the vertical line, but that gradient was consistent throughout the test. Therefore, the baseline thermal gradient profile was calculated using linear, fourth order regression analysis, and the baseline profile was subtracted from each subsequent thermal profile to enhance slight, local changes in the thermal profile. The resulting time-temperature profile was collected from each image in the last data series before failure, and the temperature at the failure location was monitored throughout time as visualized in Figure 6.5. This figure represents only the last 2500 fatigue cycles placed on each part. The x-axis for each image represents the image identifier, and the y-axes represent the axial location along each specimen. The first several data lines in this data set show thermal stability throughout the

Table 6.2: Summary of detected initiation events for compliance signal, thermal images, and optical images

Specimen Number	Total Life	Compliance Initiation Cycle	Thermal Initiation Cycle	Optical Initiation Cycle
1	78597	65000	78460	62500
2	59859	46420	59620	-
3	39735	31600	39620	-
4	94538	72578	94520	82500

length of the specimen up until the time of initiation and failure. At initiation/failure, the temperature at the initiation site rapidly increases, and the temperature in the surrounding region drastically increases at final fracture. This temperature rise is related to the strain energy that is being released in the form of heat as the crack faces separate and grow and as the surrounding material elongates.

Optical images were also taken periodically throughout the fatigue test on either side of the specimen. These images were taken much less frequently than the thermal images due to frame rate limitations of the cameras. For optical images, initiation was specified when damage in the material could be observed. In some cases, this damage was visible long before an actual crack was visible in the material.

Because optical and thermal images were taken at different times during the test, direct correlation between data from each method is not possible. A comparison of the three methods, however, makes clear that compliance detects initiation much earlier in the test than both thermal and optical methods. Both optical and thermal acquisition systems are limited in their field of view to one side at a time. For the case of flat, rectangular specimens as used in the redundancy tests, four component surfaces must be monitored with appropriate spatial resolution and temporal resolution to be able to detect a relatively small crack at precisely the initiation cycle. In this test, only two sides were monitored. The feasibility of obtaining the necessary data at the right location and time is less likely due to computational, storage, and hardware limitations. Table 6.2 shows that generally, compliance growth indicates initiation much sooner in the life than the thermal technique or the optical technique. For small cracks, the SIF is very small. SIF is related to energy release

rate $\mathcal{G}$,the amount of energy required to extend a crack, such that

$$\mathcal{G} = \frac{1-\nu^2}{E} K_I^2 \tag{6.4}$$

where ν is Poisson's ratio and E is Young's modulus [115]. Energy release through crack extension propagates through the material in the form of heat which is observed by the thermal camera. At small stress intensities the energy release rate is very small, so any temperature rise produced by released energy is very small, and dissipates quickly into the surrounding material and air. Therefore, thermal resolution is a limiting factor for the thermal camera method. The optical method exhibits other limitations due to the size of initial cracks. Additionally, in some cases cracks initiate inside the material or on surfaces that are not easily monitored by the camera, so initiation is often unobservable at the macro-scale.

Compliance, on the other hand, is very simple to calculate, and represents damage occurring across the entire test region. Therefore, contrary to the thermal or optical observations which are limited by line of sight effects, compliance has no blind spots and can detect initiation anywhere in the test region. Additionally, compliance requires no extra sensors because it is calculated from data already available from most fatigue tests.

6.3.3 Vertical Specimen Initiation Analysis

Once the compliance method was shown to detect crack initiation more precisely and inexpensively than other proven methods, load and displacement data from the vertical specimens examined in Chapter 5 was aggregated and analyzed. Based on a relative change of 0.3% from the baseline compliance, the crack initiation was detected from the compliance signal and noted for each specimen. Failure defect size was also measured from the fracture surface for each specimen, and the total number of cycles for each specimen at the tested stress was noted. Additionally, the number of cycles for initiation and growth

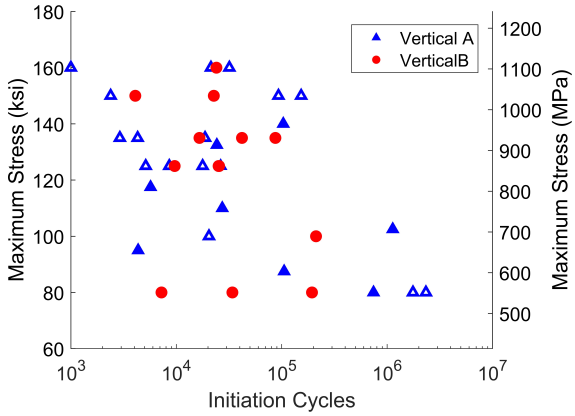

(a)

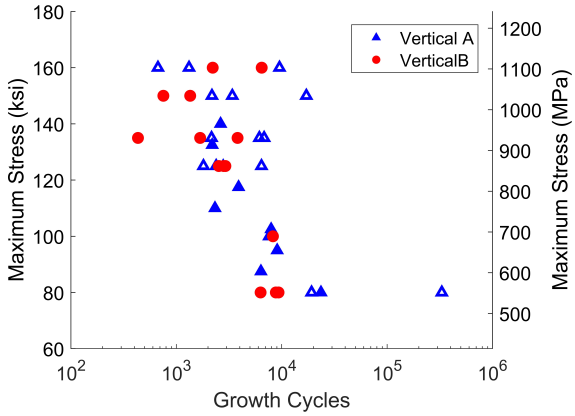

(b)

Figure 6.6: S-N plots for a) cycles to initiation and b)growth cycles to failure.

lives were collected. Figure 6.6 reflects the data trend observed in Figure 5.2 for total life observations: high stresses tend to produce short initiation lives. Additionally, Figure 6.6a shows a uniform amount of scatter of initiation life in logarithmic space while Figure 6.6b exhibits larger scatter at higher stresses and generally smaller amounts of scatter for low stress tests. These observations could indicate that initiation life is sensitive to pore size while growth life is more sensitive to other factors.

One way to test this hypothesis is to include failure pore data in the image by changing the stress value to a stress-intensity based on the failure pore measurements observed in Chapter 6. Figure 6.7 shows that the S-N data collapses onto a single curve when trans-

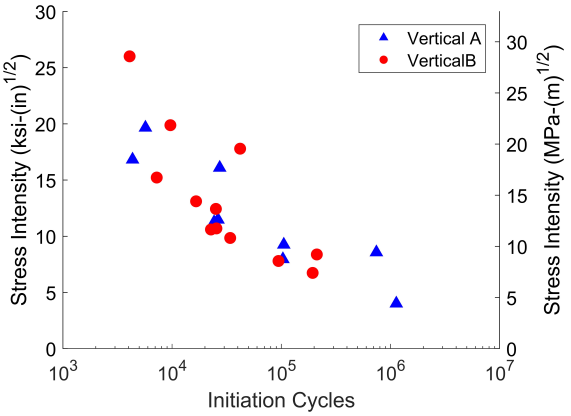

(a)

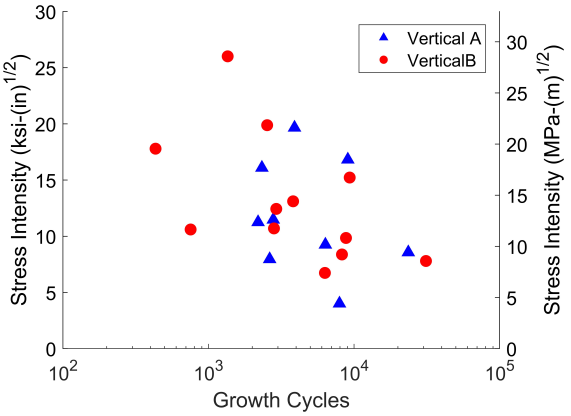

(b)

Figure 6.7: dK-N plots for a) cycles to initiation and b)growth cycles to failure.

formed into dK-dN data for initiation life. The growth life, however does not collapse onto a single curve, however the logarthimic representation of the initiation and growth quantities makes exact comparison very difficult. It can be observed however that crack initiation is dominated by a combination of the applied stress and flaw size. The growth life, while still dependent on crack size and applied stress, depends also on other random variables which may include pore location and/or local grain structure, and microstructure texture which all play a role in how quickly a crack grows through a material.

The literature has suggested that for components undergoing low cyclic stresses, crack initiation accounts for up to 90% of the total life while in situations where high stresses oc-

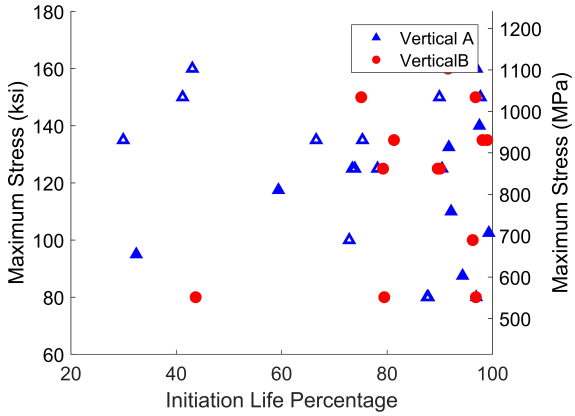

(a)

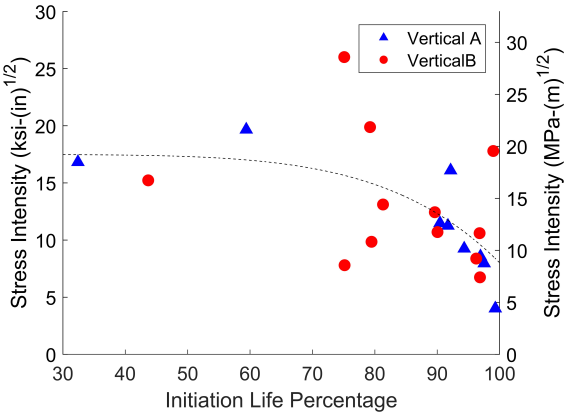

(b)

Figure 6.8: Percentage of total life spent initiating a crack from a flaw with respect to a) maximum stress applied to component and b) maximum stress intensity experienced at the failure location.

cur, initiation may account for less than 40% of the total life [116, 117]. For the Vertical specimens, the percentage of the total life taken up by crack initiation as detected by compliance was calculated for each specimen, and plotted in Figure 6.8a. This figure shows no trend to indicate that initiation life percentage goes down as stress goes up. Figure 6.8b, on the other hand shows that apart from a few outliers, the general trend of initiation life with respect to stress intensity is to decrease as stress intensity increases. Therefore, for larger flaws and higher stresses, the initiation life is significantly reduced to about 30%. Conversely, for small flaws and low stresses, components exhibit initiation lives of about

95-99% the total life. This observation falls in line with the literature. Therefore, it is probable that the first-cycle initiation theory does not accurately represent the true behavior of porous additive material behavior. Instead, a pore initiates a crack in direct relation to the pore's size, location, and applied stress. Then, depending on the local microstructure morphology and texture, the crack grows according to some crack propagation behavior until component failure.

Assuming that each component propagates a crack in a similar manner, the average material behavior can be predicted using crack propagation models. The initial flaw size is known from fractography, the final crack size is calculated based on the normal stress in the ligament exceeding the ultimate strength of the material, and the stress intensity shape factor is known from the defect location. The constants that are unknown are from the crack growth model. Both the Paris law and the NASGRO equations were used to model the growth lives of the Vertical specimens. Based on the initial flaw size and location and the applied stress, the growth life of each component was calculated and compared to the actual growth lives obtained from compliance monitoring. The crack growth constants from both the Paris law and the NASGRO equation were modified to minimize the error between the predicted and actual growth lives. These comparisons are shown in Figure 6.9. Figure 6.9a shows that the predicted lives group around the one to one line, but there is significant scatter outside the 2x scatter band which shows that the error between the model and the experimental data is relatively large. In the case of fatigue, however, it is probable that the error in this calculation is acceptable because of the differences in microstructure, pores along the crack path, and location effects on stress intensity. Figure 6.9b illustrates a similar picture. Fewer data points are shown on this plot because of the average threshold value used in the NASGRO model. Any initial flaws that produce a stress intensity below the threshold value assumed by the model experience dramatically increased lives.

The scatter in the growth life comparison illustrates there is some inconsistency in the way the growth lives are specified or modeled. Either, the growth lives determined by

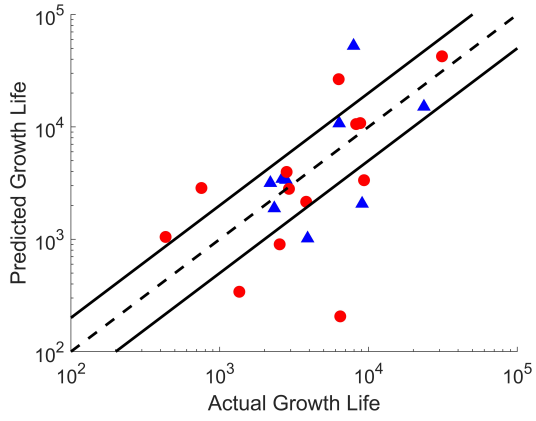

(a)

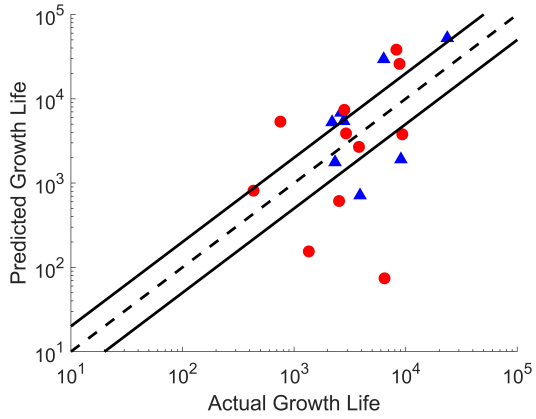

(b)

Figure 6.9: Comparison of actual component growth lives obtained from compliance monitoring and predicted growth lives calculated from a) Eq. 2.13 and b) integration of Eq. 2.12.

changes in compliance do not accurately represent the actual growth lives, or the average model does not accurately represent each individual specimen (i.e. Each specimen exhibits slightly different fatigue crack properties.) The first hypothesis does not seem probable because redundant methods of crack detection were compared to the compliance crack detection method, and compliance appeared to detect cracks significantly sooner than the other methods. The second hypothesis must be investigated in the future. Currently, there was not data taken during the tests to track the progress of the crack growth. In the future, this exercise must be performed and compared to the compliance development. Once a relationship is derived between crack length and compliance, the data presented above can be in terms of serial number specific crack growth properties, and the differences in those properties can be compared.

6.4 Conclusion

In this chapter, a method was adapted from previous literature to detect fatigue crack initiation in AM materials. It was shown that compliance (as defined in Eq. 6.2) remains constant throughout a constant amplitude fatigue test, and once crack initiation occurs, the compliance increases dramatically until failure of the component occurs. The crack initiation event was monitored for several test cases using proven methods of crack initiation detection including both thermal and optical imaging, and it was shown that the compliance method of crack detection was much more sensitive than the other methods. In some cases, compliance was able to detect initiation up to twenty-two thousand cycles before the other methods.

Based on the number of cycles to initiation detected by compliance in the Vertical AM specimens, it was shown that initiation life data followed a power trend with stress intensity factor while growth life data did not. It was confirmed, however, that the percentage of the total component life used to initiate a crack follows a loose trend with stress-intensity factor

at the failure location which indicates that the percent of the total life used to initiate a crack is related both to the stress applied to the component as well as the defect residing at the failure location. Specifically, for high stress-intensity tests, the percent of the total life spent in the initiation phase is approximately 25% while in low stress-intensity tests, that ratio increases to close to 90%. These values are similar to previously published assertions, and they indicate that the first cycle assumption for failure of AM materials is not true.

Based on the initiation life detection, it was shown that average crack growth properties can be determined from the growth life data based on initial and final crack sizes. These approximations were found to contain some level of error, but it is believed that the level of error is acceptable for this application. Future studies will work to use compliance data directly to determine the serial number specific crack growth properties which can be used to obtain statistically significant data sets in a relatively small number of tests.

Conclusions

As part of this research, experimental investigations have been performed to quantify the influence of processing on the structure, properties, and performance of AM materials. These investigations included observations of defect populations and their dependence on material processing, fatigue life predictions based on porosity distributions, further observations of applied stress and defect size interaction effects on fatigue life of AM components, and a novel approach to crack initiation detection and rapid characterization of fatigue properties of materials. Based on the results and subsequent analyses, the following conclusions were drawn.

7.1 Summary

1. Porosity data was collected from a large number of specimens and regression models were developed to describe the trends of pore size and pore density with respect to four PPP variables: beam power, scan speed, hatch spacing, and layer thickness.

2. Pore regression model trends indicate an optimal process parameter region bounded by two non-optimal regions. This trend corroborates previously observed phenomena keyhole mode and LOF melting.

3. Three literature porosity prediction models were compared with the collected experimental data, and it was shown that each have a different level of utility for predicting

porosity in AM components

(a) Tang's Rosenthal-based model can give a good first-order approximation of which combinations of PPPs will produce LOF porosity. This approach, however, neglects the physics occurring as the melt pools overlap, and should be further investigated to verify actual behavior.

(b) Volumetric Energy Density is a good rule of thumb for how porosity characteristics will react to a change in a single PPP, but the effects of each individual PPP are confounded in the final calculation which makes the specific application of this method inaccurate for predicting porosity across a wide region of process space.

(c) King's normalized enthalpy model provides a good approximation of a threshold beyond which keyhole porosity will occur.

4. A method was proposed to predict axial fatigue lives of components given the porosity size distributions observed in the components via CT. This method was proven to be accurate for a small sample of specimens.

5. The effects of PPPs on porosity were found to transfer directly to significant effects on fatigue life. Components exhibiting differences in both PPPs and scan strategy exhibited significantly different porosity distributions, and a corresponding fatigue performance change was directly observed for each component.

6. S-N curves were produced for a larger AM dataset, and failure defects were catalogued for each component.

7. Scatter in S-N data was collapsed to a single curve by combining the effects of stress and defect size into a stress-intensity value. This curve approached a single stress intensity value as the life of the part increased.

8. Based on observations , the El-Haddad fatigue limit model was adapted to produce a novel finite life prediction framework based on applied stress and flaw size.

9. A rapid fatigue performance characterization technique was developed using specimen compliance monitoring.

10. Initial results showed that compliance indicates material damage prior to other proven methods.

11. It was shown that initiation life has a direct relationship to the stress intensity produced by the material defect.

12. Identification of initiation life for each specimen illustrated that for porous AM materials, the initiation stage of fatigue accounts for down to 25% of the total life for high stresses and large defects and up to 90% of the total life for low stresses and small defects which falls in line with previous observations in traditionally manufactured materials.

7.2 Contributions

1. Examined PPP trends across LPBF process space

2. Interrogated literature porosity prediction models using experimental data

3. Developed a pore-based fatigue life prediction method

4. Identified beam PPP influence on fatigue life

5. Quantified fatigue life debit induced by a pore of a given size compared to fatigue life of wrought alloy

6. Adapted fatigue limit prediction methodologies to predict finite life using pore and stress data.

7. Identified critical pore size for achieving a infinite/finite life for a given stress state

8. Developed a compliance-based characterization method for rapid characterization of fatigue performance of AM materials

Recommendations

The work performed in this dissertation has built on the work of others and introduced new ways to characterize AM material and predict the performance of AM components. However, the pursuit of greater knowledge and better understanding of AM processes and their products must still continue. Therefore, based on the work presented in the previous chapters, it is recommended that the following work be performed in the future to increase the maturity of the technology and increase the applicability of AM to widespread structural applications.

1. Continued production of AM fatigue life and crack propagation data using standard test methods.

2. Further development of compliance-based fatigue characterization procedure and analysis.

    (a) Identify relationships between crack size and compliance development using either intermittent crack monitoring, in-situ observation techniques, or post-failure observations.

    (b) Identify localized methods of monitoring compliance in order to identify position of initiation sooner in the life of the part.

    (c) Investigate the effects of specimen geometry on compliance development.

    (d) Identify the relationships between initial crack location and shape on the compliance development.

3. Comparison of compliance-based fatigue measurements to material properties observed using standardized test methods.

4. Application of methods developed herein to other process induced defects or anomalies including surface roughness.

Bibliography

[1] K Moussaoui, W Rubio, M Mousseigne, T Sultan, and F Rezai. Effects of selective laser melting additive manufacturing parameters of Inconel 718 on porosity, microstructure, and mechanical properties. *Mat. Sci. Eng. A*, 735:182–190, 2018.

[2] *Metallic Materials Properties Development and Standardization (MMPDS)*, volume 1. 2015.

[3] J Fielding, R Gorham, A Davis, B Bouffard, and K Morris. Department of defense joint additive manufacturing roadmap. Nov. 2016.

[4] T Vilaro, C Colin, and J Bartout. As-fabricated and heat treated microstructures of the Ti-6Al-4V alloy processed by selective laser melting. *Met. Mater. Trans. A*, 42:3190–3199, 2011.

[5] R Cunningham, S Narra, T Ozturk, J Beuth, and A Rollett. Evaluating the effect of processing parameters on porosity in electron beam melted Ti-6Al-4V via synchotron x-ray microtomography. *JOM*, 68:765–771, 2016.

[6] H Gong, K Rafi, H Gu, T Starr, and B Stucker. Analysis of defect generation in ti-6al-4v parts made using powder bed fusion additive manufacturing processes. *Addit. Manuf.*, 1-4:87–98, 2014.

[7] G Kasperovich, J Haubrich, J Gussone, and G Requena. Correlation between porosity and processing parameters in TiAl6V4 produced by selective laser melting. *Mater. Des.*, 105:160–170, 2016.

[8] L Sheridan, O Scott-Emuakpor, T George, and J Gockel. Relating porosity to fatigue failure in additively manufactured alloy 718. *Mat. Sci. and Eng. A*, 727:170–176, 2018.

[9] M Zhang, C Sun, X Zhang, J Wei, D Hardacre, and H Li. Predictive models for fatigue property of laser pwder bed fusion stainless steel 316L. *Mater. Des.*, 145:42–54, 2018.

[10] D Rosenthal. The theory of moving sources of heat and its application to metal treatments. *Transactions of the American Society of Mechanical Engineers*, 68:849–866, 1946.

[11] A Vasinonta, J Beuth, and R Ong. Melt pool size control in thin-walled and bulky parts via process maps. In *Proceedings of the SFF*, 2001.

[12] E Soylemez, J Beuth, and K Taminger. Controlling melt pool dimensions over a wide range of material deposition rates in electron beam additive manufacturing. In *Proceedings of the SFF*, 2010.

[13] J E Gockel, J Beuth, and K Taminger. Integrated control of solidification microstructure and melt pool dimensions in electron beam wirefeed additive manufacturing of Ti-6Al-4V. *Additive Manuf.*, 1-4:119–126, 2012.

[14] C Montgomery, J Beuth, L Sheridan, and N Klingbeil. Process mapping of Inconel 625 in laser powder bed additive manufacturing. In *Solid Freeform Fabrication Symposium Proceedings*, 2015.

[15] L Sheridan. An adapted approach to process mapping across alloy systems and additive manufacturing processes. Master's thesis, Wright State University, 2016.

[16] U S Bertoli, A J Wolfer, M J Matthews, J P R Delplanque, and JM Schoenung. On the limitations of volumetric energy density as a design parameter for selective laser melting. *Mater. Des.*, 113:331–340, 2017.

[17] Concept Laser. User manual CL WRX parameter, 2016.

[18] M A Groeber, E Schwalbach, S Donegan, K Chaput, T Butler, and J Miller. Application of characterization, modelling, and analytics towards understanding process-structure linkages in metallic 3d printing. *IOP Conf Series: Materials Science and Engineering*, 219, 2017.

[19] ASTM. 3055 - standard specification for additive manufacturing nickel alloy (UNS N07718) with powder bed fusion. *ASTM Book of Standards*, 2014.

[20] T Antonsson and H Fredriksson. The effect of cooling rate on the solidification of Inconel 718. *Metallurgical and Materials Transactions B*, 36B:85–96, 2005.

[21] R R Dehoff, M M Kirka, F A List, K A Unocic, and W J Sames. Crystallographic texture engineering through novel melt strategies via electron beam melting: Inconel 718. *Mater. Sci. and Technol.*, 31(8), 2015.

[22] R R Dehoff, M M Kirka, W J Sames, H Bilheux, A S Tremsin, L E Lowe, and S S Babu. Site specific control of crystallographic grain orientation through electron beam additive manufacturing. *Mater. Sci. and Technol.*, 31(8):931–938, 2015.

[23] B Whip, L Sheridan, and J Gockel. The effect of primary processing parameters on surface roughness in laser powder bed additive manufacturing. *The Int. J. of Adv. Manuf. Tech.*, 2019.

[24] G T Loughnane, S L Kuntz, N Klingbeil, J M Sosa, J Irwin, A R Nassar, and E W Reutzel. Application of a microstructural characterization uncertainty quantification framework to widmanstatten α-laths in additive manufactured Ti-6Al-4V. In *Proceedings of the SFF*, 2015.

[25] M Seifi, D Christiansen, J Beuth, and J J Lewandowski. Process mapping, fracture and fatigue behavior of Ti-6Al-4V produced by ebm Additive Manufacturing. In *Proceedings of the 13th World Conference on Titanium*, 2016.

[26] L E Criales, Y M Arisoy, B Lane, S Moylan, and A Donmez. Laser powder bed fusion of nickel alloy 625: experimental investigations of effects of process parameters on melt pool size and shape with spatter analysis. *Int. J. Mach. Tools Man.*, 121:22–36, 2017.

[27] M Tang. *Inclusions, porosity, and fatigue of ALSi10Mg parts produced by selective laser melting*. PhD thesis, Carnegie Mellon University, 2017.

[28] W E King, H D Barth, V M Castillo, G F Gallegos, J W Gibbs, D E Hahn, C Kamath, and A M Rubenchik. Observation of keyhole-mode laser melting in laser powder-bed fusion additive manufacturing. *J. of Mat. Proc. Tech.*, 214:2915–2925, 2014.

[29] L Thijs, F Verhaeghe, T Craeghs, J Van Humbeeck, and J P Kruth. A study of the microstructural evolution during selective laser melting of Ti-6Al-4V. *Act. Mat.*, 58:3303–3312, 2010.

[30] H Gong, K Rafi, H Gu, G D Janaki Ram, T Starr, and B Stucker. Influence of defects on mechanical properties of Ti-6Al-4V components produced by selective laser melting and electron beam melting. *Mater. Des.*, 86:545–554, 2015.

[31] A B Spierings, K Wegner, and G Levy. Designing material properties locally with additive manufacturing technology SLM. In *Proceedings of the SFF*, 2012.

[32] L Sheridan, J E Gockel, and O E Scott-Emuakpor. Primary processing parameters, porosity production, and fatigue prediction for additively manufactured alloy 718. *J. of Mat. Eng. and Performance*, 28(9):5387–5397, 2019.

[33] K Darvish, Z W Chen, and T Pasang. Reducing lack of fusion during selective laser melting of CoCrMo alloy: Effect of laser power on geometrical features of tracks. *Mater. Des.*, 112:357–366, 2016.

[34] Z Francis. *The effects of laser and electron beam spot size in additive manufacturing processes*. PhD thesis, Carnegie Mellon University, 2017.

[35] G Vastola, Q X Pei, and Y W Zhang. Predictive model for porosity in powder-bed fusion additive manufacturing at high beam energy regime. *Additive Manuf.*, 22:817–822, 2018.

[36] Daniel Greitemeier, Frank Palm, Freerk Syassen, and Tobias Melz. Fatigue performance of additive manufactured TiAl6V4 using electron and laser beam melting. *Int. J. Fatigue*, 94:211–217, 2017.

[37] V Le, E Pessard, F Morel, and F Edy. Influence of porosity on the fatigue behaviour of additively fabricated TA6V. *MATEC Web of Conferences*, 165:1–9, 2018.

[38] B Liu, R Wildman, C R Tuck, I Ashcroft, and R J M Hague. Investigation the effect of particle size distribution on processing parameters optimisation in selective laser melting process. In *Solid Freeform Fabrication Symposium Proceedings*, 2011.

[39] A Morri, L Ceschini, I L Svensson, and S Seifeddine. Relationship between pore volume (by density measurements) and pore area (on fracture surfaces) of a356 fatigue specimens. In *Supplemental Proceedings: Volume 2: Materials Properties, Characterization, and Modeling*, 2012.

[40] M Letenneur, A Kreitchberg, and V Brailovski. Optimization of laser powder bed fusion processing using a combination of melt pool modeling and design of experiment approaches:Density control. *J. Man. and Mat. Proc.*, 3, 2019.

[41] Y Murakami. *Metal fatigue: effects of small defects and nonmetallic inclusions*, chapter Stress Concentration, pages 17–22. Elsevier Science, 2002.

[42] Y Murakami and T Endo. Effects of small defects on fatigue strength of metals. *IJF*, 2:23–30, 1980.

[43] Y Murakami and M Endo. Effects of defects, inclusions, and inhomogeneities on fatigue strength. *IJF*, 16:163–182, 1994.

[44] Y Murakami and S Beretta. Small defects and inhomogeneities in fatigue strength: Experiments, models and statistical implications. *Extremes*, 2:123–147, 1999.

[45] Special Metals, Inc. Inconel alloy 718 datasheet, 2007.

[46] K N Amato, S M Gatan, L E Murr, E Martinez, P W Shindo, J Hernandez, S Collins, and F Medina. Microstructures and mechanical behavior of Inconel 718 fabricated by selective laser melting. *Acta Materialia*, 60:2229–2239, 2012.

[47] Q Jia and D Gu. Selective laser melting additive manufacturing of Inconel 718 superalloy parts: Densification, microstructure and properties. *J. of Alloys and Compounds*, 585:713–721, 2014.

[48] A Odabasi, N Unlu, G Goller, M N Eruslu, and E S Kayali. Relationship between heat input and microstructure and mechanical properties of laser beam welded superalloy Inconel 718. In *TMS supplemental proceedings: Materials Processing and Interfaces*, 2012.

[49] A Strondl, R Fischer, G Frommeyer, and A Schneider. Investigations of MX and

gamma prime and gamma double prime precipitates in the nickel-based superalloy 718 produced by electron beam melting. *Mat. Sci. and Eng. A*, 480:138–147, 2008.

[50] A Strondl, M Palm, J Gnauk, and G Frommeyer. Microstructure and mechanical properties of nickel based superalloy IN718 produced by rapid prototyping with electron beam melting. *Mat. Sci. and Tech.*, 27:876–883, 2011.

[51] W A Tayon, R N Shenoy, M R Redding, R K Bird, and R A Hafley. Microstructure and mechanical properties in and Inconel 718 deposit produced via electron beam freeform fabrication. *J. of Man. Sci. and Eng.*, 136, 2014.

[52] Y Tian, D McAllister, H Coljin, M Mills, D Farson, M Nordin, and S Babu. Rationalization of microstructure heterogeneity in Inconel 718 builds made by the direct laser additive manufacturing process. *Met. and Mat. Trans. A*, 45A:4470–4483, 2014.

[53] R R Dehoff, M M Kirka, E Ellis, V Paquit, P Nandwana, and A Plotkowski. Electron beam melting technology improvements. Technical report, Oak Ridge National Laboratory, 2019.

[54] W Huang, Z Wang, J Yang, H Yang, and X Zeng. Effects of process parameters and heat treatment on the microstructure and mechanical properties of selective laser melted Inconel 718. In *Proceedings of the SFF*, 2018.

[55] D J Newell, R P O'Hara, G R Cobb, A N Palazotto, M M Kirka, L W Burggraf, and J A Hess. Mitigation of scan strategy effects and material anisotropy through supersolvus annealing in LPBF IN718. *Mat. Sci. & Eng. A*, 2019.

[56] American Metallurgical Society. AMS 2774: Heat treatment wrought nickel alloy and cobalt alloy parts, 2016.

[57] Stratasys. Inconel 718 direct metal laser sintering material specifications, 2015.

[58] Concept Laser. Cl 100NPB nickel-based alloy, 2019.

[59] A C Ugural and S K Fenster. *Advanced strength and applied elasticity*. Pearson Education, Inc., 4 edition, 2003.

[60] G R Irwin. Analysis of stresses and strains near the end of a crack traversing a plate. *J. of App. Mech.*, 24:361–364, 1957.

[61] M Grasso, A De Iorio, Y Xu, and G Haritos. An analytical model for the identification of the threshold of stress intensity factor range for crack growth. *Adv. in Mat. Sci. Eng.*, 3:1–13, 2017.

[62] P Paris and F Erdogan. A critical analysis of crack propagation laws. *J. of Basic Eng.*, pages 528–534, December 1963.

[63] NASA-JSC and SwRI. *NASGRO® fracture mechanics and fatigue crack growth analysis software*, 2002. Version 4.02.

[64] R Konecna, L Kunz, Gianni Nicolletto, and A Baca. Long fatigue crack growth in Inconel 718 produced by selective laser melting. *Int. J. Fatigue*, 92(2):499–506, 2016.

[65] S Sui, J Chen, E Fan, H Yang, X Lin, and W Huang. The influence of Laves phases on the high-cycle fatigue behavior of laser additive manufactured Inconel 718. *Mat. Sci. Eng. A*, 695:6–13, 2017.

[66] S Gribbin, S Ghorbanpour, N C Ferreri, J Bicknell, I Tsukrov, and M Knezevic. Role of grain structure, grain boundaries, crystallographic texture, precipitates, and porosity on fatigue behavior of inconel 718 at room and elevated temperatures. *Mat. Characterization*, 149:184–197, 2019.

[67] O Scott-Emuakpor, J Schwartz, T George, C Holycross, C Cross, and J Slater. Bending fatigue life charactersation of direct metal laser sintering nickel alloy 718. *Fatigue and Fracture of Eng. Mat & Struct.*, 38:1105–1117, 2015.

[68] H Kitagawa and S Takahashi. Application of fracture mechanics to very small cracks or the cracks in the early stage. In *2nd International Conference on Mechanical Behaviour of Materials*, pages 627–630, 1976.

[69] M H El Haddad, K N Smith, and T H Topper. Fatigue crack propagation of short cracks. *Trans. of the ASME*, 101:42–46, 1979.

[70] S Beretta, M Carboni, and M Madia. Modelling of fatigue thresholds for small cracks in a mild steel by "strip-yield" model. *Eng Fract Mech*, 76:1548–1561, 2009.

[71] S Beretta and S Romano. A comparison of fatigue strength sensitivity to defects for materials manufactured by am or traditional processes. *IJOF*, 94:178–191, 2017.

[72] J Gumpinger, A Brand ao, E Beevers, T Rohr, T Ghidini, S Beretta, and S Romano. Expression of additive manufacturing surface irregularities through a flaw-based assessment. In *STP ASTM Sympoisum AM structural integrity*, 2018.

[73] S Romano, A Brand ao, J Gumpinger, M Gschweitl, and S Beretta. Qualification of AM parts: Extreme value statistics applied to tomographic measurements. *Mat. & Des.*, 131:32–48, 2017.

[74] S Romano, A Bruckner-Foit, A Brandao, J Gumpinger, T Ghidini, and S Beretta. Fatigue properties of AlSi10Mg obtained by additive manufacturing: Defect-based modelling and prediction of fatigue strength. *Engineering Fracture Mechanics*, 187:165–189, 2018.

[75] S Romano, S Miccoli, and S Beretta. A new FE post-processor for probabilistic

fatigue assessment in the presence of defects and its application to AM parts. *IJOF*, 125:324–341, 2019.

[76] W S Rasband. Imagej. National Institutes of Health, 2017. https://imagej.nih.gov/ij/.

[77] G Chen, Q Zhou, S Y Zhao, J O Yin, P Tan, Z F Li, Y Ge, J Wang, and H P Tang. A pore morphological study of gas-atomized Ti-6Al-4V powders by scanning electron microscopy and synchrotron X-ray computed tomography. *Powder Technology*, 330:425–430, 2018.

[78] L Li, G Peng, J Wang, J Gong, and H Li. Experimental study on weld formation of Inconel 718 with fiber laser welding under reduced ambient pressure. *Vacuum*, 151:140–147, 2018.

[79] E Chlebus, K Gruber, B Kuznicka, J Kurzac, and T Kurzynowski. Effect of heat treatment on the microstructure and mechanical properties of Inconel 718 processed by selective laser melting. *Mater. Sci. Eng., A*, 639:647–655, 2015.

[80] Onome Scott-Emuakpor, Casey Holycross, Tommy George, Kevin Knapp, and Joseph Beck. Fatigue and strength studies of Titanium 6Al-4V fabricated by direct metal laser sintering. *J. Eng. for Gas Turbines and Power*, 138, 2016.

[81] Aref Yadollahi, Nima Shamsaei, Scott M Thompson, Alaa Elwany, and Linkan Bian. Effects of building orientation and heat treatment on fatigue behavior of selective laser melted 17-4 PH stainless steel. *Int. J. Fatigue*, 94:218–235, 2017.

[82] J Gockel, L Sheridan, S P Narra, N W Klingbeil, and J Beuth. Trends in solidification grain size and morphology for additive manufacturing of Ti-6Al-4V. *JOM*, 69(12):2706–2710, 2017.

[83] A Vasinonta. Process maps for predicting residual stress and melt pool size in the

laser-based fabrication of thin-walled structures. *J. of Manuf. Sci. Eng.*, 129(1):101–109, 2006.

[84] R Cunningham, S P Narra, Tugce Ozturk, Jack Beuth, and A D Rollet. Synchotron-based x-ray microtomography characterization of the effect of processing variables on porosity formation in laser powder-bed additive manufacturing of Ti-6Al-4V. *JOM*, 69(3):765–771, 2017.

[85] R Rashid, S H Masood, D Ruan, S Palanisamy, R A Rahman Rashid, and M Brandt. Effect of scan strategy on density and metallurgical properties of 17-4PH parts printed by selective laser melting (SLM). *J. Mat. Proc.*, pages 502–511, 2017.

[86] Q Zhang, Z Zuo, and J Liu. Numerical analysis for the influence of casting micro-porosity on fatigue life. *Eng. Failure Analysis*, 48:11–20, 2015.

[87] R A Hardin. Integrated design of castings: effect of porosity on mechanical performance. *Mater. Sci. Eng., A*, 33, 2012.

[88] M Tiryakioglu. On the relationship between statistical distributions of defect size and fatigue life in 7050-T7451 thick plate and A356-T6 castings. *Mater. Sci. Eng., A*, 520:114–120, 2009.

[89] Tatsujiro Miyazaki, Hyogyoung Kang, Hiroshi Noguchi, and Keisaku Ogi. Prediction of high-cycle fatigue life reliability of aluminum cast alloy from statistical characteristics of defects at meso-scale. *Int. J. Mech. Sci.*, 50:152–162, 2008.

[90] ASTM. E466 - standard practice for conducting force controlled constant amplitude axial fatigue tests of metallic materials. *ASTM Book of Standards*, 2015.

[91] T Nicholas. *High Cycle Fatigue*, chapter 3. Elsevier, 2006.

[92] C Hohnbaum. Fracture toughness and fatigue crack growth rate characterization of

Inconel 718 formed by laser powder bed fusion. Master's thesis, Air Force Institute of Technology, 2019.

[93] A Turnbull and E R De Los Rios. The effect of grain size on fatigue crack growth in an aluminium magnesium alloy. *Fat. & Fract. of Egr. Mat. & Struct.*, 18:1355–1366, 1995.

[94] J Masounave and J P Baflon. Effect of grain size on the threshold stress intensity factor in fatigue of a ferritic steel. *Scripta Metallurgica*, 10:165–170, 1976.

[95] D Eylon and P J Bania. Fatigue cracking characteristics of β-annealed large colony Ti-11 alloy. *Met. Trans. A*, 9:1273–1279, 1978.

[96] E K Priddle. The influence of grain size on threshold stress intensity for fatigue crack growth in AISI 316 stainless steel. *Scripta Metallurgica*, 12:49–56, 1978.

[97] D Eylon. Faceted fracture in beta annealed titanium alloys. *Met. Trans. A*, 10:311–317, 1979.

[98] *Metals Handbook*, page 332. American Society for Metals, 9th edition, 1985.

[99] J Hunt. Steady state columnar and equiaxed growth of dendrites and eutectic. *Mat Sci and Eng.*, 65:75–83, 1984.

[100] ISO. Geometrical product specifications (gps)-surface texture: Areal part2: Terms definitions and surface texture parameters. 2012.

[101] R O Ritchie and J Lankford, editors. *Small fatigue cracks*. American Institute of Mining and Metallurgical Engineers, 1986.

[102] M H Swain, R A Everett, Jr. J C Newman, and E P Phillips. The growth of short cracks in 4340 steel and aluminum-lithium 2090, 1990.

[103] J M Larsen and J E Allison, editors. *Small-crack Test Methods, ASTM STP 1149*. American Society for Testing and Materials, 1992.

[104] S Tammas-Williams, P J Withers, I Todd, and P B Prangnell. The influence of porosity on fatigue crack initiation in additively manufactured titanium components. *Scientific Reports*, 7, 2017.

[105] R Biswal, X Zhang, M Samir, A Al Mamun, M Awd, F Walther, and A K Syed. Interrupted fatigue testing with periodic tomgraphy to monitor porosity defects in wire + arc additive manufactured Ti-6Al-4V. *Additive Manufacturing*, 28:517–527, 2019.

[106] A Koch, P Wittke, and F Walther. Computed tomography-based characterization of fatigue behavior and damage development of extruded profiles made from recycled AW6060 aluminum chips. *Materials*, 12(15), 2019.

[107] D Wagner, N Ranc, C Bathias, and P C Paris. Fatigue crack initiation detection by an ifrared thermography method. *Fat & Fract. of Eng. Mat. & Struct.*, 33(1):12–21, 2009.

[108] P Koruba, M Karoluk, G Ziólkowski, and E Chlebus. Application of thermal imaging system for prediction of fatigue crack initiation in ti-6al-4v fabricated by ebm. In *Proceedings of 14th quantitative InfraRed Thermography Conference*, June 2018.

[109] C Q Cai and C S Shin. A normalized area-compliance method for monitoring surface crack development in a cylindrical rod. *JOF*, 27:801–809, 2005.

[110] J Toribio, J C Matos, B González, and J Escuadra. Numerical modeling of crack shape evolution for surface flaws in round bars under tensile loading. *Engineering Failure Analysis*, 16:618–630, 2009.

[111] J Toribio, J C Matos, B González, and J Escuadra. Compliance evolution in round cracked bars under tensile fatigue. *Engineering Fracture Mechanics*, 78:3243–3252, 2011.

[112] J Toribio, J C Matos, B González, and J Escuadra. Fatigue cracking paths and compliance analysis in round bars under tension and bending. In *Proceedings of 13th International Conference on Fracture*, June 2013.

[113] J Toribio, J C Matos, B González, and J Escuadra. Evolution of crack paths and compliance in round bars under cyclic tension and bending. *Theoretical and Applied Fracture Mechanics*, 80:104–110, 2015.

[114] MATLAB®. *Curve Fitting Toolbox Documentation: Filtering and Smoothing Data*, 2017b edition.

[115] F Ellyin. *Fatigue Damage, Crack Growth, and Life Prediction*. Chapman & Hall, 1997.

[116] M F E Ibrahim and K J Miller. Determination of fatigue crack initiation life. *Fat. of Eng. Mat. and Struct.*, 2:351–360, 1980.

[117] J A Sova, Jr. J H Crews, and R J Exton. Fatigue-crack initiation and growth in notched 2024-T3 specimens monitored by a video tape system. Technical report, NASA Langley Research Center, 1976.